

RICE UNIVERSITY

# Spatiotemporal Response of the Photoreceptor Network

by

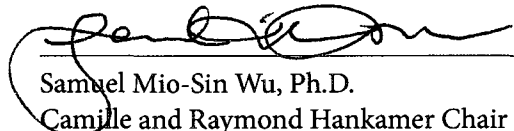
**Andrew Barrow**

A THESIS SUBMITTED

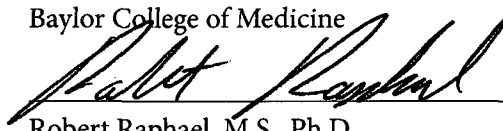
IN PARTIAL FULFILLMENT OF THE  
REQUIREMENTS FOR THE DEGREE

**Doctor of Philosophy**

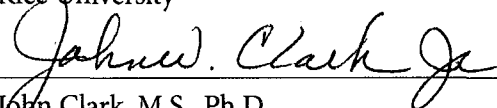
APPROVED, THESIS COMMITTEE:



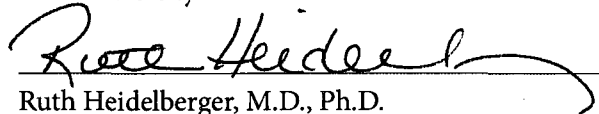
Samuel Mio-Sin Wu, Ph.D.  
Camille and Raymond Hankamer Chair of  
Ophthalmology  
Professor of Neuroscience  
Professor Molecular Physiology and Biophysics  
Baylor College of Medicine



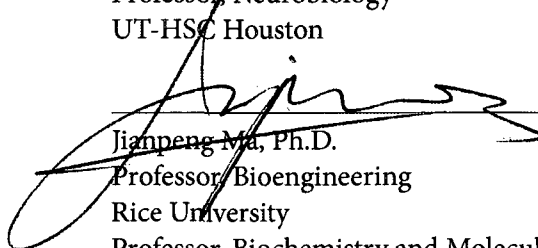
Robert Raphael, M.S., Ph.D.  
Associate Professor, Bioengineering  
Rice University



John Clark, M.S., Ph.D.  
Professor, Electrical and Computer Engineering  
Joint appointment, Bioengineering  
Rice University



Ruth Heidelberger, M.D., Ph.D.  
Professor, Neurobiology  
UT-HSC Houston



Jianpeng Ma, Ph.D.  
Professor, Bioengineering  
Rice University  
Professor, Biochemistry and Molecular Biology  
Baylor College of Medicine

Houston, Texas

December, 2009

UMI Number: 3421162

All rights reserved

**INFORMATION TO ALL USERS**

The quality of this reproduction is dependent upon the quality of the copy submitted.

In the unlikely event that the author did not send a complete manuscript and there are missing pages, these will be noted. Also, if material had to be removed, a note will indicate the deletion.



UMI 3421162

Copyright 2010 by ProQuest LLC.

All rights reserved. This edition of the work is protected against unauthorized copying under Title 17, United States Code.



ProQuest LLC  
789 East Eisenhower Parkway  
P.O. Box 1346  
Ann Arbor, MI 48106-1346

## ABSTRACT

### SPATIOTEMPORAL RESPONSE OF THE PHOTORECEPTOR NETWORK

by

Andrew Barrow

The retina is a specialized part of the central nervous system adapted to encoding images into electrical signals. Images are formed on the back of the eye by the lens and cornea, and photons that make up those images are absorbed by light sensitive pigments in the photoreceptors. Photon absorptions by these pigments generate a current, the photocurrent, which is modified by voltage-gated ion channels and electrical connections to adjacent photoreceptors. A voltage change in the photoreceptor is transformed into a chemical signal to downstream cells by its modulatory effect on the calcium concentration at the synapse. This thesis examines two important elements in photoreceptor function other than the photocurrent: the  $I_h$  current and electrical coupling between rods.

Here, using the tiger salamander (*Ambystoma tigrinum*) as a model, we investigate the kinetic properties of the HCN channels responsible for the  $I_h$  current in photoreceptors, and show that they are similar in rods and cones, which in turn are similar to the known properties of the HCN1 isoform. With western blot and immunostaining, we show that the HCN1 isoform is present in retina. We also demonstrate how HCN channels modify the kinetics of the rod and cone light response to make it faster. This thesis integrates this and other data from photoreceptor ion channels into physiology-based models of rod and cone photoreceptors. Through simulation, the model of the rod demonstrates that conductance changes from the h and Kx currents largely cancel one another during the rod light response. The cone model is used to demonstrate the feasibility of two proposed mechanisms for horizontal cell to cone negative feedback.

Finally, this work presents measurements of electrical coupling between rod photoreceptors in the salamander retina using both light and electrical stimuli. Using measured parameters for the coupling resistance, a model of the electrically coupled network of rod photoreceptors is developed. We use this model to demonstrate how rod-rod coupling decreases noise at the expense of attenuating sharp contrasts in visual scenes. The model predicts the tradeoff between these two factors results in an overall improvement in the signal-to-noise ratio for most perceptible stimuli. Results suggest that photoreceptor coupling is especially helpful in the perception of images with statistical qualities similar to natural scenes.

## Acknowledgments

I would like to acknowledge my wife, Sandra, for her support and encouragement throughout my studies. I would also like to thank my extended family, and especially my mother, Terri Barrow, who were very helpful and supportive while I worked to write this thesis.

Sam Wu has been a mentor as well as a friend throughout my studies. In addition to providing all of the equipment, facilities, and materials for these studies, our many conversations have shaped and guided my learning process.

I would also like to especially acknowledge Fan Gao, who meticulously collected the data for the paired rod recordings presented in section 5.3. His sense of humor and fondness for conversation have provided a useful distraction from lab work.

I would like to thank David Simons and Cameron Cowan for many interesting conversations and feedback on ideas, and Zhou Yang for her instruction and help with performing western blots and immunohistochemistry. Mohammad Abd-el-Barr served as an influential mentor and role model when I was new to the lab. Furthermore, I would like to acknowledge other members and former members of the lab who contributed in many ways: Aijun Zhang, JiJie Pang, and Roy Jacoby.

Finally, I would like to acknowledge the funding sources that made this research possible: NIH grants EY04446, EY02520, the Retina Research Foundation (Houston), Research to Prevent Blindness, Inc. provided generous support for our lab. I also received support for several years from the NIH T32 predoctoral training grant EY007001.

# Contents

Abstract	ii
Acknowledgments	iii
List of Illustrations	vii
List of Tables	viii
<b>1 Introduction</b>	<b>1</b>
1.1 Motivation	1
1.2 Background	5
1.2.1 $I_h$ and HCN Channels	6
1.2.2 Electrical Coupling in the Retina	9
<b>2 Materials and Methods</b>	<b>11</b>
2.1 Materials	11
2.2 Solutions	12
2.3 Recordings	13
2.4 Immunohistochemistry and Western Blot	16
2.5 Data analysis	18
2.6 Numerical Methods	21
<b>3 Properties and Function of HCN Channels in Photoreceptors</b>	<b>22</b>
3.1 Introduction	22
3.2 Molecular and Biophysical Properties	24
3.2.1 Whole-cell currents	24
3.2.2 Distribution and Molecular Identification	27
3.2.3 HCN1 single channel conductance	30
3.3 Function of HCN Channels in Photoreceptors	34
3.3.1 Simulated HCN current during rod light response	34
3.3.2 HCN contribution to photoreceptor membrane frequency response	37
3.3.3 Equivalent circuit	39

3.3.4	HCN channel shaping of photocurrent . . . . .	42
3.3.5	HCN contribution to GWN estimated kernel (impulse response) . . . . .	44
3.4	Discussion . . . . .	48
3.4.1	$I_h$ in salamander rods and cones is mediated by HCN1 channels . . . . .	48
3.4.2	Conductance of single HCN1 channels . . . . .	50
3.4.3	HCN1 channels create a bandpass filter in photoreceptors . . . . .	50
3.4.4	HCN1 channels help rods and cones efficiently encode impulses of light . . . . .	51
3.4.5	Conclusion . . . . .	53
<b>4</b>	<b>Functional Models of the Rod and Cone</b>	<b>55</b>
4.1	Interactions between $I_h$ and $I_{Kx}$ in the rod light response . . . . .	55
4.1.1	Introduction . . . . .	55
4.1.2	Results . . . . .	57
4.1.3	Discussion . . . . .	61
4.2	Model of a cone . . . . .	65
4.2.1	Feedback from horizontal cell to cone . . . . .	65
<b>5</b>	<b>Electrical Coupling in the Rod Network</b>	<b>71</b>
5.1	Introduction . . . . .	71
5.2	Measurement of coupling resistance using light stimuli . . . . .	73
5.3	Measurement of coupling resistance using electrical stimuli . . . . .	78
5.4	Cable Theory . . . . .	85
5.4.1	Cable equation in one dimension . . . . .	86
5.4.2	Cable equation in two dimensions . . . . .	90
5.4.3	Discrete cable . . . . .	91
5.4.4	Numerical Methods . . . . .	91
5.4.5	Network input impedance . . . . .	94
5.4.6	Network impulse response and frequency response . . . . .	95
5.5	Estimation of adjacent coupling resistance . . . . .	98
5.6	Coupling and noise in the rod network . . . . .	101
5.7	Discussion . . . . .	108
5.7.1	Measurement of coupling with light . . . . .	108
5.7.2	Measurement of coupling via dual-patch . . . . .	109
5.7.3	Significance of rod-rod coupling . . . . .	111

<b>6 Conclusion and Future Directions</b>	<b>115</b>
6.1 Conclusion . . . . .	115
6.2 Future Directions . . . . .	118
<b>A Appendix</b>	<b>123</b>
A.1 Derivation of second order model parameters . . . . .	123
A.2 Frequency domain calculations . . . . .	125
A.3 Rod model parameters . . . . .	126
A.4 Derivation of the solution for a one-dimensional infinite cable . . . . .	131
A.5 Derivation of the input impedance of a one-dimensional cable . . . . .	132
<b>Bibliography</b>	<b>133</b>

## Illustrations

3.1	Whole-cell HCN currents . . . . .	25
3.2	Immunohistochemical staining and Western Blot . . . . .	29
3.3	HCN single channel conductance . . . . .	32
3.4	Simulated HCN current . . . . .	36
3.5	HCN and membrane frequency response . . . . .	38
3.6	Circuit model analog . . . . .	41
3.7	Model predicted frequency response . . . . .	42
3.8	HCN role in the rod and cone light response . . . . .	45
3.9	HCN contribution to photoreceptor impulse response . . . . .	47
4.1	Effect of TEA and ZD 7288 on rod light response . . . . .	58
4.2	Simulation of h and Kx conductances . . . . .	60
4.3	Illustration of current flow in the rod network . . . . .	63
4.4	Model of a cone with HC feedback . . . . .	68
4.5	Simulation of HC feedback to cone . . . . .	70
5.1	Rod response to bar of light . . . . .	74
5.2	Deconvolved rod network responses . . . . .	76
5.3	Estimated space constant of rod network . . . . .	77
5.4	Voltage clamp in the rod network . . . . .	82
5.5	Superposition of point sources . . . . .	83
5.6	One dimensional cable . . . . .	88
5.7	Length constant and input impedance vs $R_c/R_m$ . . . . .	96
5.8	Impulse response and frequency response of networked cells . . . . .	97
5.9	Estimated $R_{in2D}$ from voltage clamp . . . . .	100
5.10	Rod network response and example gratings . . . . .	103
5.11	Response of the rod network to spatial frequencies . . . . .	105
5.12	Signal-to-noise ratio in the coupled vs uncoupled network . . . . .	106



## Tables

3.1	Kinetic parameters for $I_h$ and HCN isoforms . . . . .	54
5.1	Rod network parameters measured by light stimulus . . . . .	79
5.2	Network conductance values for adjacent rods . . . . .	85

# Chapter 1

## Introduction

### 1.1 Motivation

The mechanisms behind cognition and human consciousness are possibly two of the most important mysteries confronting modern science. In investigating these questions through study of the brain and nervous system, research in neuroscience is not only an endeavor to advance medical care and understanding of neurological diseases, but an effort to learn what makes us human. Although we have made a lot of progress in 60 years of modern neuroscience research in understanding specific brain systems, we still seem far away from a comprehensive picture of how the brain works.

The brain is a complex tissue with tens of billions of neurons, whose convoluted and heterogeneous interconnections lead to an unknown number of interlinked and interdependent circuits. In order to understand it all it would seem that we would have to have a tool to analyze the behavior of all of these circuits simultaneously. Some tools like fMRI can observe the activity of nearly the entire brain, and tell which areas of the brain are active at a given time by their oxygen demand. However, fMRI can only give a very broad view of which areas of the brain are active due to its limited spatial, and particularly temporal resolution. It cannot necessarily tell what those areas are doing. An fMRI image of the brain

is like a view of the earth from space. Just as brain areas light up during activity, individual cities may be lit up at night, but that light doesn't say anything about why the inhabitants of that city have their lights on. There may be people shopping, working, or driving from one place to another, each with a specific purpose or intent. Such a macroscopic viewpoint may be useful for some purposes, but it obscures the rich detail and meaning of the activity. Clearly to understand what is going on we must use other tools as well.

In contrast to the top down approach used in fMRI studies, another way to study the brain is to begin by analyzing some of its neurons in isolation, where detailed electrical recordings can be made, and the effect of drugs or other neuromodulatory substances can be tested. This bottom up approach has traditionally been employed by researchers who study the hippocampus or simple invertebrates such as the sea slug or roundworm. One of the difficulties in studying brain sections in vitro, however, is that the normal inputs to the neurons have been removed. The slice can be stimulated with a microelectrode, but such an artificial stimulus may not have any similarity to the physiological inputs to these neurons.

On the other hand, the retina is a part of the central nervous system (CNS) whose physiologic inputs are familiar: two dimensional patterns of light that form images. As a high-throughput source of information for the visual cortex and higher level brain centers, it is our brain's window to the external world. Part of the visual system, it arguably provides more information about our external environment than any of our other senses. In addition, it appears to function on its own in isolation, although it may rely on some level of feedback from the brain.

By studying the retina, we can characterize responses of its neurons to its normal physiologic stimuli— light. We can also examine how these physiologic signals are transformed as they are relayed from one set of neurons in the retina to another, and back through negative feedback loops. By studying the retina, neurophysiologists hope not only to discover the basis of vision, but to find basic principles that underly systems of neurons that are applicable to the rest of the CNS. One such principle that is applicable to visual information processing in both the visual cortex and the retina, is center-surround receptive field antagonism (CSRFA). This phenomenon, which enhances contrast around edges in visual scenes, comes from negative feedback from downstream neurons with wide receptive fields back to upstream neurons. It leads to counteracting receptive field areas for a neuron called the center and surround. This basic feature has been found in sections of the visual system from its first stage, in the photoreceptors, all the way up to the visual cortex.

Another interesting feature of the retina as an image detector that is unmatched by any conventional camera is that it is able to respond to light over a billion fold difference in intensity without saturating. In the retina this feature is called adaptation, and while there appear to be many mechanisms that underly this response, the basic principle of adaptation is important in other neural circuits in the CNS, where it is often referred to as gain modulation [106]. In turn, gain modulation is also similar to the concepts of facilitation and inhibition.

A logical place to start studying the retina is with the photoreceptors— the neurons which first transform light stimuli into electrical signals. If we are able to say that we have

a good understanding of how these neurons that comprise the very first interface between the CNS and the outside world, then we will have accomplished a small but respectable step toward understanding the CNS. This thesis undertakes a study of photoreceptor physiology with the intent to contribute toward this goal.

A unique and notable feature of the retina is that the photoreceptors, the cells that initially respond to light, encode this light with graded potentials. This means that they represent visual information as a continuous function of their membrane voltage. In this way they are "analog" neurons. The photoreceptors pass on visual information to other "analog" neurons called bipolar cells and horizontal cells. Eventually after being passed between and transformed by cells with graded potentials, the information reaches ganglion cells, which then encode the signals into an action potential. This action potential is an angle modulated\* binary signal that is characteristic of most of the rest of the neurons in the CNS.

Relevant to the introduced theme of generalizability, two features of photoreceptor physiology investigated in this thesis also appear to be important in other neural systems. The first is a type of very specialized ionic current in photoreceptors that appears to have many interesting roles in human physiology. This current,  $I_h$ , is unique in that the ion channels that gate it are opened by hyperpolarizing voltages in contrast to the conventional depolarization dependent gating characteristic of other ion channels.  $I_h$  is present in the heart, where it acts as the primary cardiac pacemaker, and in the brain, where it may regulate rhythmic activity and modulate gain of neuronal synapses [106]. This work investigates the

---

\*encoded by either the firing frequency, or relative phase between firings

biophysical properties and function of  $I_h$ , showing that it is a fundamental building block for neural systems, and demonstrates how it plays an important role in photoreceptor responses to light.

Electrical coupling between rod photoreceptors is another feature of photoreceptors that is applicable to other neurons in the retina, myocytes in the heart, and neurons in the brain. In the retina, electrical coupling between adjacent rods lowers their intrinsic noise level, and allows them to average light responses over space. This thesis describes our investigations into the relevant conductances involved in rod-rod coupling, and shows how this leads to tradeoffs in noise tolerance versus image fidelity in the rod network. This analysis is certainly applicable to other networks of coupled retinal neurons such as bipolar cells, but may also be applicable to other systems in the brain where lateral coupling can serve to reduce noise in redundant parallel pathways.

## 1.2 Background

The use of the tiger salamander (*Ambystoma tigrinum*) as a model organism began with Lasansky's investigations of the anatomy of the salamander retina using electron microscopy [71]. The salamander is a convenient model organism for retinal research because its cells are very large (a rod photoreceptor is  $\approx 10$  microns in diameter), facilitating easy electrical recordings with a glass microelectrode or patch pipette. Importantly, the basic structure of the salamander retina is the same as that of other vertebrates, including primates. This includes a layer of photoreceptors that includes rods and cones, depolarizing and hyperpo-

larizing bipolar cells, amacrine cells, and retinal ganglion cells. However, salamanders, like all non-primates, do not have the dense central collection of cones and associated bipolar cells that comprise the fovea.

While genetic manipulation has made the mouse the model organism of choice for most biologists, its photoreceptors are too small to make practical recordings from. However, it is possible to record from other cell types in the mouse retina such as bipolar cells, horizontal cells or ganglion cells. Because the focus of this thesis is photoreceptor electrophysiology, the salamander is the model organism of choice for our studies.

### 1.2.1 $I_h$ and HCN Channels

The study of the  $I_h$  current and HCN channels has a very diverse history. It was first recognized as a hyperpolarization gated conductance that regulates pacemaking in the sino-atrial (SA) node of the heart [23]. In cardiac tissue the current was called  $I_f$ , or "funny current", because it was gated during hyperpolarization and contributed to depolarization of myocytes. It was found that the activity of this current could be increased by  $\beta$ -adrenergic input to the heart [22], which accelerated heart rate.  $I_f$  activity can be decreased by cholinergic input to the heart through the vagus nerve [37, 36]. Both of these effects were found to be mediated by cAMP internal to the cell. Increasing cAMP concentrations cause a negative shift in the activation curve, and decreasing levels a rightward shift. In the late 1990s, Molecular cloning revealed the genes encoding the protein subunits (HCN1-4) that form the channels for the  $I_h$  and  $I_f$  currents [92, 93]. These subunits normally combine with other

subunits of the same type to produce four different isoforms of HCN channels, HCN1-4. Each of these isoforms has characteristic properties, including different gating kinetics, activation curve, and sensitivity to cyclic nucleotides. However, subunits can also combine to form heteromeric HCN channels with properties that are intermediate to those of the purely homomeric channels [3].

Meanwhile retinal researchers had also discovered a hyperpolarization activated current in photoreceptors in the early 1980s. Detwiler and Hodgkin found that such a current was important in causing signals propagating in the rod network to peak earlier in more distant rods than in the source rod, an effect they called "negative propagation delay" [33, 34]. Attwell and Wilson dubbed this hyperpolarization activated current  $I_A$ , and studied its properties in a model of the salamander rod network [5]. They were unable to find a reversal potential for  $I_A$ , and as a result, were the first to suggest that the observed current may be a sum of two or more currents with similar kinetics. Owen and Torre studied this current's role in high pass filtering of signals in the rod network, and discovered that the current was composed of two parts: a Cesium sensitive component that caused a conductance increase on hyperpolarization, and a separate TEA sensitive potassium component that caused a conductance decrease on hyperpolarization [87]. Bader and Bertrand first measured the reversal potential for the cesium sensitive component, and showed that it is between the reversal potentials for sodium and potassium, naming component  $I_h$  [9]. Hestrin was the first to study the kinetics of  $I_h$  in the retina in detail, and showed that it is different from the inward rectification that is present in muscle and oocytes. Barnes and Hille and Maricq



and Korenbrot study  $I_h$  in salamander cones, showing that it is similar to the current in rods [13, 78].

Meanwhile, Barnes et al studied the TEA sensitive component and called it  $I_{Kx}$ , finding that it is important in filtering smaller light responses, while  $I_h$  is more important in filtering larger light responses. Akopian and Witovsky reported that  $I_h$  can be modulated by D2 dopaminergic receptors [1], and MacLolm et al. show that it can be modulated by protons (pH) [75]. Satoh and Yamada showed that  $I_h$  in rods could be blocked with the cardiac  $I_f$  inhibitor ZD 7288 [94], which suggested that the origin of the two currents is the same. Demontis et. al and Gargini et al performed a series of studies demonstrating that HCN1 channels are present in rabbit rods, and that the  $I_h$  current is important in maintaining the retina's temporal response to light stimuli [30, 48, 49, 31]. They noted the similarity in its kinetics to the cardiac  $I_f$ . Moosmang et al. perform immunohistochemical staining of the mouse retina to show the distribution of HCN1-4 isoforms [82]. Later, Ivanova and Müller along with Cangiano et. al studied the properties of  $I_h$  in retinal bipolar cells [83, 58, 26].

While this long list of contributions is not entirely comprehensive, it highlights the main contributions to studies of  $I_h$  in the retina up to this point. Much has been learned about this current since its discovery, but some questions remained that our studies addressed. Namely: Is  $I_h$  the same in rods and cones, and if so, what is its function in each of these cells? What is the conductance of single HCN channels in the retina? and Which HCN isoforms are responsible for  $I_h$  in salamander rods and cones?

### 1.2.2 Electrical Coupling in the Retina

Electrical coupling was first proposed by Baylor et al. to exist between cone photoreceptors when receptive field measurements from individual cones in the turtle retina gave results much larger than the size of an individual cone [16]. Later, a pair of papers by Lamb and Simon analyzed voltage noise in the turtle cones [69, 70]. With the help of Hodgkin, they proposed several analytical models for the voltage response in the cone network, which are also reproduced and discussed in section 5.4 of this thesis. Lamb and Simon showed that voltage noise is inversely proportional to the length constant in the coupled network, and pointed out that coupling causes the signal-to-noise ratio for small stimuli to be degraded compared to uncoupled cones [69]. Detwiler and Hodgkin further analyzed coupling in the turtle cones using both microelectrodes and light stimuli [32], demonstrating a length constant of  $25 \mu\text{m}$ . They acknowledged that the length constant measured with light stimuli may be an overestimate as a result of light scattering in the retinal tissue. They also made note of the "negative propagation" delay in studies of turtle rods [33, 34]. Following these studies, Torre and Owen examined high pass filtering that causes this phenomenon in the toad rod network [103]. Attwell and Wilson made recordings of salamander rod coupling using microelectrodes, reporting a  $300 \text{ M}\Omega$  coupling resistance [5]. From this data, they used a Hodgkin-Huxley type model of a single  $I_A$  current to describe lateral signal propagation in the rod network. Later, Attwell et al. used the same framework to model interactions between rods and cones, estimating the coupling resistance between the two cells as  $5000 \text{ M}\Omega$  [7]. Attwell and Wilson also demonstrated how coupling in the rod network affects the

voltage distribution in the bipolar cell layer [6]. Deans et al. showed that the gap junction protein connexin-36 is expressed between mouse rods [29], highlighting it as a candidate for rod-rod coupling. Zhang and Wu recorded from salamander rods in the slice preparation and measured a coupling resistance of 2 G $\Omega$ . They also showed immunostaining for connexin-35/36 between these rods, implicating connexin-36 as the determinant of rod-rod coupling.

While there have been at least two separate estimates of the coupling resistance between salamander rods, the reported values are very different from one another. This may be due to drawbacks in the experimental techniques used by each of the reports. The 300 M $\Omega$  estimate by Attwell and Wilson was performed using sharp electrodes, which could have compromised the cell membrane, and the 2000 M $\Omega$  estimate was performed in retinal slices, where the connections between rods could have been damaged. While it is well known that rod-rod coupling reduces noise in the network, the conditions under which this translates to a favorable signal-to-noise ratio are unclear. In chapter 5, this thesis attempts to address these deficiencies.

## Chapter 2

### Materials and Methods

#### 2.1 Materials

Tiger salamanders (*Ambystoma tigrinum*) were kept on a 12 hour light-dark cycle in a temperature-controlled environment. Animals were handled according to NIH guidelines, and the Baylor College of Medicine Committee for Animal Use approved the methods of this study. The salamanders were first dark adapted for 45 minutes, then anesthetized with MS2222 and quickly decapitated after they were unresponsive. Eyes were then enucleated and the retinas were dissected under infra-red light with night vision scopes (BE Meyers, Redmond, WA) mounted to a stereomicroscope. The dissected whole retina was then fixed to a piece of filter paper which was first secured to the bottom of the recording chamber with a small amount of silicon grease and with a small window for transillumination carved into it. The ground electrode consisted of chlorided silver wire. The chamber was mounted in a Zeiss Universal Microscope (Carl Zeiss, Oberkochen, Germany) with Hoffman Modulation Contrast inside a light isolating faraday cage. Perfusion was supplied by gravity feed through a valve manifold (ALA Scientific, Westbury, NY), and solution was recirculated with a peristaltic pump. Extracellular solutions were bubbled with 100% O<sub>2</sub>. For experiments measuring light responses, a deep infrared filter was placed on the microscope condenser and all extraneous

light sources were eliminated. Night vision scopes mounted to the microscope eyepieces converted infra-red light to visible light in order to view the preparation. An MP-285 micro-manipulator (Sutter Instruments, Novato, CA) provided fine control of the pipette electrode for recordings.

## 2.2 Solutions

Normal Ringer's Solution was used for recordings of cell light response, and consisted of (in mM) 108 NaCl, 2.5 KCl, 1.2 MgCl<sub>2</sub>, 2 CaCl<sub>2</sub>, and 5 HEPES. Solution pH was titrated to 7.7 with NaOH. For recordings of HCN gated currents, 20 TEA, 5 CoCl<sub>2</sub> and 5 BaCl<sub>2</sub> were added to the solution to block BK and Ca-dependent potassium channels, calcium channels, and I<sub>Kx</sub> potassium channels, respectively. Intracellular solutions for whole cell recordings consisted of (in mM) 106 K gluconate, 5 NaCl, 2 MgCl<sub>2</sub>, 5 EGTA and 5 HEPES, with pH 7.4 titrated with KOH. Pipette solutions for cell attached recordings of HCN channels consisted of 106 KCl, 167 NaCl, 1.8 CaCl<sub>2</sub>, 1 MgCl<sub>2</sub>, and 5 HEPES, and were titrated to pH 7.7 with NaOH. The purpose of this non-physiologic solution was to increase the driving force of the HCN channels inside the patch. The reversal potential for the HCN channels with this solution was approximately +9 mV assuming a [Na]/[K] permeability ratio of 0.33 [108, 54]. In chirped current and current step injection experiments, K<sup>+</sup> and Ca<sup>++</sup> channels were blocked, and the HCN channel blocker ZD 7288 was perfused at a concentration of 100 μM to selectively block the I<sub>h</sub> current. Although ZD 7288 is known to be a specific blocker of HCN channels [15], in light response experiments, normal saline solution was used, and the

ZD 7288 concentration was reduced to 50  $\mu\text{M}$  in order to minimize potential cross over to other ion channels.

### 2.3 Recordings

Recordings were made with an EPC-10 amplifier (HEKA, Lambrecht-Pfalz, Germany) in either voltage clamp or current clamp mode. All power supply cables were shielded, which along with the Faraday cage were well grounded [52]. Baseline noise levels recorded in voltage clamp mode with no pipette attached to the pipette holder were measured to be 140 fA RMS. Unless otherwise stated, data was low-pass filtered at 4 kHz with a Bessel filter, and sampled at 10 kHz to avoid aliasing. Patchmaster software (HEKA, Lambrecht-Pfalz, Germany) was used to generate stimulus pulses and record the data.

Glass electrodes were pulled from 1.5 mm OD thick-walled (0.86 mm ID) 10 cm glass with filament (Sutter Instruments, Novato, CA) on a programmable P-97 puller (Sutter Instruments, Novato, CA). Using thick glass reduced pipette capacitance and noise [52]. Smaller tipped pipettes were pulled for whole-cell recording in order to minimize the effects of wash-out. These pipettes measured 8-10  $\text{M}\Omega$  when filled with intracellular solution. These results are corrected for a calculated liquid junction potential of +14 mV [91]. Larger tipped pipettes were pulled for cell attached recordings in order to increase the number of HCN channels present in a patch. These pipettes measured between 1.5-3  $\text{M}\Omega$  when filled with the cell attached solution. Giga-seals with these pipettes incorporated a large area of membrane in order to maximize the HCN channel current. Typical cell attached

background noise levels with a giga-seal patch were 400-600 fA RMS at 4 kHz bandwidth.

To measure the  $I_h$  IV curve, activation curve, and activation time constants, a voltage-clamp protocol that pulsed cells from a holding potential to command potentials between -134 mV and -24 mV and then to a tail potential of -4 mV was used. Leak currents were subtracted with a standard P/4 protocol [91].

For chirped current stimulus recordings, stimuli were modulated by exponentially increasing frequencies (equation 2.1) in order to increase the signal component in the low frequency range, where the response of the cell is more interesting. Frequency range was .5 to 20 Hz, and delivered over a period of 20 seconds. MATLAB (Mathworks) was used to generate frequency-chirped sine wave stimuli (equation 2.1) and gaussian white noise stimuli, which were then fed into Patchmaster. Frequency chirped stimuli were sampled at 500 Hz. Current amplitudes were approximately 50 pA with a 50 pA offset, but were determined at the time of experiment by the voltage response to steps of current input. Stimuli were calibrated to have voltage responses no less than -100 mV in order to avoid dielectric breakdown.

$$I_{stim} = I_{amp} \cdot \cos(2\pi f_{start} \cdot e^{(t \cdot k)} \cdot t) + I_{offset} \quad (2.1)$$

$$k = \ln\left(\frac{f_{end}}{f_{start}}\right) / t_{max}$$

Recordings of whole cell currents from both rods and cones were made using the whole mount retina. To control for the potential effect of  $I_h$  activation in adjacent cells contribut-

ing to the recorded response, some recordings were made from single dissociated cells, and the results compared against the data from the whole mount retina. These responses cells fell within the range for recordings from the whole mount retina (figure 3.1 A2). Although rod-rod coupling appears to play an important role in propagating small electrical signals between adjacent rods, it does not affect our characterization of the kinetics of the  $I_h$  current in a single cell. Our experiments involve much larger currents, making the contribution from neighboring cells negligible compared to the current induced in the recorded cell. Given a rod impedance of,  $550 \text{ M}\Omega$  and a coupling resistance of  $2 \text{ G}\Omega$  [115], this would result in the adjacent cell being hyperpolarized at most to  $-57 \text{ mV}$  in our experiments, where a proportionally small  $I_h$  current is generated (figure 3.1 A3, B3). Only part of this activated current in adjacent cells would flow back into the voltage clamped cell.

### **Light Responses**

Light responses were recorded using current clamp mode.  $R_s$  compensation in the EPC-10 acted as a bridge to ensure that the voltages were properly scaled. Light stimuli were generated by converting the voltage from the D/A converter on the amplifier into a current source via an op-amp, which was used to drive either a  $627 \text{ nm}$  or  $530 \text{ nm}$  Luxeon K2 LED (Phillips). The light output from the LEDs was found to be proportional to the drive current.

### **Impulse Responses**

We estimated the impulse response of photoreceptors using the  $627 \text{ nm}$  or  $530 \text{ nm}$  LED light source modulated with  $30 \text{ Hz}$  gaussian white noise. The noise was generated in MATLAB



and had equal variance and mean, and was delivered to the preparation at 1000 Hz sample rate in phase with the current clamp recordings. First order kernels were estimated using the Lee-Shetzen cross-correlation approach, with the first order kernel equal to the weighted cross-correlation between the stimulus and recorded response [80]. For the purposes of this paper, we use the term impulse response to describe the first order kernel. This is because photoreceptors can be approximated as linear—the power of the photoreceptor response is comparable to the power of the first order kernel predicted response [79].

## 2.4 Immunohistochemistry and Western Blot

Immunohistochemical experiments were performed using a rabbit anti rat polyclonal HCN1 antibody (Sigma) and a rabbit anti human HCN3 antibody (Santa Cruz Biotech). Salamander retina was embedded in low temperature gelling agar (Sigma) and cut into 40  $\mu\text{m}$  sections with a vibratome. Sections were permeabilized and blocked with a 10% donkey serum in phosphate buffered saline (PBS) with Triton overnight, and then incubated in primary antibody in 3% donkey serum PBS for 5 days. The sections were washed and incubated overnight in donkey-anti-goat antibodies tagged with Alexa-488 (Molecular Probes). They were then mounted on slides and imaged on a Zeiss LSM 510 microscope.

Western blot experiments were performed using the same HCN1 and HCN3 antibodies as the immunohistochemistry. The anti-HCN1 antibody's epitope was residues 6-24 (near the N terminus) of rat HCN1 protein, representing the intracellular domain. A BLASTp search in Pubmed demonstrated that this sequence is highly conserved among mouse, rat,

human, rabbit and cat, and that it should not cross react with other known proteins. The anti-HCN3 antibody's epitope was amino acids 625-774 near the C-terminus of the human HCN3 protein.

Mouse brain and 12 salamander retinas were extracted and homogenized in a buffer consisting of 500mM NaCl, 20 mM Tris-HCL buffer at pH 7.5 (Bio-Rad), 2mM EGTA (Fluka) and a protease inhibitor cocktail tablet (Roche). Extracts were kept on ice, and centrifuged at 4 C at 500 g for 20 minutes. The supernatant was extracted and pellet discarded. For the mouse brain, in order to isolate membrane proteins, the extract was centrifuged at 30000 g for 20 minutes at 4 C and the pellet was collected. Runs of non-ultracentrifuged brain extract gave identical results to the ultracentrifuged extract. Ultracentrifuged retina did not yield enough protein pellet to stain. Ultracentrifuged brain was resuspended in 10% SDS. Extracts were combined 1:1 into a Laemmli buffer (Bio-Rad) and denatured at 80 C for 10 minutes. Solutions were run in a 7.5% Tris Ready-gel (Bio-Rad) for 45 minutes at 100 V, and transferred for 60 min at 110 V to a PVDF membrane pre-soaked in methanol. Transfer buffer was Tris/Glycine + 20% methanol.

The membranes were incubated in antibodies at a 1:200 dilution in 3% milk overnight. After three sets of washes, they were incubated once again with HRP conjugated anti-rabbit antibody at a 1:500 dilution. Membranes were washed 3x again, and reacted with ECP detection solution. The reaction was exposed onto X-ray film for either 5 or 10 minutes and developed. BLASTp searches on antibody epitope were performed on *Xenopus tropicalis* data obtained from Xenbase.org [20].

## 2.5 Data analysis

Data Analysis was performed with Igor Pro or MATLAB using custom written and standard built-in routines.

### Non-stationary Fluctuation Analysis

Nonstationary Fluctuation Analysis (NSFA), sometimes called Nonstationary Noise Analysis (NSNA) was used to estimate the conductance of single HCN channels [61, 91, 95]. This technique uses many repeated command voltage pulses to create a collection of many current responses. This collection of traces is referred to as an ensemble. From this ensemble, the variance and mean current can be computed at each point in time using equation 2.2. A plot of the variance versus the mean was used to estimate the single channel conductance by fitting with a parabola. We use software routines written in Igor Pro for the NSFA. For our experiments, NSFA was performed on a series of 100 or more data traces pulsed to no more than -94 or -104 mV in order to avoid dielectric breakdown of the membrane. Ideally the noise analysis should be performed using a command pulse that can both fully activate the ion channel of interest and generate sufficient driving force for the current. However, photoreceptor cell membranes experience dielectric breakdown beginning near -100 mV [44]. Dielectric breakdown manifests itself as a transient high amplitude  $1/f$  noise process, invalidating the fluctuation analysis in traces where it is present. Therefore we had to use a less hyperpolarized voltage in order to achieve recordings uncorrupted by membrane breakdown. As a result, our NSFA estimates could achieve a maximum  $P_o = .95/.85$

for  $V_c = -104/-94$  mV.

For most recordings, equation 2.2 was sufficient to estimate the variance in the current [4, 53, 66].

$$\sigma^2(t) = \frac{1}{N-1} \sum_{x=1}^N (i_x(t) - I(t))^2 \quad (2.2)$$

where  $i_x(t)$  is the trace and the mean,  $I(t)$  is defined by:

$$I(t) = \frac{1}{N} \sum_{x=1}^N i_x(t)$$

An isochrone is defined as a cross section of the ensemble of traces with respect to one point in time:

$$\{i_x(\tau) : 1 \leq x \leq N\}$$

where  $\tau$  is a particular time of interest that defines the isochrone.

However, for the whole cell NSFA estimates and some cell attached NSFA estimates, a method that could account for the time dependent "rundown" in the current traces in the ensemble was necessary [4]. Rundown is noticeable when the amplitude of HCN activation current or cell capacitance drifts over time, and successive traces in the ensemble are then no longer stationary with respect to their isochrone. This change could be due to a washout of cell cytoplasm, a change in membrane capacitance, or deactivation of some HCN channels over time. To minimize the effect of rundown, we calculated the variance from the differences between the traces, as in equation 2.3 [4, 66].

$$\sigma^2(t) = \frac{2}{N-1} \sum_{x=1}^N (y_x(t) - Y(t))^2 \quad (2.3)$$

with  $y_x(t)$ , the difference between two successive traces, defined by:

$$y_x(t) = \frac{y_x - y_{x+1}}{2}$$

and the mean of differences calculated by:

$$Y(t) = \frac{1}{N-1} \sum_{x=1}^N y_x(t)$$

Traces that had spurious transient noise, caused by either temporary membrane breakdown, external electrical interference, or other causes needed to be removed from the ensemble in order to generate a reliable estimate of the variance. If a minority of traces needed to be removed, and the effect of rundown was small over the ensemble, then the variance estimate according to equation 2.3 was reliable. Typically, traces which had 0.1% of their points 3 or more standard deviations from the mean were removed. All results in this paper are reported as mean  $\pm$  SEM unless otherwise indicated.

After acquisition at 10kHz and filtering with a lowpass Bessel filter at 4kHz, data were imported into Igor Pro for processing, and digitally filtered to 400 Hz with a Gaussian weighted FIR filter. This additional filtering step allowed us to increase the signal to noise ratio of our recordings by reducing broad spectrum background noise fluctuations. Theoretical considerations dictate that the filter time constant should be no greater than 10 times the activation time constant of the recorded channels [4]. HCN channels were seen to transition with a

time constant around 50 ms at -104 mV, which would yield a minimum filter time constant of 200 Hz. We therefore chose a 400 Hz digital cutoff frequency in order to reduce background noise while still preserving HCN kinetic information. See Kole et. al, 2006 for an analysis of single HCN channel estimates vs filtering frequency.

The single channel conductance ( $\gamma$ ) number of channels ( $N$ ) present were estimated by fitting a plot (figure 2.2 C, D) of the ensemble variance vs the mean current (figure 2.2 B) with equation 2.4.  $k$  represents the variance offset from underlying noise that is not time dependent, and was subtracted out in displayed plots (figure 2.2 C,D).

$$\sigma^2(I) = \gamma I - \frac{I^2}{N} + k \quad (2.4)$$

## 2.6 Numerical Methods

Simulations were computed in MATLAB (Mathworks) using the ode15s numerical solver. The differential equations and constants for the model are given in appendix 1. Equations for voltage gated channels come from studies previously published by Liu and Kourennyi with the  $I_h$  model as published by Barnes and Hille [73, 13]. Although more accurate models of HCN channel kinetics exist, [2] the Barnes model describes  $I_h$  kinetics relatively well (unpublished data), and requires only one state variable, greatly decreasing computational complexity. Equations and constants for the photocurrent come from studies by RD Hamer, originally from Nikonov et al. [51, 85]. Initial conditions for the model were determined by allowing the system to relax to steady-state without any light input.

## Chapter 3

### Properties and Function of HCN Channels in Photoreceptors

#### 3.1 Introduction

Hyperpolarization-activated cyclic nucleotide gated (HCN) ion channels are activated by membrane hyperpolarization, and depending on the channel isoform, modulated by cyclic nucleotides such as cAMP to a varying degree [39, 15, 96]. HCN channels serve important functions in many systems of the body. For example, they act as a cardiac pacemaker in the SA node and other parts of the heart [39] and contribute to oscillatory potentials in the central nervous system (CNS) [96]. In the retina, immunocytochemical studies have shown that various isoforms of HCN channels are expressed in retinal neurons [83], but the functional specificity of these expression patterns are not clear.

In rod and cone photoreceptors, hyperpolarization-activated currents ( $I_h$ ) have been characterized with whole-cell or microelectrode recording techniques [54, 13, 78, 30, 31]. It is not clear, however, whether  $I_h$  in rods and cones is mediated by HCN channels and whether these two photoreceptors use the same isoform of channels. Although current-voltage relations and activation properties of whole-cell  $I_h$  currents in rods have been described [54, 30, 31], the single channel conductance and density of  $I_h$  or HCN channels in photoreceptors are unknown. Here we present a systematic study of the single channel

properties of HCN channels in salamander rod and cone photoreceptors using the non-stationary fluctuation analysis (NSFA) method. By comparing single channel conductance with whole-cell currents, we estimate the total number of channels and the channel density in rods and cones. We also demonstrate via immunohistochemistry, single channel conductance, and analysis of kinetic data of whole cell currents, that  $I_h$  in salamander rods and cones is mediated by the HCN1 isoform.

In contrast to the heart and CNS, where HCN channels generate rhythmic potentials, HCN channels in the retina do not cause oscillations, but instead help shape the potentials that encode light stimuli. Evidence suggests HCN channels are necessary for the retina's temporal response to light stimuli [49, 48, 50]. The  $I_h$  current, along with another ionic conductance dubbed  $I_{Kx}$ , have been shown to create a bandpass filter effect in rod photoreceptors [5, 17, 34, 87, 103, 30, 19]. It is not clear, however, how the electrical properties of HCN channels contribute to the dynamics of rod and cone signaling, or whether these processes differ in the two types of photoreceptors. In this study, we use frequency chirped and gaussian white noise (GWN) modulated current and light stimuli to directly demonstrate how HCN channels speed up the voltage response of rods and cones. Our results show that HCN channels contribute to photoreceptor dynamics not only in response to bright flashes, where signal clipping is a factor, but also under physiologic light levels, and have varying degrees of effect in rods and cones at different adaptational conditions.



## 3.2 Molecular and Biophysical Properties

### 3.2.1 Whole-cell currents

Recordings of whole cell currents were made from rods and cones in the whole mount retina. We chose the whole mount retinal preparation over the dissociated rod and cone preparations in order to avoid adverse effects associated with enzymatic or mechanical dissociation such as changes in channel kinetics/gating or loss of axon terminals. We found that contributions from adjacent rods to recorded currents via coupling were minimal, and did not affect our results (see Recordings in Methods for explanation), as our data recorded from the intact retina also agrees with experiments on dissociated salamander rods performed by us (figure 3.1 A1) and other researchers [54]. For whole cell recordings, an extracellular solution containing TEA, cobalt and barium was used to block all other ionic currents other than  $I_h$  (see Solutions in Methods). Although the whole cell properties of the  $I_h$  current have been examined before in dissociated salamander photoreceptors or by using sharp electrodes [1, 75, 78, 54], we felt the need to characterize them in our experiments using whole cell voltage clamp in the intact retina, and standardize the recording conditions between rods and cones. This standardization allows us to directly compare our rod and cone data, compare results obtained from dark- and light-adapted conditions, and use our single channel current data to estimate the number of channels present in each cell.

Our results show that the kinetic properties of  $I_h$  in whole-cell recordings of rods and cones are very similar, which suggests that the same channels carry  $I_h$  in both cell types. We also found that physiological properties of  $I_h$  in rods and cones in dark-adapted conditions

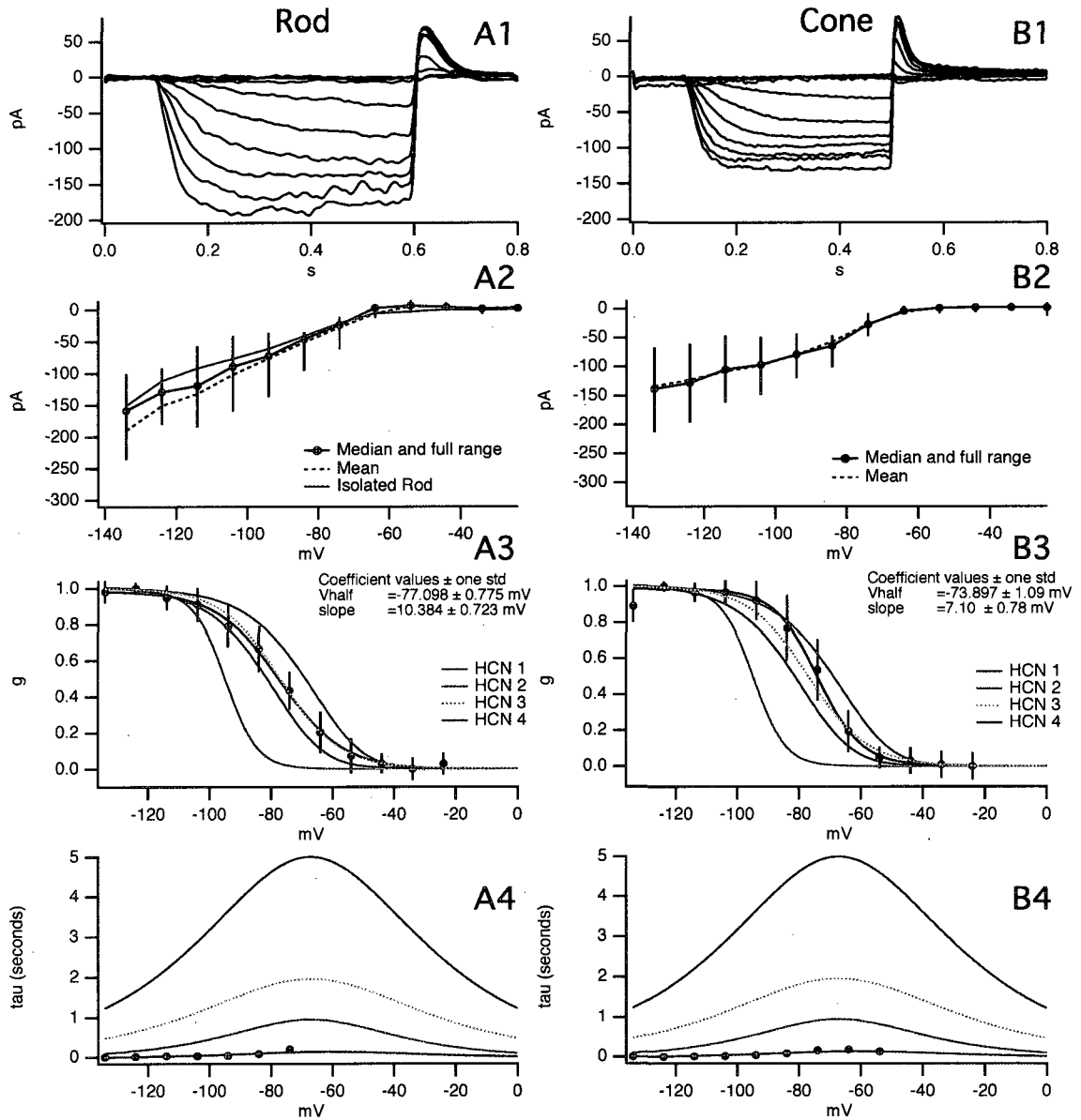


Figure 3.1 : Whole cell currents from voltage-clamp recordings from rod (A) and cone (B). (A1) and (B1) show example current traces. (A2) and (B2) show the median IV curve values with vertical bars representing the minimum and maximum range for 10 cells. (A3) and (B3) show the respective activation curves computed from the normalized and averaged tail currents of 10 cells. Data is fit with a sigmoidal exponential function of the form:  $g = b + g_{max} / (1 + e^{(V - V_{half})/slope})$ . (A4) and (B4) show the activation time constants fit with a single exponential for rod (A4) and cone (B4) data (black dots), with the color lines showing values for HCN1,2,3, and 4. In (A3,4) and (B3,4), data for HCN 1, 2, and 4 come from homogeneously expressed HCN channels (Altomare et al., 2001) plus estimated values for expressed HCN3 (Stieber et al., 2005)

are indistinguishable from those in light-adapted conditions, suggesting that  $I_h$  channels are not modulated by steady background light. Because HCN channels are also gated by cyclic nucleotides in addition to hyperpolarizing voltages, we attempted to measure the sensitivity of rod  $I_h$  to cAMP. Although other researchers have reported a small modulatory effect of cAMP on the  $I_h$  activation curve in rabbit rods [31], we were unable to produce a change in activation curve or I-V curve with bath perfusion of 8-Br-cAMP. This is consistent with reported evidence that HCN1 channels, which we believe are the primary isoform, are the least sensitive of the four HCN isoforms [15]. The steady state IV curves for rods and cones, generated by plotting the end steady state current at each holding potential, are both seen to be a hyperpolarization activated inward current with an amplitude of around -150 pA at -134 mV (figure 3.1 A2 and B2). This similarity in magnitude and rectification provides evidence that rods and cones have similar numbers of channels carrying the  $I_h$  current, assuming the identity of the channels is the same.

The steady-state activation curves, shown in figure 3.1 A3 and B3, generated by plotting the normalized amplitude of the tail currents at -4 mV vs. the command pulse amplitude, are also similar. The half activation potential for rods,  $-77.8 \pm 3.7$  mV (mean  $\pm$  std dev), is slightly more negative than for cones,  $-73.8 \pm 1.2$  mV. The activation rate constants are also similar ( $10.5 \pm 3.42$  mV for rods and  $7.1 \pm .86$  mV for cones), although the cone activation is slightly steeper. These activation curves for both cell types agree well with results published previously for rods [31, 75, 78, 54]. Also similar are the rod and cone activation time constants (figure 3.1 A4 and B4), which were generated by fitting a single exponential decay to

the traces in figure 3.1 A1 and B1. The similarity in the activation curves and time constants in rods and cones provides strong evidence that the kinetics, and therefore identity of the channels that carry rod and cone  $I_h$  is the same.

Most striking, however, is how closely the activation curves and activation time constants for rod and cone  $I_h$  resemble the activation curve and time constants for the HCN1 channel isoform. Colored lines in figures 3.1 A3 and B3 show the activation curves for an allosteric model of HCN 1, 2, and 4 channels. These allosteric models were developed from voltage clamp data of homogenous populations of HCN isoforms expressed in human embryonic kidney cells [2]. HCN3 kinetics are known to be intermediate between HCN2 and 4 [15]. We estimated the parameters for HCN3 channels from another set of data [98]. The activation curves for rod and cone  $I_h$  appear to be similar to HCN1, HCN3 and HCN4 channels (figure 3.1 A3 and B3), however, the voltage dependence of the time constants closely resembles the time constants for HCN1 channels, and is significantly different from HCN2, 3 and 4 (figure 3.1 A4 and B4). The similarity in the activation curves and activation time constants for rod and cone  $I_h$  to the HCN1 isoform provides electrophysiological evidence that HCN channels carry the  $I_h$  current, and that HCN1 is the predominant HCN isoform present in both rods and cones.

### 3.2.2 Distribution and Molecular Identification

We used antibodies against the two known neuronal HCN isoforms (HCN1 and HCN3) to label HCN channels in the salamander retina. See methods for a description of the antibod-

ies. Immunohistochemical staining of the salamander retina demonstrates stronger staining for HCN1 antibodies than HCN3 for rod and cone photoreceptors (figure 3.2). Anti-HCN1 antibodies strongly label the rod and cone inner segments, with some binding in the outer segments as well. This finding agrees with our electrophysiology data that indicates that the HCN1 isoform is dominant in these cells, however, we did not observe any HCN currents from the outer segments. HCN3 binding appears to be relatively nonspecific, with some binding in the photoreceptors.

To test the specificity of the antibodies used, a western blot was performed on salamander retina and mouse brain. For HCN1 in mouse brain (figure 3.2 A1), a single band appears in the 100-110 kDa range, which is consistent with the predicted molecular weight for mouse HCN1 (102 kDa). For salamander, a single band appears near 60 kDa (figure 3.2 A1), which is consistent with findings of other researchers from the rat retina [83]. Although the observed molecular weight is different than the mouse, the appearance of single specific band indicates that the HCN1 antibody does indicate specific binding in the salamander. A BLASTp search on the *Xenopus tropicalis* HCN1 protein sequence [20] predicts binding of the HCN1 antibody to amphibian HCN1, with homology in 15 of 19 amino acids between the antibody epitope and *Xenopus* HCN1. The 60 kDa band in retina has been observed by other researchers also using N-terminal HCN1 antibodies in rat retina [83]. It is possible that the 60 kDa protein is a truncated form of HCN1. Western blot with the HCN3 antibody (figure 3.2 B1) demonstrated distinct bands near 50 kDa in both mouse brain and salamander retina. These bands may both represent protein fragments, as the predicted mass for

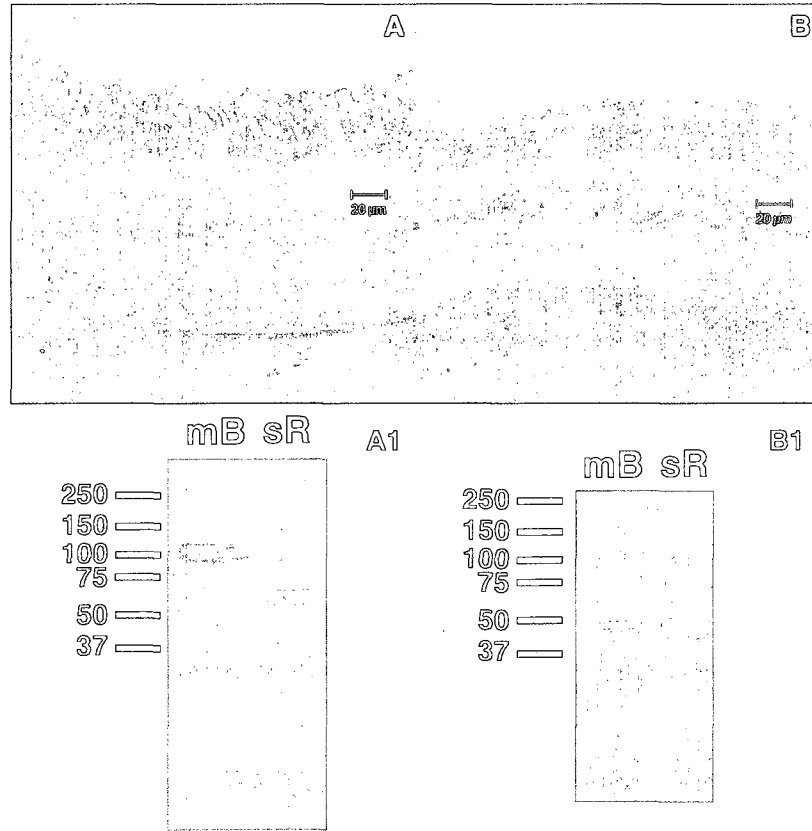


Figure 3.2 : (A) anti-HCN1 antibody binding in photoreceptors. Labeling is present in the inner segments of rods and cones. (B) HCN3 labeling also appears in photoreceptors and other cells of the retina. (A1) western blot on mouse Brain (mB) and salamander retina (sR) showing specific binding of the HCN1 antibody to protein. The resulting band is at 60 kDa in the salamander retina, below the expected 104 kDa molecular weight for intact HCN1 protein. (B1) western blot as in A1 for the HCN3 antibody.

mouse HCN3 is 85 kDa. Our results using immunohistochemical labeling and western blot of whole retina, while they cannot rule out the presence of other HCN isoforms, are supportive of our electrophysiological findings that HCN1 is the dominant isoform present in photoreceptors.

### 3.2.3 HCN1 single channel conductance

With evidence from whole cell currents and immunohistochemical experiments indicating that the identity of the  $I_h$  current in rods and cones is the HCN1 channel, we endeavored to estimate the conductance of single HCN1 channels in the whole salamander retina. Normally the conductance of single ion channels is determined by directly observing single channel events with a cell-attached patch, but the conductance of HCN channels is so small that it is below the thermal noise threshold of any physically realizable patch clamp amplifier. Therefore we used a statistical technique called Nonstationary Fluctuation Analysis (NSFA) to estimate the conductance of single HCN channels in vivo [4, 53, 95]. An ensemble of 100 traces was recorded from whole cell currents from rods using 100 traces of a command pulse to -104 mV (as in figure 3.3 A), with other channel activity blocked with special external solutions (see Solutions in Methods). The variance and mean of the ensemble were then computed (as in figure 3.3 B) (see Methods for detailed explanation) and plotted against one another (figure 3.3 C2). We initially used a whole-cell patch as opposed to the more common cell-attached technique in order to maximize the  $I_h$  current recorded. With this whole-cell NSFA recording technique, we estimated the HCN channel conductance to be

$766 \pm 242$  fS, with  $2214 \pm 986$  (std.,  $n=6$ ) channels per rod (figure 3.3 C2).

A small activation delay, which is sometimes seen as an early minimum in HCN currents, is visible in figure 2.2 3A and 3B. It appears to be more evident in recordings of cell attached HCN currents. This activation delay has been observed in HCN currents recorded from Purkinje fibers [38], salamander rods [54], and expressed HCN channels [77]. One explanation for this delay is that HCN channels have many different conformational states, and must transition to a lower conducting state shortly after a voltage pulse before reaching full activation.

While a larger  $I_h$  current can be recorded from a whole cell as opposed to a cell-attached patch, the cell-attached technique of recording currents has several advantages, including less membrane noise, avoidance of cell internal dialysis, and the ability to localize the distribution of HCN currents on the cell membrane (see Methods). Therefore, to confirm our whole-cell NSFA results, we also estimated the single channel conductance of HCN channels with cell-attached patches, using special pipette solutions to increase the HCN driving force (see Solutions in Materials Methods). The increased extracellular potassium level raised the reversal potential of HCN channels without affecting the gating kinetics of  $I_h$  [108], increasing the driving force of  $I_h$  currents. These cell attached patches in rods gave estimates of a single channel conductance of  $663 \pm 71$  fS, with  $155 \pm 42$  (std.,  $n=3$ ) channels present in each patch (figure 3.3 C1) . From the single channel conductance we estimate the number of channels per cell by dividing the whole cell conductance ( $\mu = 1.4 \pm .89$  nS) by the single channel conductance, which predicts  $2111 \pm 1342$  channels per cell. This result is similar



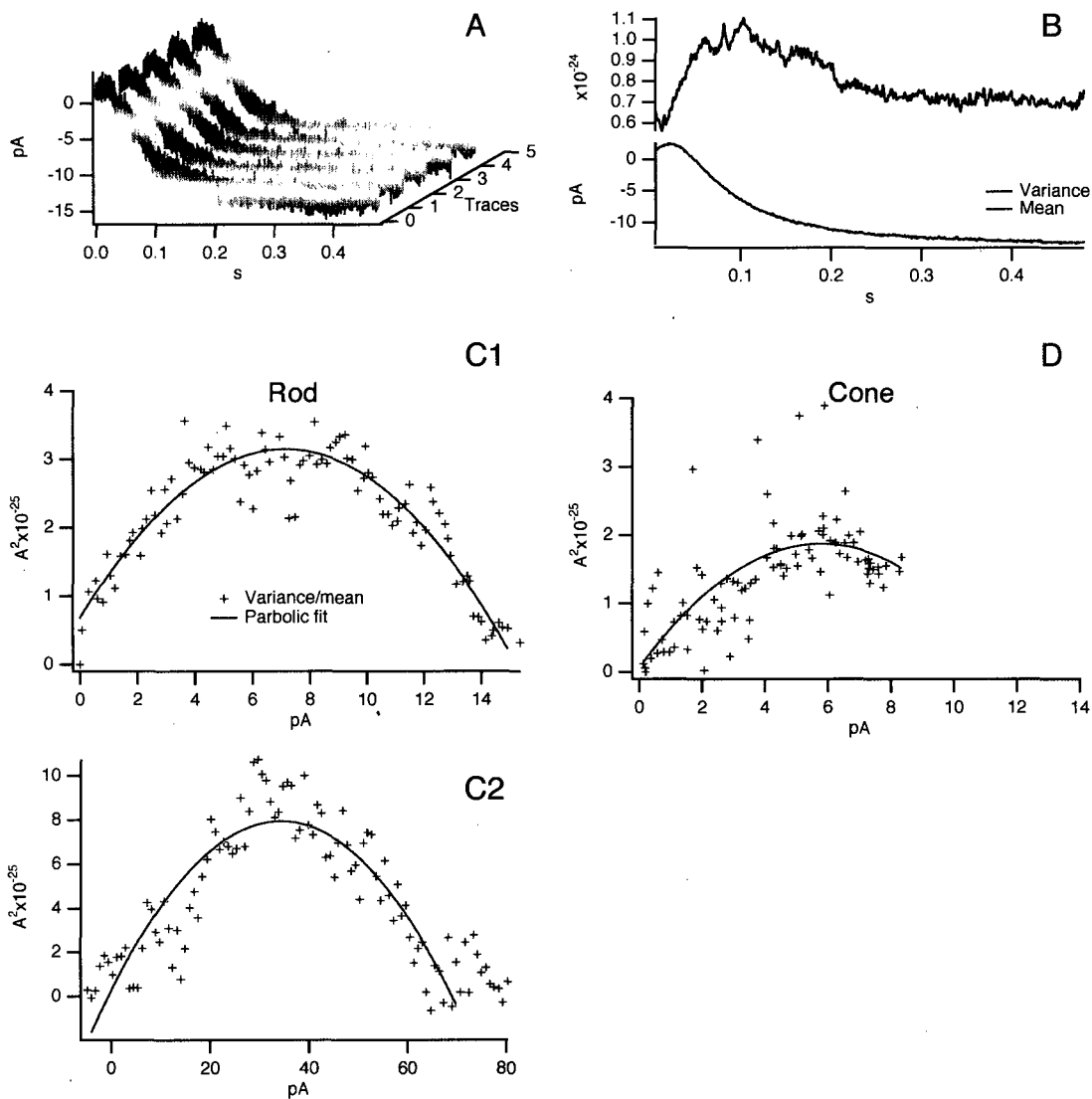


Figure 3.3 : Nonstationary Fluctuation Analysis of HCN currents (A) Five traces from an ensemble, and (B), variance and mean computed from the ensemble. (C1), In the rod, cell attached patches gave an estimate of  $663 \pm 71$  fS, with  $N=155 \pm 42$  channels in the patch (std.,  $n=3$ , two cells). (C2) Whole-cell patches estimated the conductance to be  $766 \pm 242$  fS, with  $N=2214 \pm 986$  channels (std.,  $n=6$ ). (D) In the cone, cell attached patches yielded an estimated conductance of 526 fS with 183 channels ( $n=1$ ) present per patch. Estimates were made from the coefficients of equation 2.4

to the number predicted with whole cell NSFA ( $N = 2214$ ). Due to the small size and the geometry of cones, long-term stable recordings (necessary for NSFA) of cone HCN currents were very challenging to obtain. However, recorded traces from cones gave an estimate of 526 fS, with 183 channels present per patch (figure 3.3 D), which is similar to the single channel conductance in rods. From this and the cone whole cell conductance ( $1.34 \pm .48$  nS), we estimate there are  $2021 \pm 725$  channels per cone. The comparable conductance and number of HCN channels in rods and cones is not surprising, because from analysis of the whole cell currents, we show the identity of the channels is the same, and the magnitude of the whole cell currents are similar (figures 3.1).

Our estimates of photoreceptor HCN conductance are comparable to the conductance reported for single HCN channels in rat cortical pyramidal neurons [66], which were also believed to be the HCN1 isoform. The significance of the similarity in conductance of HCN channels in photoreceptors and in pyramidal cells is twofold. First, this supports our whole cell and immunohistochemical evidence that the HCN1 isoform is the dominant isoform expressed in photoreceptors. Second, it indicates that the conductance of HCN1 channels is similar in different species, which is consistent with genetic evidence showing that HCN channels are highly conserved across species [59].

Comparison of the whole-cell and cell attached NSFA allows us to make estimates of HCN channel density and distribution. HCN currents could only be observed with cell-attached patches from the inner segment and cell bodies of rod and cone photoreceptors. This distribution is consistent with the proposed role of HCN channels as modulating the

photocurrent's electrical signal as it propagates from the outer segment to the synapse. On-cell patches typically showed 1/14 as many channels as the whole cell. We estimate that the average surface area of rod and cone inner segments are 586 and 508  $\mu\text{m}^2$ , respectively, from analysis of salamander retinal tissue sections [114]. Assuming the channel density is even throughout the inner segment, this would correspond to a density of 3.6 channels per  $\mu\text{m}^2$  in rods, and 4.0 channels per  $\mu\text{m}^2$  in cones. These estimates of HCN channel density in the inner segment of rods and cones are similar to results reported by cell-attached currents recorded from areas near the soma of rat cortical neurons [66]. Kole et al report that HCN channel varies exponentially from 9 - 550 channels per  $\mu\text{m}^2$  progressing from the soma to the distal end of the dendrites, an effect that had been previously noted in hippocampal pyramidal neurons [74].

### 3.3 Function of HCN Channels in Photoreceptors

#### 3.3.1 Simulated HCN current during rod light response

In order to determine HCN1 channel contributions to light evoked responses in photoreceptors, we simulated the light response of a rod photoreceptor, incorporating the data from our single channel conductance and whole cell studies of HCN1 channels (described above) into the simulation (figure 3.4 A). The numerical simulation model was developed with photocurrent data from the suction electrode technique experiments of Baylor et al [18], and our HCN channel data combined with models of other voltage gated currents, as developed by other salamander rod photoreceptor models [64, 73, 86, 88]. The simulation approximates

the voltage response of an actual rod photoreceptor at multiple light intensities (figure 3.4 A, B). By using actual data for the photocurrent (figure 3.4 D) and comparing the model response to the actual voltage response, we made every effort to make our model reflect not only the voltage response of a photoreceptor, but the contribution of individual ionic currents. Through the simulation, we were able to predict the time course and magnitude of the  $I_h$  current during the voltage response of a rod. Using our data for the single channel conductance, we were also able to estimate the number of HCN channels open at any given instant in time during a typical flash light response. The model predicts an opening probability  $P_o = .02$  at the dark membrane potential, which corresponds to an average of about 44 open HCN channels. This means that in darkness and at very dim light intensities, only a few HCN channels contribute to the resting potential. On the other hand, in response to a bright flash, HCN channels reach a peak open probability of  $P_o = .65$ , which corresponds to 1430 open HCN channels (figure 3.4 C). The model also shows that once they are opened by the fast initial hyperpolarization during the light response, HCN channels are slow to close after the sharp "nose" in the voltage response. This finding uncovers a potential advantage for the extremely low single channel conductance observed by our NSFA studies in photoreceptors. Namely, at a low opening probability, as in darkness and dim light, greater numbers of low conductance channels spontaneously opening and closing (as found with photoreceptor  $I_h$ ) would cause less noisy fluctuations in the membrane potential than small numbers of high conductance channels. This means that a low single HCN channel conductance could help improve the signal-to-noise ratio of rods in dim light.

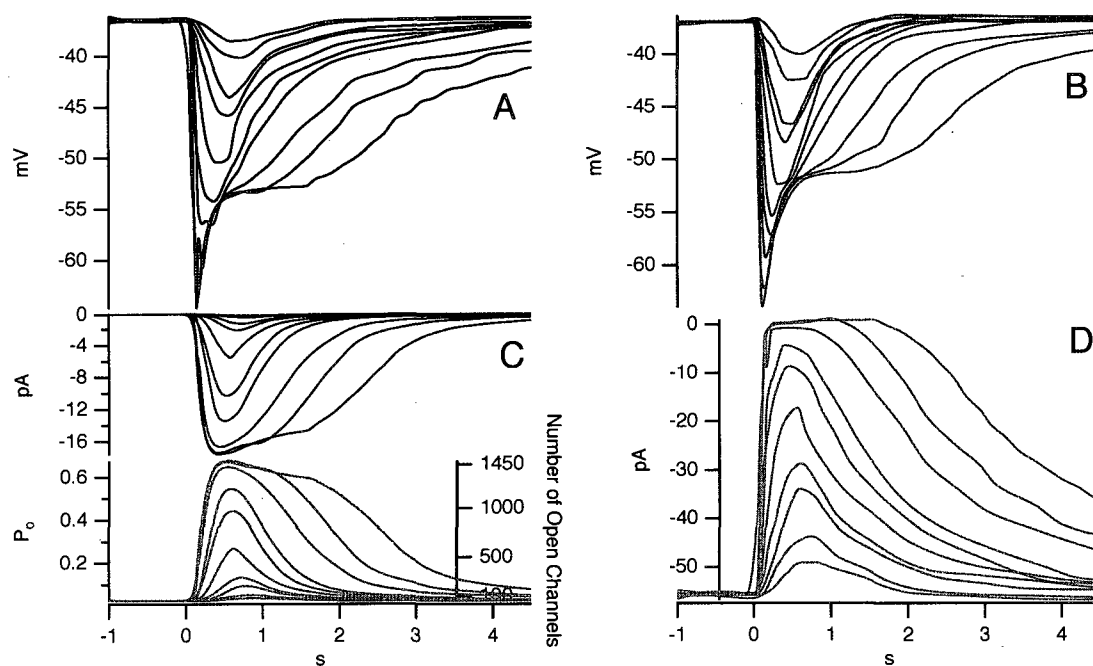


Figure 3.4 : Simulation analysis of rod photoreceptor function. (A) Simulated voltage response of a rod to increasing light intensities. (B) Actual voltage response recorded simultaneously with the photocurrent in (D) from an isolated rod. Data for (B) and (D) taken from Baylor et al, 1986. (C)  $I_h$  current and opening probability  $P_o$  with corresponding number of open HCN channels for each stimulus as predicted by simulation. Simulation parameters are given in Appendix A.3

### 3.3.2 HCN contribution to photoreceptor membrane frequency response

Frequency-chirped sinusoidal current stimuli according to equation 2.1 were injected into both rods and cones in order to examine the contribution of HCN channels to the electrical frequency response of these cells. All other currents were blocked (see Solutions in Methods), and the voltage responses were recorded (figure 3.5 A1 and B1). The magnitude of the Fourier transform of the stimulus and response were computed, and the impedance plotted as  $Z(f) = |V(f)|/|I(f)|$ . This analysis demonstrated that HCN channels cause a peak in the electrical impedance of both rod and cone photoreceptors at around 4 Hz, an effect equivalent to a bandpass filter (figure 3.5 A2 and B2, black traces).

Application of 100  $\mu$ M ZD 7288, which selectively blocks HCN channels [65, 94], was found to abolish the bandpass filter response (figure 3.5 A2 and B2, red traces). The frequency responses with HCN channels blocked with ZD7288 are those of a passive membrane, and equivalent to a low-pass filter. These results reveal that the bandpass filter effect seen when HCN channels are active arises because of a combination of an  $I_h$ -mediated high-pass filter, and a lowpass filter formed from the membrane resistance and capacitance. In other words HCN channels serve to lower the membrane impedance at low frequencies, which means the cell will be less sensitive to inputs at these frequencies.

From a theoretical perspective, a passive rod network would be modeled electrically with cells represented by the parallel combination of a resistor and capacitor, coupled to a neighboring cell of the same configuration by a resistor. This is the same as the cable equation (see section 5.4). Because the network has only parallel resistances and capacitances and no

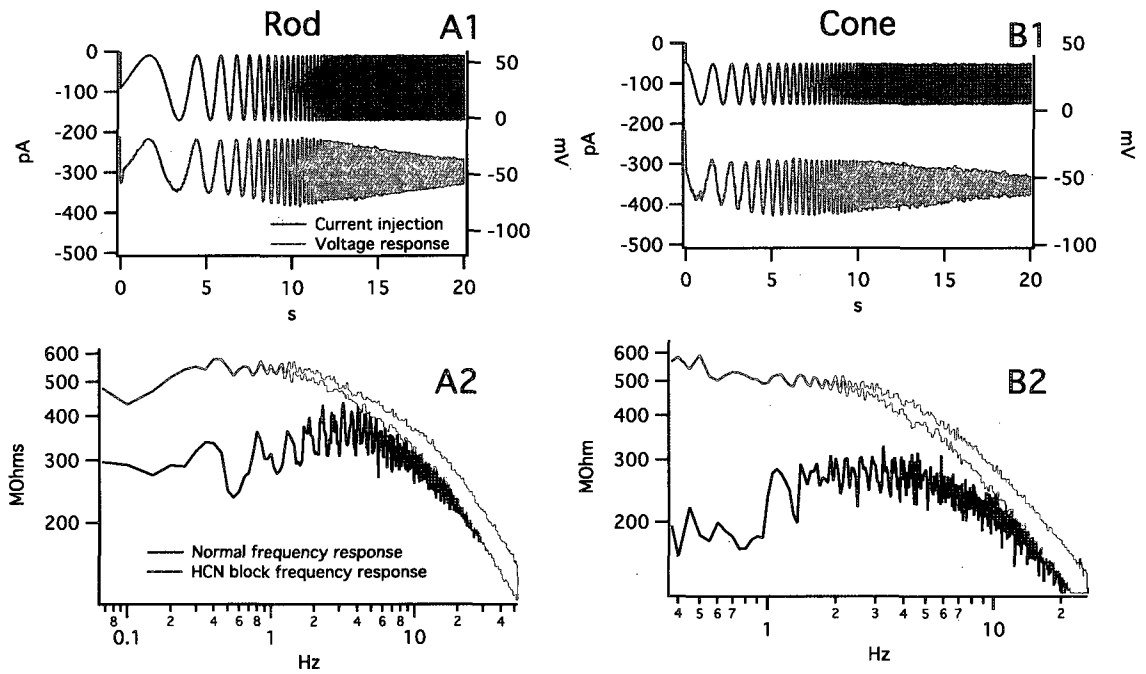


Figure 3.5 : Stimulus and response of a rod (A1) and cone (B1) to a frequency chirped sine wave current stimulus. Rod (A2) and Cone (B2) frequency response determined from stimulus and response, plotted on log-log axes. Application of ZD 7288, which blocks HCN channels, is shown in red. Normal rods and cones are seen to have a peak frequency response near 4 Hz. HCN channel block is seen to abolish the band-pass filter characteristic, leaving a low-pass filter resulting from the membrane capacitance and resistance.

series capacitance, it can act only as a low pass filter. Changes in passive membrane resistance by blocking  $I_h$  can only cause a shift in the cutoff frequency of the lowpass filter, and not the highpass filter characteristic observed in these experiments.

From an experimental standpoint, although our chirped current injection experiments were carried out in the whole mount retina, we were able to observe the same bandpass effect in cone photoreceptors as in rods. Salamander cones have been shown to have much weaker coupling to adjacent rods than rod-rod coupling, which would mean that if the bandpass filter effect were from the network, the effect should be much less for cones than rods. Because we instead observe a very similar bandpass filtering effect in cones and rods, it is likely that the effect comes from the electrical properties of HCN channels in individual cells, than from the coupled network. We believe that the bandpass filtering observed in this and other studies [115] is a result of active voltage gated conductances, such as  $I_h$ , and not the coupled rod network.

### 3.3.3 Equivalent circuit

With the realization that the electrical characteristics of the cell are equivalent to the combination of an HCN mediated high-pass filter and a low-pass filter from the cell membrane, an equivalent circuit can be constructed (figure 3.6 C). The voltage response of a rod and cone due to the  $I_h$  current at given input current can be modeled as a linear time dependent circuit [33, 34, 87, 103]. This circuit model has been studied before, and demonstrates what is referred to as the "inductive" property of the photoreceptors due to  $I_h$  [30, 33, 34, 87, 103].



We have extended previous work by using this model to create a linear approximation of the photoreceptor electrical response at different input magnitudes, and use this model predict the change in frequency response of the cell with stimulus intensity.

In the circuit, the capacitor  $C$  represents the membrane capacitance,  $R_m$  the membrane resistance, and the inductor  $L$  and series resistance  $R_1$  the contribution of  $I_h$ . The circuit works as follows: injected current charges the membrane capacitance with a time constant dependent on  $R_m$  and  $C$ . After a delay, the inductor  $L$  representing the contribution of HCN channels begins to turn on and shunt current through its branch of the circuit with a time constant dependent on  $L$  and  $R_1$ . This causes a sag in the voltage response, shown in figures 3.6 A and B.

To determine the values for the equivalent circuit, hyperpolarizing current pulses were delivered to rods and cones, and the voltage responses were recorded (figure 3.6 A and B). From these responses the parameters for each component of the circuit were estimated, and the corresponding frequency response predicted. Derivation of the model temporal response is given in Appendix A.1. The membrane capacitance and whole cell resistance were determined by fitting the first hyperpolarizing pulses that failed to activate  $I_h$ . Parameters for  $L$  and  $R_1$  at each input level were determined using a least-squares fit for the equivalent circuit voltage response. This model shows that as the hyperpolarizing input magnitude increases, the inductance  $L$  and series resistance  $R_1$  in the equivalent circuit decrease in both rods and cones (figure 3.6 A3,4 and B3,4). This causes a corresponding increase in the resonant frequency and damping factor (figure 3.6 A1,2 and B1,2). Derivation of the model

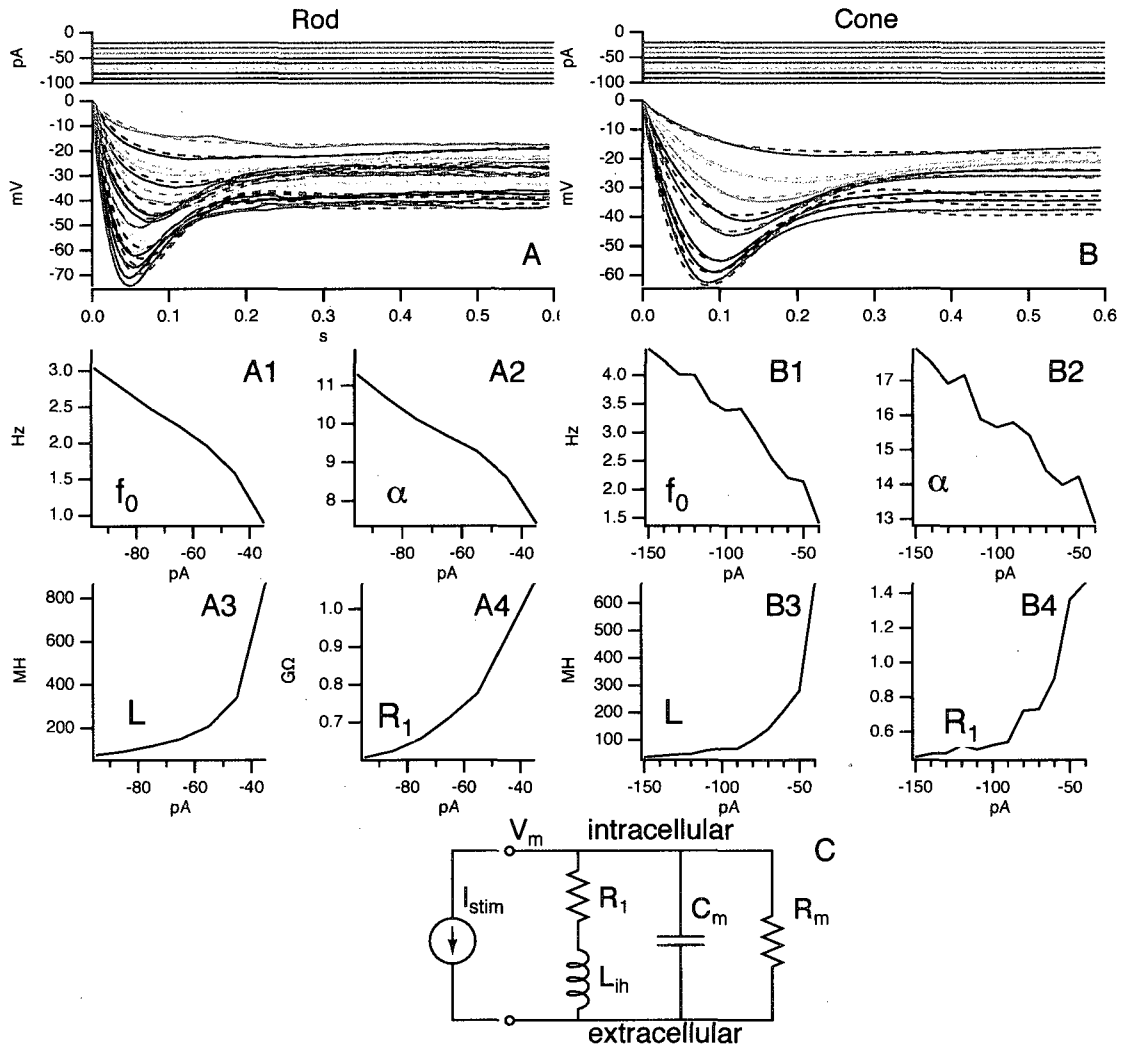


Figure 3.6 : (C) Inductive  $I_h$  model. Response of rod (A) and cone (B) photoreceptors to hyperpolarizing current steps (shown above) fit to the voltage response of the equivalent circuit (C) as a function of the parallel inductance  $L_{ih}$  and its series resistance  $R_1$ .  $L_{ih}$  (A3,4) and  $R_1$  (B3,4) decrease with increasing stimulus intensity. (A1, A2) show the circuit model predicted resonant frequency for the cell  $f_0$ , with damping factor  $\alpha$  shown in (A2, B2) as a function of the input current intensity. These parameters change as a function of  $L_{ih}$  and  $R_1$ . Derivation is given in Appendix A.2

frequency response is given in Appendix A.2. Plotting the model predicted frequency response demonstrates the shift in peak response for rods and cones with increasing stimulus strength (figure 3.7 A,B). These shifts, from about 2-4 Hz for rods, and from 1.5-3.5 Hz for cones, suggest that the HCN channels work to extend the operational frequency range for both rod and cone photoreceptors. This effect, along with the bandpass filter response, helps to quicken the voltage response of photoreceptors.

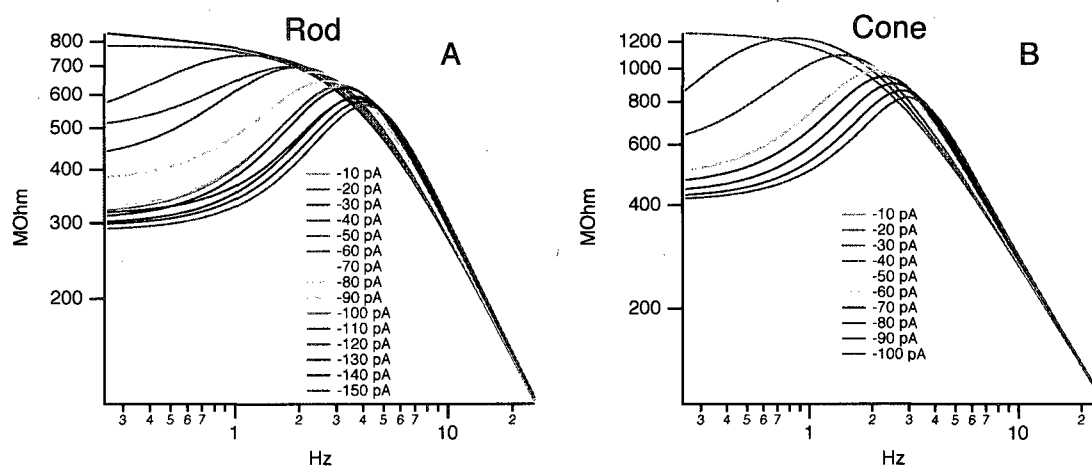


Figure 3.7 : Model (figure 6) predicted frequency response to electrical stimuli. (A) Frequency response of a rod photoreceptor predicted by the inductive model for each input magnitude. (B) Frequency response of cone photoreceptor. This demonstrates the HCN-mediated bandpass filter response of rods and cones at different input magnitudes. The resonant frequency shifts from 1 Hz to around 4 Hz for both rods and cones.

### 3.3.4 HCN channel shaping of photocurrent

Up to this point we have shown that the single channel conductance, whole-cell current, and electrical characteristics of the  $I_h$  current are very similar in rods and cones. However, results using light stimuli demonstrate that the effect of HCN channels on the light response

of rods and cones differs in accordance with the distinct function of these two cell types.

Applying 50  $\mu\text{M}$  of the HCN blocker ZD 7288 greatly increased the amplitude of the light response to a bright flash for both dark adapted rods and cones (figure 3.8 A1 and B1). In rods, blocking HCN channels abolished the transient “nose” present in the light response (figure 3.8 A1), while in cones, blocking it increased the response magnitude and appeared to eliminate the voltage overshoot present in the recovery phase (figure 3.8 B1). With HCN channels blocked, the light response magnitude and time course for rods and cones are both increased for flash stimuli. This means that HCN channels play a role in aiding recovery of from bright stimuli in both cell types from a dark-adapted baseline.

To measure the contribution of HCN channels to the frequency response of photoreceptors in response to light, their natural stimulus, chirped sine wave-modulated light stimuli were generated that ranged from .5 to 5 Hz for a rod over the course of 20 seconds (equation 2.1). These stimuli were similar to the electrical stimuli described previously, but in the form of light rather than current. Background illumination for 2 seconds adapted the retina to the average light intensity of the stimulus. In a normal rod the light stimulus produced a response of consistent amplitude from .5 to 1 Hz at  $1 \cdot 10^{-2}$  lux (figure 3.8 A2), falling off rapidly at higher frequencies (figure 3.8 A3). However, when HCN channels were blocked with ZD 7288, the response was much greater in magnitude, especially at low frequencies (figure 3.8 A2, red trace). The frequency components of the HCN blocked response were seen to decay beginning at .5 Hz, similar to a low pass filter (figure 3.8 A3). The decline at frequencies higher than 1 Hz was much more rapid than the falloff of the low-pass filter of

the electrical stimuli (figure 3.7), and had a lower cutoff frequency. This suggests that the components of this decay are due to the limited frequency response of the photocurrent, and not the low-pass filter of the cell membrane. Cones saw a similar increase in low frequency components with HCN channels blocked, although the light intensities to achieve this affect were greater ( $5.46 \cdot 10^{-2}$  lux). The voltage falloff at 1 Hz was less sharp than in rods, which is consistent with the faster kinetics of the cone photocurrent. Both rods and cones showed an increase in low frequency amplitudes, and greater frequency dependent decay with HCN block. Comparing the normal light frequency responses to those with HCN channels blocked demonstrates that HCN channels act as a compensator that cancels out the frequency-dependent decay in the light response over the range from 0 to 1 Hz. On a cellular level, slowly changing hyperpolarizing stimuli turn on HCN channels, which turn on and shunt the original stimulus, reducing its intensity.

### 3.3.5 HCN contribution to GWN estimated kernel (impulse response)

The impulse responses of rod and cone photoreceptors were estimated using gaussian-white-noise (GWN) light stimuli according to the Lee-Schetzen method [80]. A GWN stimulus approximates physiologic conditions for photoreceptors, with luminance in a visual scene fluctuating around a steady mean, as opposed to a flash stimulus, which measures the dark-adapted response to a single flash impulse. Briefly, the impulse response demonstrates the duration of time necessary for a system to respond to an infinitely brief stimulus. At dim light intensities ( $1.19 \cdot 10^{-2}$  lux), the impulse response of a normal rod is shown to increase

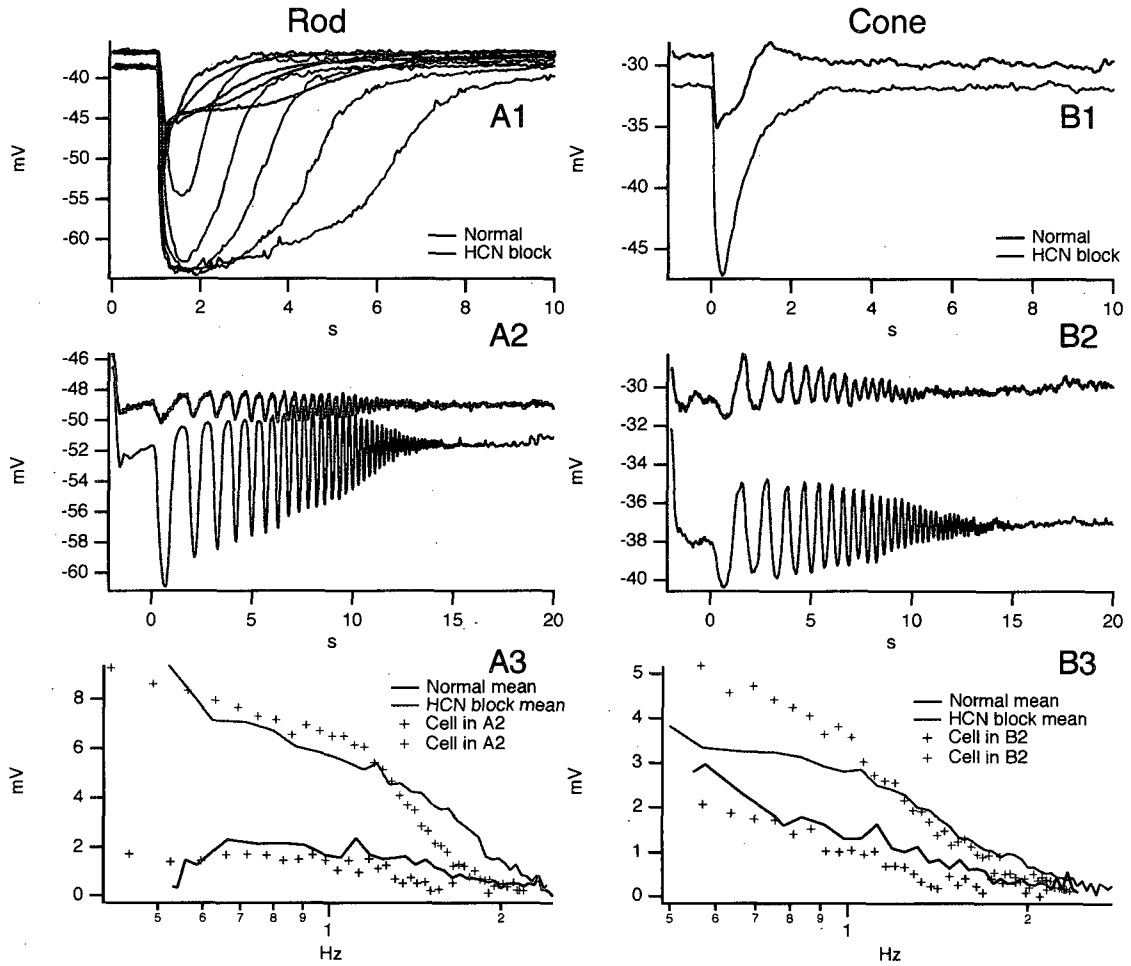


Figure 3.8 : (A1) Normal rod light response to flashes of increasing light intensity. (B1) Normal cone response to a flash of light. Response to the same stimulus after blocking HCN channels with ZD 7288 is shown in red. (A2) Rod and (B2) cone response to frequency-chirped light stimulus before and after HCN block. (A3) and (B3) demonstrate the amplitude vs frequency for chirped light stimuli. Solid lines show population means ( $n=4$  for A3 and  $n=3$  for B3), while crosses show the data for traces shown in A2 and B2, respectively. When HCN channels are blocked, a steady decay in the frequency response of both rod and cone photoreceptors, at dim and bright light intensities respectively.

in magnitude and duration when HCN channels are blocked with ZD 7288 (figure 3.9 A1). However, at brighter light intensities, the impulse response was relatively unchanged by blocking HCN channels (figure 3.9 A2). By shortening the duration of the impulse response, HCN channels reduce the amount of time necessary for rods to encode an impulse of information in dim conditions. The lack of effect at brighter intensities could be due to saturation of the rod light response. At a higher mean luminance level, impulses of light or darkness on top of the mean luminance are not able to cause significant changes in the rod voltage response, and as a result, these smaller fluctuations do not cause significant changes in HCN channel activation. Figure 3.8 shows that HCN blockade does not affect the light impulse response much at brighter mean luminances. HCN channels appear to be most effective for the normal operating state of rod photoreceptors—under dim light.

On the other hand, in cones, the impulse response to dim light ( $2.46 \cdot 10^{-2}$  lux) was seen to be relatively unaffected by blocking HCN channels (figure 3.9 B1). This is likely due to minimal HCN activation by cones at dim light intensities. At brighter light intensities ( $5.46 \cdot 10^{-2}$  lux), HCN block caused an increase in the magnitude and duration of the impulse response, similar to the change seen in rods at low light intensities (figure 3.9 B2). This implies that under brighter light, the normal operating condition for cones, HCN channels are functioning optimally, and help to reduce the amount of time needed to encode an impulse of information. The differential effect of dim vs bright light on the function of HCN channels in rod and cone photoreceptors coincides with the normal operating characteristic of these two cell types. Rods, which are sensitive to small changes in light intensity in dim

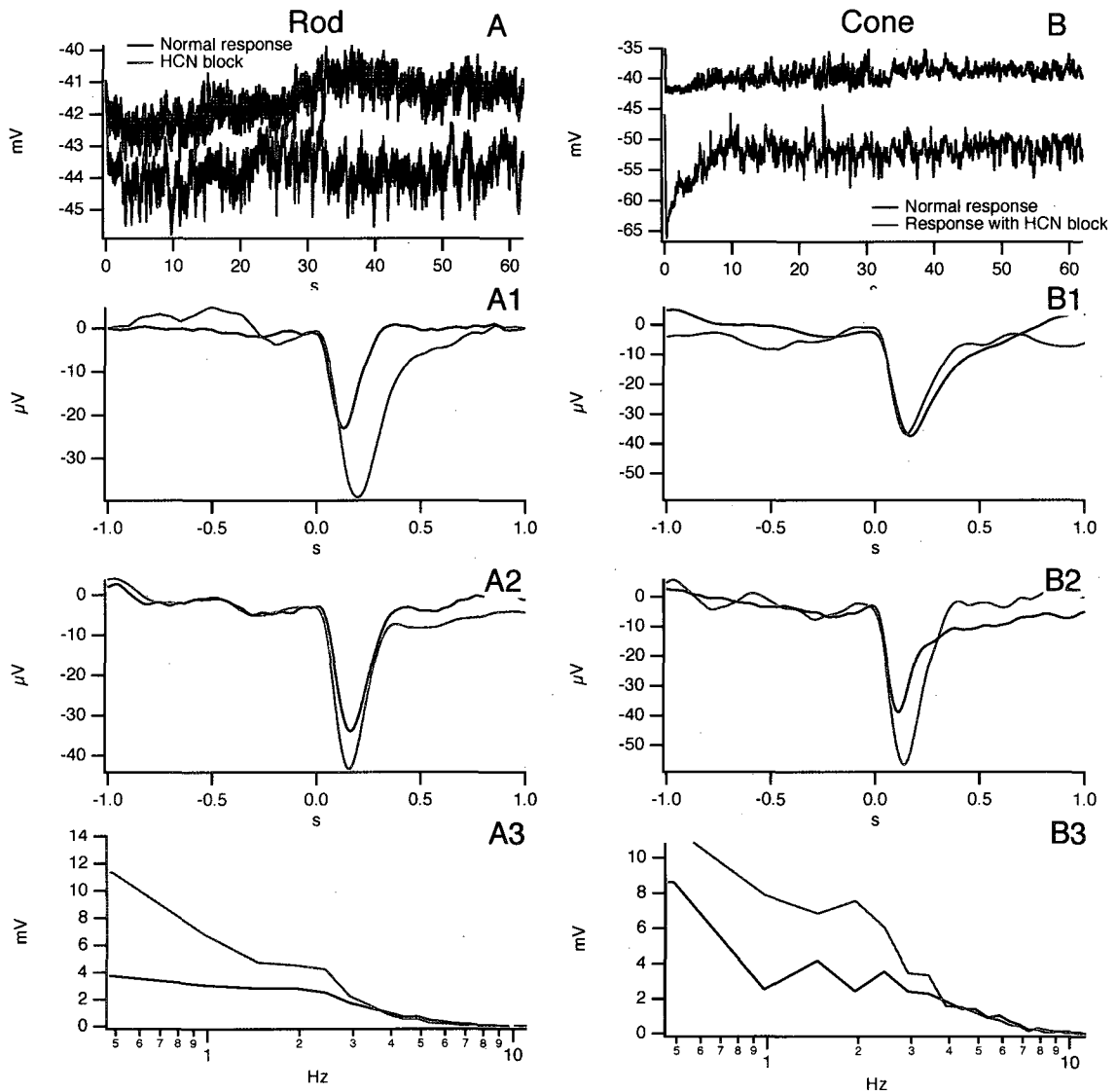


Figure 3.9 : (A1) and (B1) Estimated impulse response function (IRF) using a GWN stimulus in dim light for a rod and cone, respectively. Red traces show response with HCN block. (A2) and (B2) Estimated IRF at bright light intensities for a rod and cone, respectively. (A3) Shows the IRF predicted frequency responses for rod in dim light and (B3) shows the same for a cone in bright light. These plots are similar to the frequency response estimated directly in figure 8 A3 and B3.



light, see the optimal contribution of HCN channels in these conditions, whereas cones, which are sensitive to brighter light, see the optimal effect of HCN channels at brighter light intensities.

The Fourier transform of the impulse response gives the estimated frequency response from the GWN stimulus. This is shown for the rod and cone where HCN channels are effective—at dim and bright light intensities, respectively (figure 3.9 A3 and B3). These estimates of the rod and cone light mediated frequency responses are similar to our estimates using chirped light stimuli (figure 3.8 A3 and B3), with a frequency dependent decay at low frequencies in both rods and cones with HCN block. The similarity in the frequency responses predicted from the GWN technique and those from the chirped light stimuli confirms that photoreceptors have a mostly linear response component [79], and supports our use of GWN estimated impulse responses to approximate rod and cone function. It also shows how the changes in the rod and cone impulse response functions with HCN block correspond to the low-pass roll off characteristic seen with the frequency chirped light stimuli.

## 3.4 Discussion

### 3.4.1 $I_h$ in salamander rods and cones is mediated by HCN1 channels

In this study, we systematically investigate the biophysical and physiological properties of HCN channels in salamander rod and cone photoreceptors. We show that the  $I_h$  current in rod and cone photoreceptors is alike with respect to the whole-cell current magnitude, acti-

vation curve and time course, and that these values are characteristic of the HCN1 isoform (figure 3.1 A1-4, B1-4). Our whole-cell data from salamander rods is similar to reports from other researchers [1, 75, 78, 54], however, we use the intact retina to avoid the drawbacks of dissociated cells and standardize recording conditions for rods and cones. With whole-cell voltage clamp, we demonstrate that the activation time course of rod and cone  $I_h$  is similar to homogeneously expressed HCN1 channels (figure 3.1 A3, B3, table 3.1). Although the rod and cone half activation potentials are more hyperpolarized than the expressed HCN1 channels, this is a known difference between in vivo vs. expressed HCN1 channels [3]. While other researchers have shown that the HCN1 isoform is responsible for  $I_h$  in rabbit rods [31], we demonstrate that this is true not only for salamander rods, but also for cones. Our immunohistochemical and western blot experiments support our finding that HCN1 channels are responsible for the  $I_h$  current in rods and cones (figure 3.2). These results, which agree with experiments on the rat retina [83], show anti-HCN1 antibodies strongly labeling rods and cones. Our western blot experiments show the HCN1 antibody binds to a 60 kDa protein, which was also noted by Müller et al in the rat retina [83]. Given the specificity predicted by a BLASTp search (see Results and Methods) and demonstrated in the blot itself (figure 3.2 A1), we believe the 60 kDa protein represents a truncated form of HCN1 in the retina. Whether this product is active or not warrants further investigation.

### 3.4.2 Conductance of single HCN1 channels

By using NSFA, we provide the first known estimate of a single channel conductance in the retina. We show that photoreceptor HCN channels have a conductance of approximately 663 fS (figure 3.3), comparable to HCN1 conductance in rat cortical neurons [66]. This similarity is in line with evidence demonstrating that HCN channels are highly conserved across species [59]. We find that HCN channels are expressed in the inner segments of rods and cones, with approximately 2000 channels per cell. The density of these channels in the salamander rod and cone inner segment appears to be similar to the density of HCN channels near the soma of rat pyramidal cells, but less than the density near the distal ends of dendrites (see Results) [66, 74]. Of the many channels present, only a small number are active at the rod dark membrane potential (figure 3.4). With only a few channels open in dim light, the extremely low single channel conductance of HCN channels may be advantageous by minimizing membrane noise.

### 3.4.3 HCN1 channels create a bandpass filter in photoreceptors

To investigate how HCN channels affect the electrical properties of rods and cones, we examined the effect of HCN channels on their responses to extrinsic electrical stimuli. Using frequency-chirped stimuli, we demonstrate that HCN channels turn the low-pass filter characteristic of the rod and cone membrane into a band-pass filter, with a peak of approximately 4 Hz for both cells (figure 3.5). This is similar to observations of the frequency response in the dendrites of rat hippocampal neurons [84]. Although the bandpass filtering effect has

been investigated before in rod photoreceptors [30, 5, 17, 33, 34, 87, 103, 115], we show that cones also exhibit a similar bandpass filter effect, and that the frequency response of rods and cones varies with input intensity. By injecting hyperpolarizing steps of current into rods and cones we analyze a circuit analog for photoreceptors (figure 3.6 C), which predicts that the frequency response of the bandpass filter becomes more peaked and shifts to higher frequencies as stimulus intensity increases (figure 3.7 A, B). These effects are observed within individual photoreceptors, and are independent of the surrounding network.

#### **3.4.4 HCN1 channels help rods and cones efficiently encode impulses of light**

To investigate how HCN channels shape the light response of rods and cones, we use pharmacology combined with various light stimuli. With chirped light stimuli, we show that HCN channels act as a compensator, or damper, that normalizes the frequency dependent decay of the light response in both rods and cones (figures 3.8 A3 and B3). Using Gaussian white noise (GWN) light stimuli, we estimate the impulse responses of rods and cones at different mean luminances. We find that HCN channels reduce the amount of time needed for rods to respond to an impulse of information in conditions of low mean luminance (figure 3.9 A1), but that this effect saturates at brighter light intensities (figure 3.9 A2). Conversely, in cones, HCN channels reduce the time to respond to an impulse of information at brighter light intensities (figure 3.9 B2), but have little effect at dim light intensities (figure 3.9 B1). Previous work has done little to clearly explain the functional advantage of these channels other than describe the bandpass filtering effect  $I_h$  has on the rod network. Our analyses

show that in acting as a highpass filter, HCN channels reduce the time needed for rods and cones to respond to encode visual information in the optimal operating conditions for each cell type—dim light for rods, and brighter light for cones. One explanation for this effect is the difference in the photocurrents of each cell. Rods, which have a slow but high gain photocurrent, operate within the active voltage range for HCN channels at dim light intensities, but at brighter light intensities their photocurrent saturates, and is no longer able to be filtered by HCN channels. On the other hand, cones have a faster but lower gain photocurrent, which does not utilize the operational range of HCN channels unless the cell is stimulated with brighter light (figure 3.9). Therefore, although the biophysical and electrical properties of HCN channels are similar in rods and cones, the channels' effect on rod and cone light responses is specific to the distinct function of these photoreceptors.

Despite its importance in shaping the rod and cone light response,  $I_h$  is not the only ionic current that plays a role in bandpass filtering in rod photoreceptors.  $I_{Kx}$ , a potassium current, also plays a role in shaping the rod light response [19, 73], but its role in cones is still unclear [13].  $I_{Kx}$ , similar to  $I_h$ , exerts a depolarizing force on the membrane potential when the membrane is hyperpolarized. Traditionally,  $I_{Kx}$  is thought to be the primary mediator of high-pass filtering of small signals in rods because it is active around the dark membrane potential, while  $I_h$  is involved with filtering larger signals [19]. Contrary to these beliefs, we show that although  $I_h$  is minimally active at the rod dark membrane potential, it still affects the rod light response in dim conditions (figure 3.9). Therefore, it appears that both  $I_h$  and  $I_{Kx}$  are important in accelerating dim light responses.

### 3.4.5 Conclusion

In the retina, HCN channels appear to be necessary for the retina's temporal response to light stimuli. Blocking them reduces its ability to respond to quickly changing light stimuli [49, 48]. Although HCN expression is not limited to the photoreceptors [83], our results suggest that their role in photoreceptors can explain in part the loss of the retina's temporal resolution with HCN block. Changes in the rod and cone responses to flash, chirped, and GWN light stimuli with HCN block all show a significant slowing of the response kinetics. In light of these observations, it also makes sense that HCN1, the fastest of the four HCN isoforms, is dominant in these cells. Incidentally, we also find that HCN activation does not appear to be affected by background light, which is consistent with the very low cyclic nucleotide sensitivity reported for the HCN1 isoform [15].

In addition to elucidating how HCN channels function in photoreceptors, our study also sheds light on our understanding of the visual side effects of a new class of heart medications that target cardiac HCN channels to slow heart rate [24, 99]. The visual side effects of these drugs come from their action on HCN channels in the retina, which may well be due to blocking HCN channels in photoreceptors. Our work, which shows that HCN1 is the dominant isoform in rod and cone photoreceptors, suggests that newer cardiac drugs may be able to minimize visual side effects by selectively blocking HCN2 and 4, the cardiac HCN isoforms [24]. A newly developed HCN blocker, ivabradine, appears to exhibit some therapeutic properties in this direction, and may lead the way for a shift in treatment of patients with heart disease to more specific bradycardic agents [46, 45].

HCN Isoform	$V_{1/2} \pm \text{std}$ (mV)	$\tau \pm \text{std}$ @ -94 mV (ms)
Rod $I_h$	$-77 \pm .78$ (n=10)	$52.3 \pm 9.5$ (n=4)
Cone $I_h$	$-74 \pm 1.1$ (n=10)	$50.7 \pm 8.0$ (n=8)
HCN1	-69	84
HCN2	-95	557
HCN3	-77	1408
HCN4	-81	3586

Table 3.1 : **Kinetic parameters for  $I_h$  and HCN isoforms.** Kinetic data for both rods and cones are similar, and comparable to parameters from the HCN1 isoform. Data for HCN 1-4 come from measurements from homogeneous expression systems (Altomare et al., 2001, Stieber et al., 2005). The half activation voltage for HCN1 is known to be  $\sim 5$  mV more hyperpolarized in in-vivo systems than in the expression system (Altomare et al., 2001), putting it on par with measured salamander  $I_h$ .

## Chapter 4

### Functional Models of the Rod and Cone

#### 4.1 Interactions between $I_h$ and $I_{Kx}$ in the rod light response

##### 4.1.1 Introduction

During a photoreceptor light response many simultaneous membrane currents are summed by the cell to generate the voltage response. In turn, the voltage change of the cell alters the gating of each conductance through the voltage sensors of the channel. Through this non-linear action of voltage on gating, and the action of gating on voltage, different classes of ion channels influence one another's activity. Therefore, it is generally imprecise to classify the function of a single class of ion channel in a neuron outside the context of its peers. In this research addendum we describe one such interaction between  $I_h$ , mediated by HCN1 channels, and  $I_{Kx}$ , mediated by M-like potassium channels [107, 67] in influencing the membrane impedance of a rod during its light response.

In our work on HCN channels in salamander photoreceptors, we characterized their biophysical properties and investigated their functional role in tiger salamander (*Ambystoma tigrinum*) rods and cones [14]. From investigations of the gating kinetics and immunohistochemical staining, we showed that HCN1 channels are responsible for the  $I_h$  current observed in these cells. We used the HCN antagonist ZD7288 to block HCN1 channels in rods



and cones, and demonstrated that this increases the amplitude and duration of rod and cone light responses. When considered in the frequency domain, HCN block reveals the low-pass filter characteristic of the photocurrent [14]. This low-pass characteristic comes from the slowness of the photocurrent, whose gating depends on a complex cascade of molecular interactions. In contrast, the opening of voltage gated channels such as HCN channels depends on the motion of charged voltage sensors and their interactions with the pore, which is generally a much faster process [77, 76]. In normal physiological conditions, HCN channels reduce response amplitudes at low frequencies, flattening the frequency response of the cell to light stimuli [14]. This flattening allows the voltage response to be frequency independent over a wider range of stimulus frequencies, enabling the synapse to avoid saturation at low frequencies while still passing higher frequency signals. From a signal processing standpoint, this compensatory effect by HCN channels is analogous to high-pass filtering. Other studies previously described high-pass filtering in the rod network and postulated that it could be a way for the network to increase the signal to noise ratio for transient signals by spreading them over a larger area [33, 87, 103]. By dividing transient signals into networked rods, multiple parallel rod to bipolar cell synapses can be used, increasing the signal-to-noise ratio at the bipolar cell layer. In addition to their role in the rod network, other studies have also shown how high-pass filtering due to  $I_h$  is important in increasing the speed of the the individual photoreceptor light response [49, 30].

Although HCN1 channels appear to be major players in the rod and cone light response, they are not the only source of filtering by voltage-gated ion channels. Another current called

$I_{Kx}$  has also been shown to be involved in high-pass filtering of rod light responses, especially responses to dim stimuli [19].  $I_{Kx}$  is similar to the M-current in neurons in that it is a potassium conductance that is partially activated at resting potential, is further activated by depolarization, and is largely non-inactivating [67]. Kx channels also appear to be similar to EAG and Kcnv2 potassium channels, but its exact molecular origin is presently unknown [47, 27]. While both  $I_{Kx}$  and  $I_h$  are known to mediate high-pass filtering in rods, an important difference between the two is that during a light response (in which the rod membrane hyperpolarizes), Kx conductance decreases, while h conductance increases. Due to their different reversal potentials (-30 mV for  $I_h$  and -75 mV for  $I_{Kx}$ ), the net current change caused by  $I_h$  and  $I_{Kx}$  gating is inward during a light response, tending to counteract the initial hyperpolarization phase of the response [54, 19]. This reactive depolarizing effect leads to high-pass filtering of the input signal.

#### 4.1.2 Results

To extend our previous studies of the h-current, we examined the contribution of  $I_h$  to the rod light response when the Kx conductance, calcium conductance, and other potassium conductances are blocked. To do this, we recorded the rod light response with 5mM Co, 5 mM Ba and 20 mM TEA present in the bath [10, 43, 54]. Five flashes of light of increasing intensity were delivered to a rod and the voltage response was recorded. Then  $I_h$  was blocked with 50  $\mu$ M ZD7288 and light responses were recorded again.

In the presence of Co, Ba, and TEA, the rod's light response is smaller and occurs from a

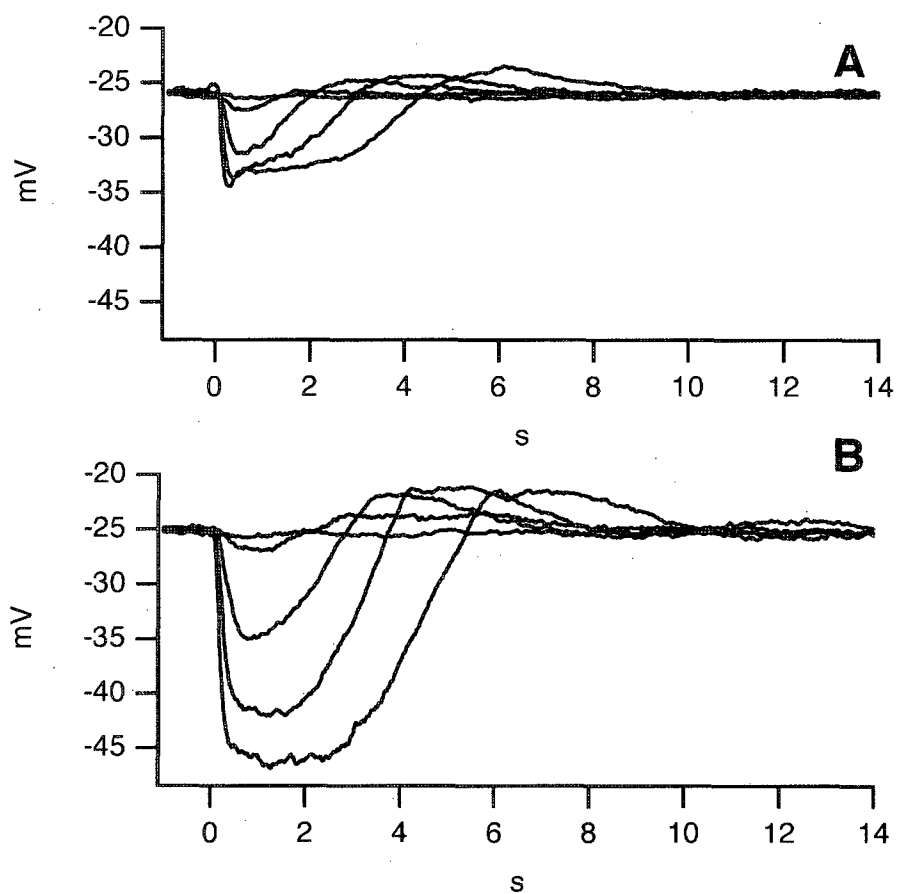


Figure 4.1 : A Rod response to flashes of increasing intensity in presence of TEA. B Rod response to same flashes with TEA + ZD 7288

more depolarized potential than in normal ringer solution (figure 4.1 A). Compare this with the simulation of a normal light response in figure 4.2 A. The depolarization in darkness is consistent with a reduction in the outward potassium current (due to  $I_{Kx}$  and other uncharacterized potassium conductances) that normally counteract the inward dark current. A small transient “nose” in the light response is seen due to the presence of  $I_h$  (figure 4.1 A).

When  $I_h$  currents are then blocked with ZD7288, the light response is seen to increase in magnitude and the transient “nose” is abolished (figure 4.2 B). This demonstrates that  $I_h$  can play a role light response recovery even when  $I_{Kx}$  is blocked. In both the solutions with and without ZD7288, an overshoot is seen following the recovery phase of the light response (figures 4.1 A and B). This is a known effect of TEA on the rod light response first observed by Fain et al., but unlike in other studies, the overshoots we observed failed to generate regenerative spikes due to the block of calcium currents with Co [73, 42]. The ionic current that causes this overshoot is not completely clear. Although our model could account for much of the shape of the waveforms in figure 4.1 A and B when Kx and h-conductances were blocked (data not shown), it failed to account for this overshoot. One potential source of the overshoot could be an uncharacterized effect of TEA and/or Co on the photocurrent, which the model did not include.

Although others have noted the complementary conductance changes by  $I_h$  and  $I_{Kx}$  during a light response, the magnitude and time courses of these changes are unknown. To evaluate the simultaneous contributions of  $I_h$  and  $I_{Kx}$  to the rod light response, we simulated the rod light response by solving differential equations describing voltage gated chan-

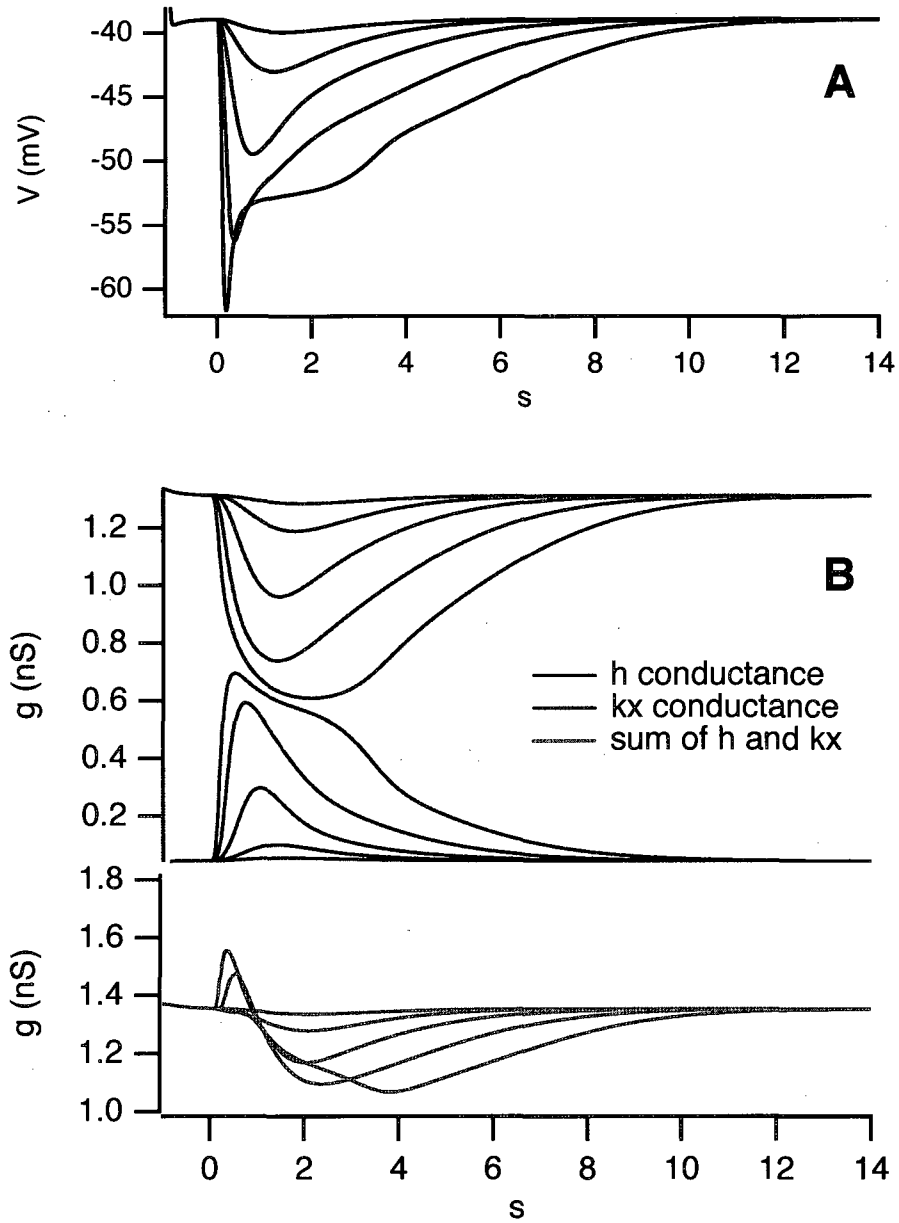


Figure 4.2: A Rod voltage response to flashes of increasing intensity. B Simulation predicted h-conductance, Kx conductance, and net conductance

nels and the photocurrent numerically (see Appendix A.3 for model parameters). The model was stimulated with five flashes of light of increasing intensity, and the time courses of the voltage,  $h$ , and  $Kx$  conductances at each flash intensity were evaluated. During a light response the voltage (figure 4.2 A) causes an increase in  $h$  conductance and a decrease in  $Kx$  conductance (figure 4.2 B). These complimentary conductance changes tend to counterbalance one another during the flash response, resulting in a reduced net conductance change whose amplitude is time dependent (figure 4.2 B, green traces). With large stimuli, the faster response kinetics of  $I_h$  cause a small transient conductance increase, followed by a longer lived conductance decrease due to  $I_{Kx}$ . Smaller stimuli cause a more synchronous activation of  $I_h$  and  $I_{Kx}$  (figure 4.2 B, green traces). In our model, the net conductance change due to both currents deviates no more than 0.3 nS from the resting level, whereas each individual conductance changes by nearly 0.6 nS. Although the conductance increase by  $I_h$  and decrease by  $I_{Kx}$  are not perfectly synchronized, together they halve the maximal conductance change of one current individually.

#### 4.1.3 Discussion

It has been observed using current pulse injection that, in contrast to cones, rods do not undergo an appreciable conductance change during a light response.[17] One explanation for this observation was that during a light response, an increase in  $h$  conductance counteracts the conductance decrease from the photocurrent.[17] This hypothesis does not account for the then unknown  $Kx$  conductance, and overlooks an important property of the pho-

to current. During a light response, the photocurrent, which is actually a shutting off of the inward dark current, causes hyperpolarization of the cell membrane. The dark current's instantaneous I-V relation is nearly flat throughout the rod's physiological voltage range, from -20 to -80 mV, in both light and darkness (Baylor and Nunn, figure 6) [18]. This property means that from the standpoint of the rod, the photocurrent acts as a current source whose magnitude depends on light, and not on the membrane potential. The consequence, which may seem counterintuitive, is that although the photocurrent is mediated by a closing of the ion channels carrying the dark current, the voltage-independence of the current through these channels means that it does not contribute to a membrane conductance change during a light response. There may, however, be a slow conductance change associated with the voltage dependence of the Na-Ca-K exchange pump.[60] It is important to note that unlike the rod, the cone dark current I-V relation is not flat, and therefore cones do undergo a conductance decrease when exposed to light.[112]

With the dark current ruled out as a source of conductance change, we conclude that the lack of observed net conductance change during a rod light response is likely due to the coordinated counterbalancing of h and Kx conductances, as we show with our simulation (figure 4.2). While the opposite conductance changes by  $I_h$  and  $I_{Kx}$  were first investigated some time ago [87, 103], the question remains as to what, if any, advantage these complementary changes would confer during a light response. One theory is that the two different conductance changes are a consequence of having two separate mechanisms ( $I_{Kx}$  and  $I_h$ ) for filtering small and large signals.[19] Alternatively, we propose that the answer to this

question may lie with the fact that rod photoreceptors are coupled to one another through gap junctions.

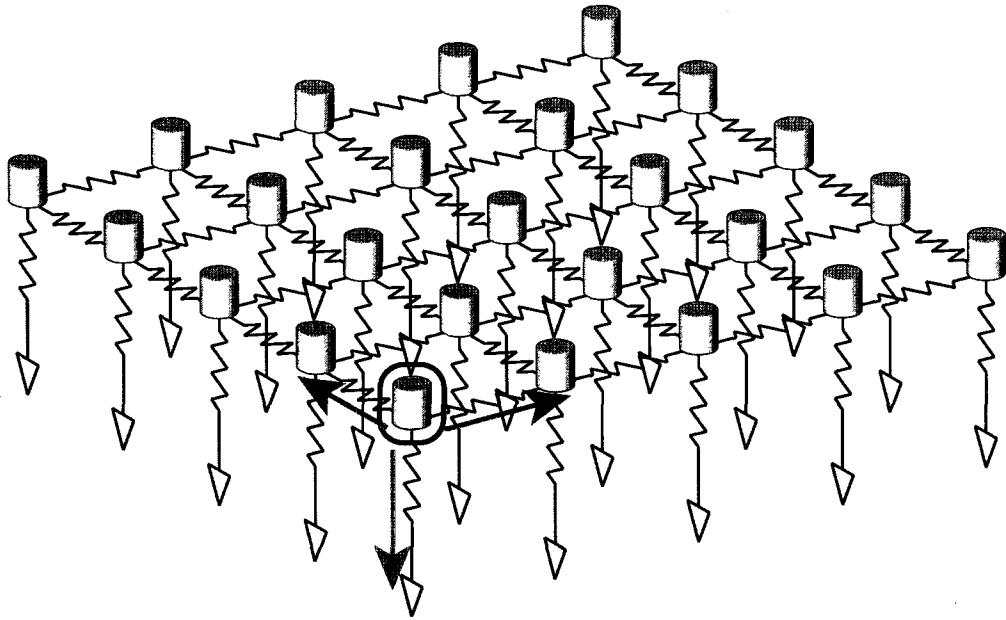


Figure 4.3 : Current flow in the rod network. The sum of the currents through the membrane of each rod equals the stimulus current in the source rod.

In the rod network (figure 4.3), signals propagate to adjacent rods through gap junctions in order to cancel random noise in individual cells and increase the number of parallel channels used in the rod to bipolar cell synapse.[115] One commonly overlooked aspect of the rod network is that the degree to which signals propagate through the network is dependent not only on the strength of the signal itself and the coupling impedance, but also on the membrane impedances of the cells in the network. With high membrane impedance (low conductance), signals tend to dissipate less (figure 4.3, green arrow) and propagate fur-



ther (figure 4.3, red arrow), and with low membrane impedance (high conductance), signals dissipate more readily. If  $I_{Kx}$  was absent and only  $I_h$  was present in rods, not only would high-pass filtering of input signals be reduced, but signals would dissipate more quickly due to unopposed h conductance increase (figure 4.3). If only  $I_{Kx}$  was present, then the propagation of signals in the network would be weighted to favor larger responses that completely turn off the Kx conductance. By having both h and Kx conductance, the cell achieves a high degree of filtering of input signals while minimizing the distortion of signal propagation in the network that would be a consequence of membrane conductance change.

We demonstrate that  $I_h$  filters the light response even when  $I_{Kx}$ , ICa and other potassium currents are blocked. This is further evidence that both currents are necessary for filtering of input signals to rods. While it has been previously shown  $I_h$  and  $I_{Kx}$  cause opposite conductance changes during a light response, the potential advantage of these complementary conductance changes has been unclear. Results from our membrane model of the rod show that the conductance changes from  $I_h$  and  $I_{Kx}$  do largely cancel one another, and that the time course of this net conductance change depends on the stimulus flash intensity. Further, we propose a potential advantage of the complementary conductances may be to maximize the amount of filtering by voltage gated channels while minimizing any perturbation of signal spread in the rod network. This would allow the cell to optimally spread signals from illuminated cells into adjacent rods for better use of the synapses between rods and bipolar cells.

## 4.2 Model of a cone

### 4.2.1 Feedback from horizontal cell to cone

The mechanism of action mediating the center-surround receptive field antagonism (CS-FRA) between horizontal cells and cones has eluded discovery since antagonistic feedback was discovered in cone photoreceptors. Early work suggested that the synapse may be mediated by gamma-Aminobutyric acid (GABA) receptors in the cone that gate a chloride current. This theory predicts that when horizontal cells hyperpolarize, they release decreasing amounts of GABA to the cone, causing a decrease in GABA receptor opening. If the equilibrium potential for chloride ( $E_{Cl}$ ) were very hyperpolarized, as is typical for many neurons, this would cause a depolarization in the cone membrane potential, as observed from cone voltage responses to surround light. It also implies that the cone membrane would see a net conductance decrease during a surround response. However, recent work has found  $E_{Cl}$  to be depolarized relative to the membrane potential, and direct application of GABA to the cone was found to have an inconsistent or no response [100, 102]. Furthermore, microelectrode recordings of salamander cones have demonstrated a net conductance increase during a surround response (Zhang, AJ, unpublished data). While other evidence for a role for GABA in the cone surround response exists, it appears that it cannot fully explain surround inhibition in cones.

Another theory of the feedback synapse originally put forth by Byzov and Shura-Bura [25] involves an ephaptic connection via gap-junction like hemichannels that causes direct changes in the cone membrane potential around voltage gated calcium channels in the cone

synapse. In this theory, hyperpolarization of the horizontal cell causes a hyperpolarization of the extracellular space around the cone synapse through leaky hemichannels in the horizontal cell membrane [63]. The local hyperpolarization of the cone extracellular membrane makes the voltage across the synaptic membrane appear more depolarized than the rest of the cone membrane. This depolarization causes the voltage gated calcium channels in the synapse to open more readily, causing more calcium flow into the cell. This theory is supported by evidence of hemichannels in the synapse [63, 41]. More recently, however, models of the resistivity of the extracellular fluid and analysis of the tightness of the connections between horizontal cell and cone have demonstrated that the effect of such an ephaptic synapse would likely be far too weak to cause any change in voltage across the cone membrane [40].

A third theory for the feedback synapse advocated by several researchers involves pH changes in the space around the synapse [104, 28, 55]. According to this theory, the horizontal cell releases protons into the synaptic space in darkness. Hyperpolarizing the horizontal cell causes a decrease in the proton release rate, causing an alkalization of the synaptic space. The alkalization of the space interacts with the calcium channels, increasing the current through them. One possibility for this activity is that the loss of positive charge in the synaptic space with alkalization causes an apparent depolarization of the membrane across the voltage gated calcium channels, just as with the hemichannel feedback theory. Evidence supporting the proton feedback theory is that changes in pH consistent with the feedback show a corresponding change in the calcium current in goldfish cones [55]. Addi-

tionally, an increase in pH buffering capacity in the extracellular solution appears to reduce the CSRFA in cone light responses [55].

Both the hemichannel and proton feedback theories cause feedback through a modulatory effect on the cone calcium current. However, it is unclear if the observed cone depolarization during a surround response could be due entirely to an increase in calcium current. Others have proposed that the effect on the calcium current must have a secondary effect on a calcium activated chloride current in order to cause a significant depolarization [68]. To assess the plausibility of these two theories, we built a model of the cone photoreceptor using data from the known cone ion channels and photocurrent. A block diagram for this model is shown in figure 4.4 A. This model includes sub-models of the photocurrent [97], h-current  $I_h$  [13], voltage gated calcium current  $I_{Ca}$ , internal calcium concentration  $[Ca]_i$ , and calcium activated chloride current  $I_{Cl(Ca)}$  [12, 68]. The flash response for the model is shown in figure 4.4 B. The model for the feedback begins with an external effector causing a left (negative) shift in the activation curve for the voltage gated calcium channels. It therefore accommodates both the hemichannel and proton feedback models. The leftward shift causes an increase in calcium current (figure 4.5 B), which over time causes an increase in internal calcium concentration (figure 4.5 C). The calcium current by itself causes a slight depolarization in the membrane (figure 4.5 A), but the main effect comes from a gating of a calcium activated chloride current. With  $E_{Cl}$  in the cone at -43 mV, hyperpolarization of the cone membrane potential with light causes gated the chloride current to be an inward current (figure 4.5 D), causing a depolarization in the cone membrane (figure 4.5 A),

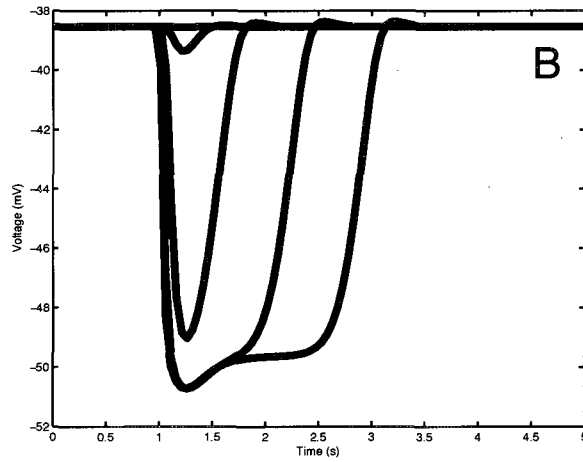
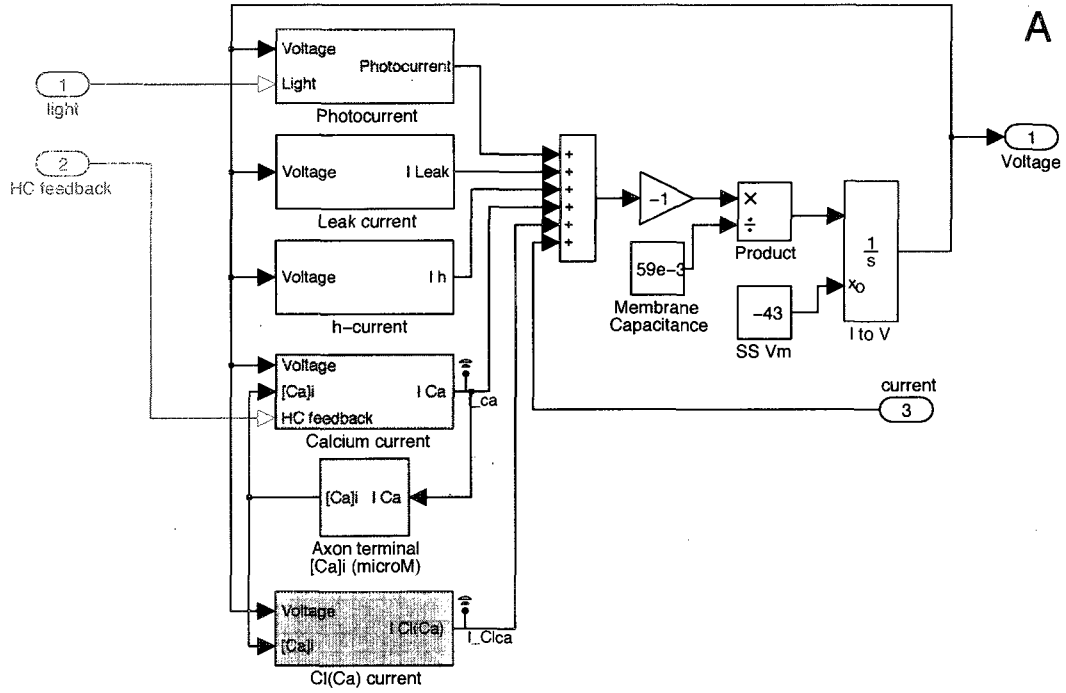


Figure 4.4 : (A) Block diagram for a model of a cone photoreceptor created in Simulink. Horizontal cell feedback causes a left shift in the activation curve of voltage gated calcium channels. (B) Response of the cone model to flashes of increasing light intensity.

consistent with the observed response.

The model predicts that the incremental change in calcium current with the feedback is too small to cause the observed depolarization in the cone membrane. It is only through the calcium current's effect on  $I_{Cl(Ca)}$  that a large enough depolarization can occur. Because the feedback requires the activity of the chloride current, the model also predicts that to observe an inhibitory feedback response, that the cone must be hyperpolarized by a light stimulus to generate enough driving force for the chloride current if  $E_{Cl}$  is -43 mV [102]. This prediction is consistent with our direct observations— cones must first be hyperpolarized with a center stimulus before an antagonistic surround can be observed.

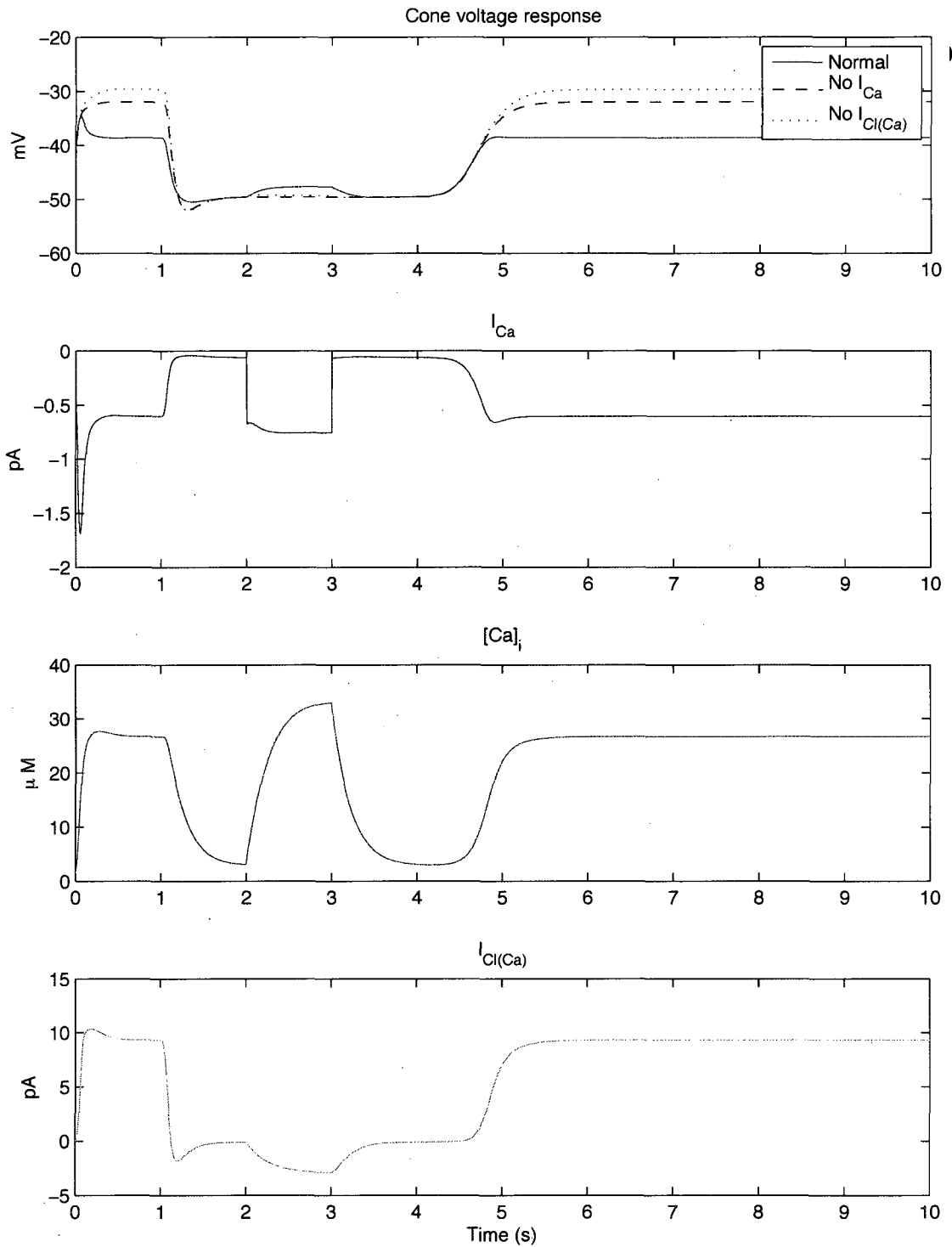


Figure 4.5 : Simulation of feedback from horizontal cell to cone. A step of light is applied to the cone at  $t=1$ , and at  $t=2$ , a feedback signal that shifts the voltage activation curve of the calcium current 10 mV to the left is applied. (A) The inhibitory depolarization is dependent on both the activity of the calcium activation curve and a calcium activated chloride conductance. (B) Shows the calcium current as a function of time. (C) Shows the calcium concentration in the cell, modeled with a first order buffering system. (D) Shows the calcium activated chloride current, which is the end effector causing depolarization in the cone.

## Chapter 5

### Electrical Coupling in the Rod Network

#### 5.1 Introduction

Electrical coupling between photoreceptors has been demonstrated in many species, including the turtle, the tiger salamander, the ground squirrel, and primates [69, 5, 35, 56]. Although the pattern of photoreceptor coupling varies between species— there are varying combinations of rod-rod, rod-cone, and cone-cone coupling in different animals, the purpose of this coupling appears to be the same across species. Coupling between alike photoreceptors (rod-rod, cone-cone) is thought to reduce noise by averaging out fluctuations in dark current activity in these photoreceptors. On the other hand, coupling between rods and cones is thought to provide a way for cones to make use of the rod bipolar cells at light intensities where rods approach saturation.

In transforming light signals into electrical signals, the retina creates a representation of the underlying information while minimizing contamination with noise. The first stage in this process, and the limiting factor in the baseline noise in the retina, is the conversion of photons into electrical signals by the photoreceptors. Noise intrinsic to photoreceptors comes from several sources including the photocurrent and ion channel activity. The photocurrent has two sources of noise: spontaneous thermal activation of rhodopsin molecules,



called discrete noise, and continuous variation in phosphodiesterase activity, called continuous noise. These intrinsic noise sources make extracting the signal from the background more difficult. Another major source of noise in photoreceptors is noise in the light stimulus that results from the poisson variability in photon arrival rates. Photon noise, called "shot noise" in other systems, is especially evident in dim conditions, so it is particularly relevant for the rod system. It makes estimating the intensity of the light source more difficult.

It is known that electrical coupling via gap junctions between rod photoreceptors reduces both intrinsic noise and extrinsic photon noise, at the expense of reduced spatial resolution. However, the exact nature of this tradeoff are unclear. Using parameters measured from the salamander retina, we demonstrate that coupling between rods results in an improvement in signal-to-noise ratio for nearly all perceptible stimuli. Investigating this effect in the salamander rods requires accurate measurements of the rod-rod coupling resistance, membrane resistance, and membrane capacitance. While estimates of salamander rod-rod coupling have been made using retinal slices [115], these measurements may overestimate the coupling resistance because connections between adjacent rods could be disrupted near the surface of the slice. In this study we estimate the rod-rod coupling resistance in the tiger salamander retina using both a bar light stimulus and electrical measurements using patch-clamp in the whole-mount retina. With this data, we demonstrate the functional consequences of rod-rod coupling on photoreceptor noise performance due to both intrinsic and extrinsic noise, and on image fidelity.

## 5.2 Measurement of coupling resistance using light stimuli

We estimated the space constant, the distance for the voltage to decay  $e$  fold, in the salamander retina using a bar shaped light stimulus, which is non-invasive and physiologic. We recorded the voltage response of rods and cones in response to a flashed bar of light stepped across the retina in  $5\ \mu\text{m}$  increments. With a bar shaped stimulus, the voltage distribution in the rod network is reduced from a two dimensional distribution to one dimension, simplifying our analysis. Light was projected onto the whole retina using a custom made projection system (see Methods), and voltage responses over two orthogonal directions were averaged. Figure 5.1A shows an image of the bar projected onto the retina. First, to assess the effect of light scattering by the retina on the stimulus, we measured the response of a cone to the bar of light. Because cones are only weakly coupled to rods, and because the background light of the projector largely saturated the rod response, this cone response represents the response of a single photoreceptor to the profile of the scattered light. Figure 5.1 B shows the example traces of the voltage response of a rod and cone to the bar stimulus.

With a  $-1$  log neutral density filter installed to attenuate the light intensity, we performed the same experiment on rods. The average maximum response for 6 rods measured several times over two directions was  $3.5\ \text{mV}$ . Without the  $-1$  log filter, the average peak cone response for several replications of two directions in 3 cells was  $6.4\ \text{mV}$ . Figure 5.1C shows the spatial profiles of the rod and cone response peaks centered around their maximal response. As expected, rods showed a slower falloff in their response than cones as the bar moved farther from the cell center. This effect is due to both coupling between rods, and

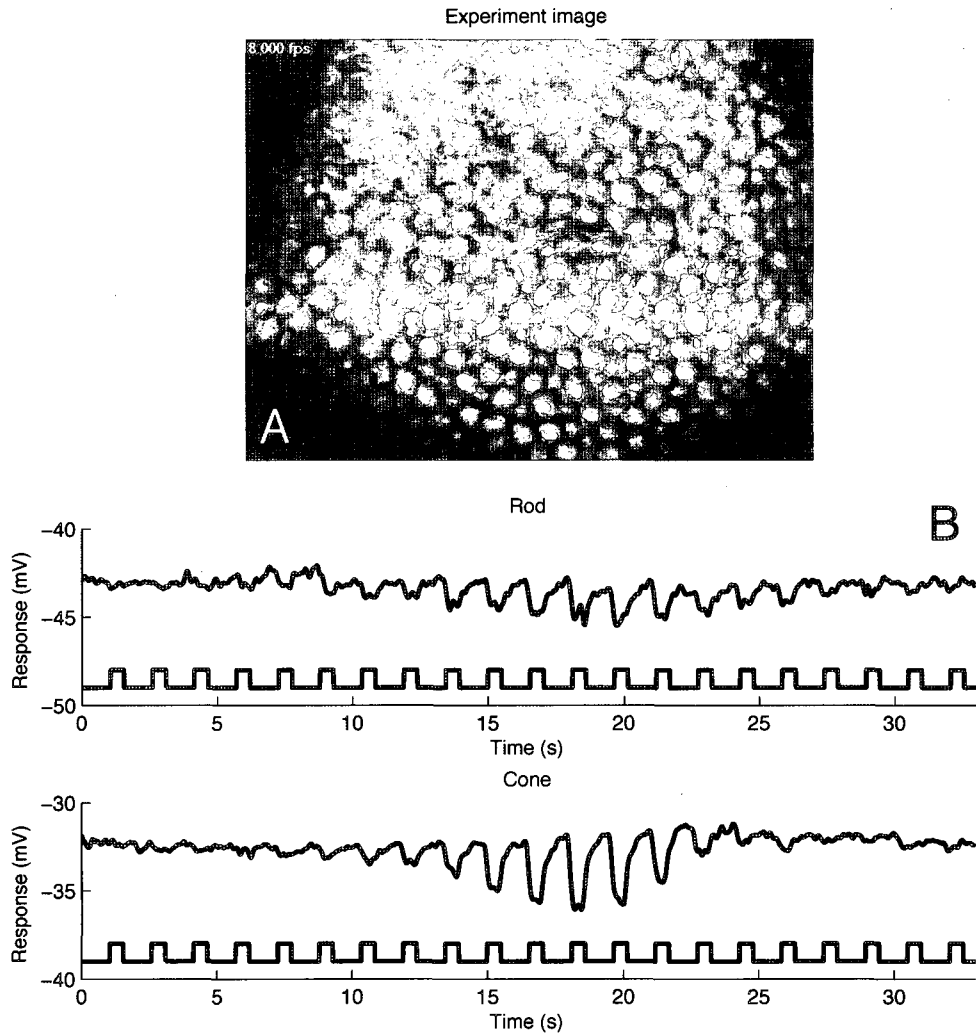


Figure 5.1 : (A) Image of whole mount retina during stimulus presentation, recording from a rod. (B) Example traces of current clamp recordings from a rod and cone with stimulus timing below.

increased rod sensitivity at low light intensities.

Because rods are only weakly coupled to cones, we use the cone as an in-vivo point source detector of the intensity of the light stimulus. In this way we could account for the profile of the scattered light in the retina that using a pinhole or slit and a photodiode detector could not. However, because the cone's intensity-voltage response relation is nonlinear, we had to transform the voltage response profile to the light intensity profile using the known cone I-V response curve to yield the profile of the actual light intensity (figure 5.2A). The light intensity profile, shown in figure 5.2 C, was narrower than the cone voltage response profile due to the cone's increased gain at lower light intensities.

After computing the light intensity profile of the stimulus, we calculated the theoretical isolated rod response by transforming the light intensity, divided by 10 to account for the additional ND filter, to rod voltage response' (figure 5.2 D). This transformation was done using the rod response to whole field flashes of known intensity. Because the background light from the projector system changes the rod light response, the I-V relationship was assessed both with and without the background light of the projector (figure 5.2 B). A small rightward shift in the I-V curve and a lower saturation threshold was seen in the presence of this background light (figure 5.2 B).

Ideally, the isolated rod response should be the same as the response of a rod to a whole field stimulus of the same intensity, because whole field flashes "uncouple" the rod network by homogeneously hyperpolarizing all rods together, preventing current flow between them. It is this principle that allows us to extract the contribution of rod-rod coupling from the

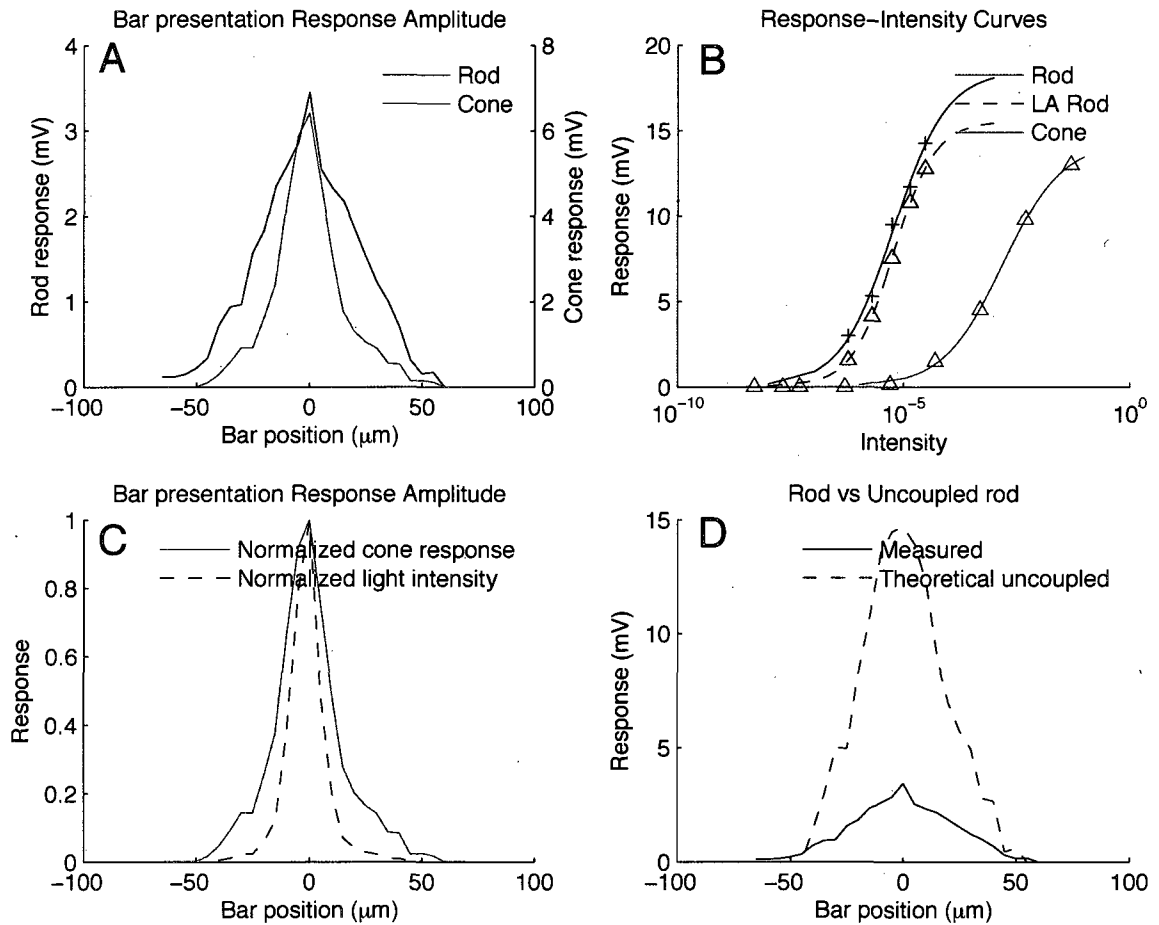


Figure 5.2 : (A) Average maximum response amplitudes for rods ( $n=6$ ) and cones ( $n=3$ ) averaged over two directions. (B) Maximum response amplitude vs logarithmic light intensity of a whole-field flash stimulus for dark adapted and background light adapted rods and cones fit with the Hill equation  $V = A/(1 + (K_{1/2}/x)^n)$ . (C) Normalized cone response compared with cone stimulus transformed by cone response sensitivity in B to yield stimulus intensity. (D) Measured rod response compared with theoretical uncoupled rod response from transforming stimulus intensity from C with rod sensitivity in B.

spatial response of a single rod.

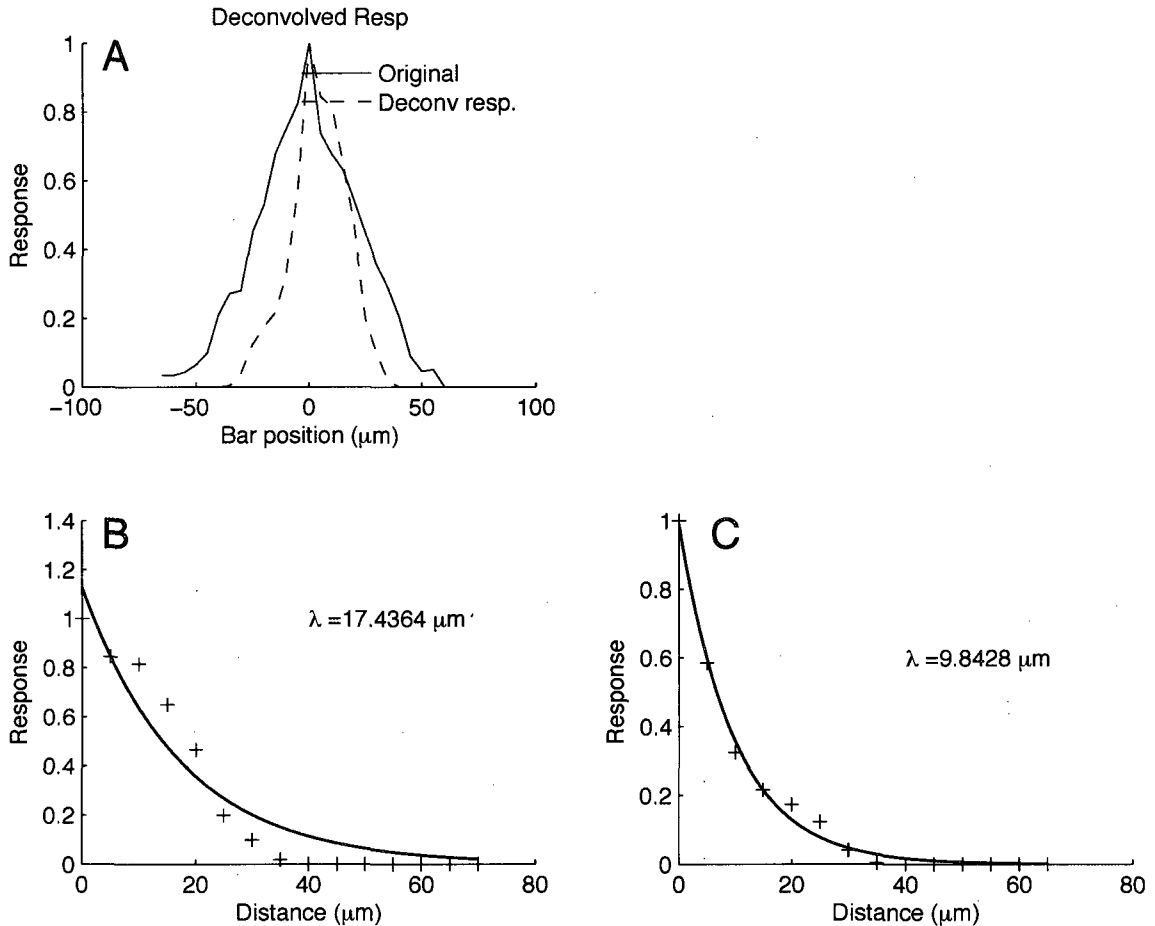


Figure 5.3 : Estimated space constant of rod network. (A) Normalized rod response compared with rod response deconvolved with theoretical isolated rod response from figure 5.2 D. (B, C) Each side of the deconvolved response fit with a single exponential decay  $r = k \exp(-x/(\lambda_{1D}))$ . Values of  $\lambda$  of 17.4 and 9.8  $\mu\text{m}$  correspond through equation 5.5 to  $\gamma = 0.91$  and 3.31, respectively. Assuming an isolated rod membrane impedance  $R_m \approx 300 \text{ M}\Omega$ , these values of gamma predict a coupling resistance  $R_c$  of 272 and 994  $\text{M}\Omega$ .

Figure 5.2D shows the theoretical isolated rod response to the light bar compared to the actual rod response in the network. The theoretical isolated rod response has a larger amplitude than the actual response due to an absence of signal spread to coupled rods. Next,

we deconvolve the networked rod response with the theoretical isolated rod response to yield a unit-less response profile that represents the contribution of coupling on the rod response (figure 5.2D). Deconvolving the networked response with the theoretical isolated rod response eliminates both the nonlinearity present in the rod light response sensitivity, as shown in figure 5.2 B, and the contribution of light scattering that would otherwise confound our analysis.

As expected, the resulting response profile is narrower than the actual rod response. By fitting single exponential decay of the form of 5.4 to the ideal network response, we calculate the space constant on each side of the ideal response profile, yielding values of  $\lambda_{1D} = 17.4$  (Pearson's  $R=0.955$ ) and  $9.8 \mu\text{m}$  ( $R=0.997$ ), as shown in figure 5.3 B and C.

Assuming a cell spacing  $D = 16 \mu$  [8],  $\lambda_{1D}/D = 1.09, 0.61$ . Using the relation for a 1-dimensional network, equation 5.5, the ratio  $\gamma = R_c/R_m$  of coupling resistance to membrane resistance was calculated, which corresponds to values of  $\gamma = 0.91$  and  $3.31$ , for the  $17.4$  and  $9.8 \mu\text{m}$  measurements respectively [69]. Assuming an isolated rod membrane impedance  $R_m = 300 \text{ M}\Omega$ , these values of gamma would correspond coupling resistances  $R_c$  of  $272$  and  $994 \text{ M}\Omega$ . Table 5.1 outlines these values.

### 5.3 Measurement of coupling resistance using electrical stimuli

Whole cell patch recordings of adjacent rods were made in the whole retina in order to measure the coupling resistance between rods in the network. Voltage clamp steps from  $-120$  to  $+20 \text{ mV}$  applied to one cell caused currents in an adjacent cell which was clamped at  $-40$

Parameter	Dir. 1	Dir. 2
Length constant $\lambda_{1D}$ ( $\mu\text{m}$ )	17.4	9.8
Pearson's R	0.955	0.997
Normalized $\lambda_{1D}/D$ (cell lengths)	1.09	0.61
$\gamma = R_c/R_m$	0.91	3.31
Estimated $R_c$ ( $M\Omega$ )	272	994

Table 5.1 : Rod network parameters estimated using a bar light stimulus. Two estimates are given- one for each side of the exponential decay.



mV, which is near the rod resting potential. These experiments demonstrate the resistance between two cells in the network, but this is different from the coupling resistance  $R_c$  which is between two rods. In these patch clamp experiments, current flows between all other electrical paths in the network, and not just the gap junctions between two adjoining cells. When the length constant  $\lambda$  is short, the measured resistance using the dual patch technique will approach the coupling resistance  $R_c$ , because the majority of the current will flow directly between two rods.

The network resistance between two adjacent cells, referred to here as the apparent resistance,  $R_a$ , is a useful parameter because it can be measured directly from the retina without making any assumptions about the topology of the network connections or input impedances\* of individual cells. This network measurement of  $R_a$  serves as a lower bound on the possible resistance between adjacent cells  $R_c$ . Iterative solving of a linear model of the two-dimensional rod network shows that the actual resistance  $R_c$  should be near 10% higher than  $R_a$ .

The network resistance and conductance (apparent resistance  $R_a$  and conductance  $g_a$ ) between cells are defined as:

$$\frac{1}{g_a} = R_a = \frac{\Delta v_{1-0}}{i_1} \quad (5.1)$$

Where  $\Delta v$  is the voltage difference between driver and follower cell, and  $i_1$  is the current in the follower cell.

---

\*By voltage clamping each cell, the voltage across the coupling resistance through the network is held constant by the amplifier, at least in the cells recorded.

The I-V relationship for the current flow between two rods is shown in figure 5.4 C. The black line shows the value of the initial transient current flow in the follower cell. This is thought to represent the current flow due to electrical coupling between the cells through the network. The red trace shows the steady-state value of the current flow, which occurs after voltage gated ion channels have altered the current flowing through adjacent cells. The current flow through directly from driver to follower cell should not be affected by gating of currents because these cells are held voltage clamped. However, adjacent cells do not have their membrane potentials clamped, and therefore the voltage of the driver cell will alter the current flow through these adjacent cells as this voltage causes a gating of ion channels. The difference between the initial and steady-state values shows the importance of the indirect current flow through the network.

The I-V relationship between the two cells was linear in both the initial and steady-state phases, except at very hyperpolarized voltages, where  $I_h$  is active in adjacent cells, and at depolarized voltages, where voltage gated potassium channels activate. This is evidence that the gap junctions between cells are purely resistive, and do not have voltage dependent changes.

The average network resistance between all cells recorded was  $890 \pm 10 \text{ M}\Omega$  (SEM) from the initial current, and  $1120 \pm 13 \text{ M}\Omega$  from the steady-state current. Most of the recordings were made between pairs of cells, reversing which cell was the driver and follower cell. In order to directly compare our results with previous measurements of rod-rod conductance [115], the results were tabulated as conductances rather than resistances. Table 5.3 shows the conductance values for recordings made in each pair. Analysis of Variance (ANOVA)

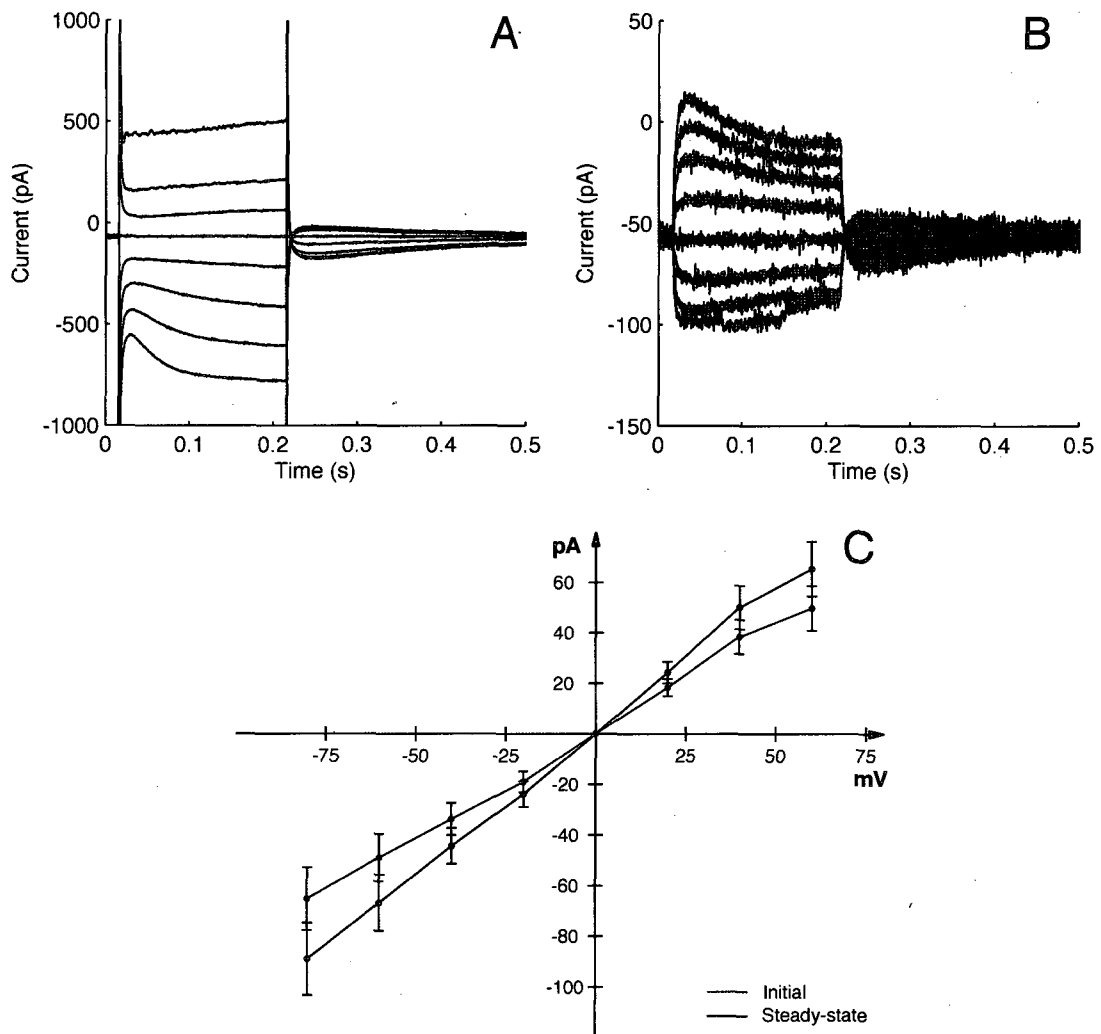


Figure 5.4 : Dual patch recordings between adjacent rods in the whole retina. (A) Example current flow in the driver cell in response to voltage steps from -120 to +20 mV. (B) Example current flow in the follower cell held at -40 mV in response to driver cell command voltage changes. (C) I-V relationship for dual patch recordings showing initial (red) and steady-state (black) currents. Average network resistance between all cells recorded was  $890 \pm 10 \text{ M}\Omega$  (SEM) from the initial current, and  $1120 \pm 13 \text{ M}\Omega$  from the steady-state current. Data comes from 24 trials (11 pairs + 2)

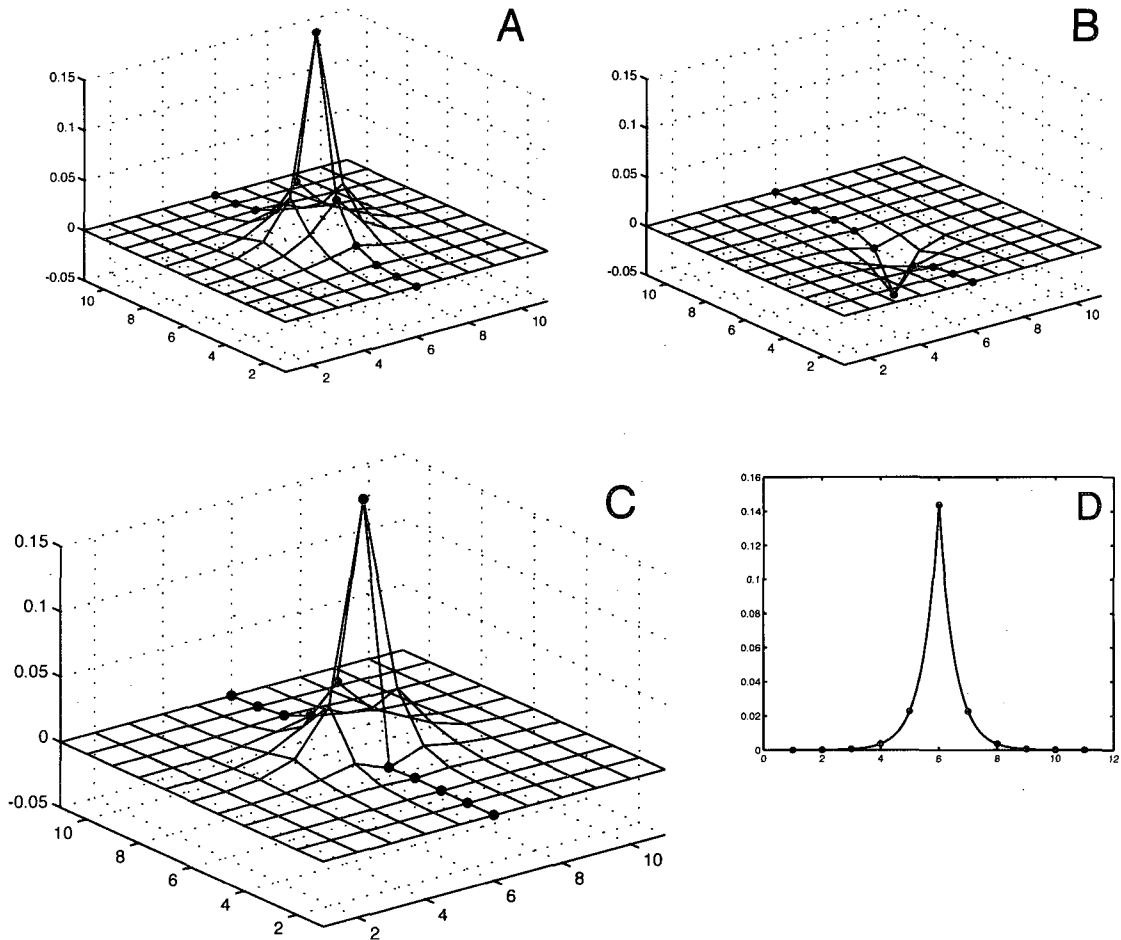


Figure 5.5 : (A) Simulation of the network voltage response to a unit step of current input into the middle cell  $v_{0,0}$ . (B) Simulation of the network voltage to a step of current with value  $i_{0,1} = -\frac{v_{0,1}}{R_{in}}$ . (C) Injecting a unit current and value  $i_{0,1} = -\frac{v_{0,1}}{R_{in}}$  simultaneously creates a superposition of the voltage responses in A and B, where  $v_{0,1} = 0$ . (D) A profile of the 2D solution in A fit with a single exponential decay.

performed on the pair data indicates that most of the variability comes from differences in the coupling between pairs, indicating that the recordings are consistent when the driver and follower cell are reversed. This agreement in the reciprocal conductance demonstrates not only that our technique is reproducible, but that there is an absence of any rectifying element between the two cells.

While the network conductance between cells is an interesting parameter because it can be measured directly, it is not useful in formulating a model of the rod network. However, by knowing the network input impedance for a point source of current  $R_{in2D}$  and the normalized length constant  $\lambda_{2D}/D$ , the membrane resistance  $R_m$  and coupling resistance  $R_c$  can be determined. For the dual patch experiments,  $R_{in2D}$  and  $\lambda_{2D}/D$  were determined according to the assumptions and derivations given in section 5.5. It is important to note that due to the difference in topology, values for  $R_{in2D}$  and  $\lambda_{2D}/D$  are different for the same  $R_c$  and  $R_m$  in the one-dimensional network analyzed in section 5.2.

From section 5.5:

$$R_{in2D} = 137 \text{ M}\Omega$$

$$\lambda_{2D}/D = 0.53$$

From figure 5.7 C, this corresponds to a ratio  $R_{in2D}/R_m \approx 0.5$  and  $R_c/R_m \approx 3.4$  which means

$$R_m \approx 274 \text{ M}\Omega$$

$$R_c \approx 931 \text{ M}\Omega$$

Pair #	Network Conductance (nS)		Mean
	Direction 1	Direction 2	
1	1.50	1.40	1.45
2	1.42	1.41	1.41
3	1.54	1.47	1.51
4	0.66	0.62	0.64
5	0.82	0.85	0.83
6	0.56	0.54	0.55
7	1.05	0.94	0.99
8	0.74	0.74	0.74
9	0.51	0.53	0.52
10	1.48	1.53	1.50
11	2.42	–	2.42
12	1.90	–	1.90
13	0.92	0.85	0.89
Grand mean $\bar{x} = 1.12$			
Grand sum of squares $T_{SS} = 3.12$			
Sum of squares between pairs $B_{SS} = 3.11$			
Sum of squares error $E_{SS} = 0.02$			

Table 5.2 : Network conductance values for adjacent rods from initial data, with results of ANOVA analysis given at the bottom. Single measurements (11 and 12) are excluded from ANOVA. The sum of squares error is small in comparison to the total sum of squares, indicating that there is good agreement in measurements made in either direction. The mean  $\bar{x} = 1.12 \text{ nS} = 0.89 \text{ G}\Omega$ .

## 5.4 Cable Theory

Now that we have an estimate of the coupling resistance and membrane resistance between cells, it makes sense to use them to explain how these values will affect the representation of

visual scenes in the rod network. Generally, rod-rod coupling reduces the spatial resolution of a visual image because signals are allowed to "diffuse" into neighboring rods. In exchange, noise in adjacent rods is reduced by averaging the noise over a larger area, making individual rods less noisy. In order to answer the question of how coupling between salamander rods improves the signal-to-noise ratio in visual scenes, we use the measurements made in the first part of this work to create a linear, two-dimensional model of the salamander rod network.

#### 5.4.1 Cable equation in one dimension

The cable equation describes the electrical potential as a function of time and space in a lossy conductor when current is injected along its length. Such a conductor has terms representing the resistivity, distributed radial capacitance, and radial loss resistance, and gives rise to the differential equation 5.2. The originator of this equation is William Thompson, who studied it in describing the electrical losses in the first undersea cable between the US and Britain for telegraph communications, built in the mid 19th century. At that time there was no way to amplify the signal in the cable as it lay beneath the Atlantic ocean, so the quality of the conductor was very important. From his theoretical analysis, he advocated new ways of manufacturing to reduce the parasitic capacitance and resistance. For work on the submarine telegraph cable and thermodynamics, Thompson was knighted, and later adopted the title of Lord Kelvin [21]. More recently, the cable equation has been used extensively in neuroscience to describe the propagation of electrical potential along the axons and dendrites

of neurons.

Figure 5.6 A shows a diagram of a neuronal cable, with axial specific resistance  $R_a$ , distributed radial resistance through the membrane  $R_m$ , and distributed capacitance  $C$ . This cable is analogous to a one-dimensional section of rod photoreceptors, shown in figure 5.6 B, with rod membrane resistance  $R_m$ , membrane capacitance  $C$ , and  $R_c$  the coupling resistance to an adjacent rod.

The current flow through an infinitely long section of cable of the form given in figure 5.6 gives rise to the following differential equation:

$$\frac{v}{R_m} + C \frac{\partial v}{\partial t} - \frac{1}{R_a} \frac{\partial^2 v}{\partial x^2} = i \quad (5.2)$$

where  $u$  is a function of  $x$  and  $t$ . The general solution† for the voltage in a one-dimensional infinite cable as a function of time and space is:

$$G^*(x, t) = v(x, t) = \sqrt{\frac{R_a}{C}} \frac{1}{\sqrt{4\pi t}} u(t) \exp\left(\frac{-x}{C r_r}\right) \exp\left(\frac{-C R_a x^2}{4t}\right) \quad (5.3)$$

for a point source of current that is impulsive in time ( $i(x, t) = \delta(x)\delta(t)$ ), where  $u(t)$  is the Heaviside step function. The derivation for this solution is given in section A.4 of the appendix.

By solving for an impulse (point) of current in space and an impulse (flash) in time, the solution can be solved for any time vary current by superimposing a scaled version of this response for each point in a known stimulus distribution through time and space. The time

---

†This solution is derived in section A.4



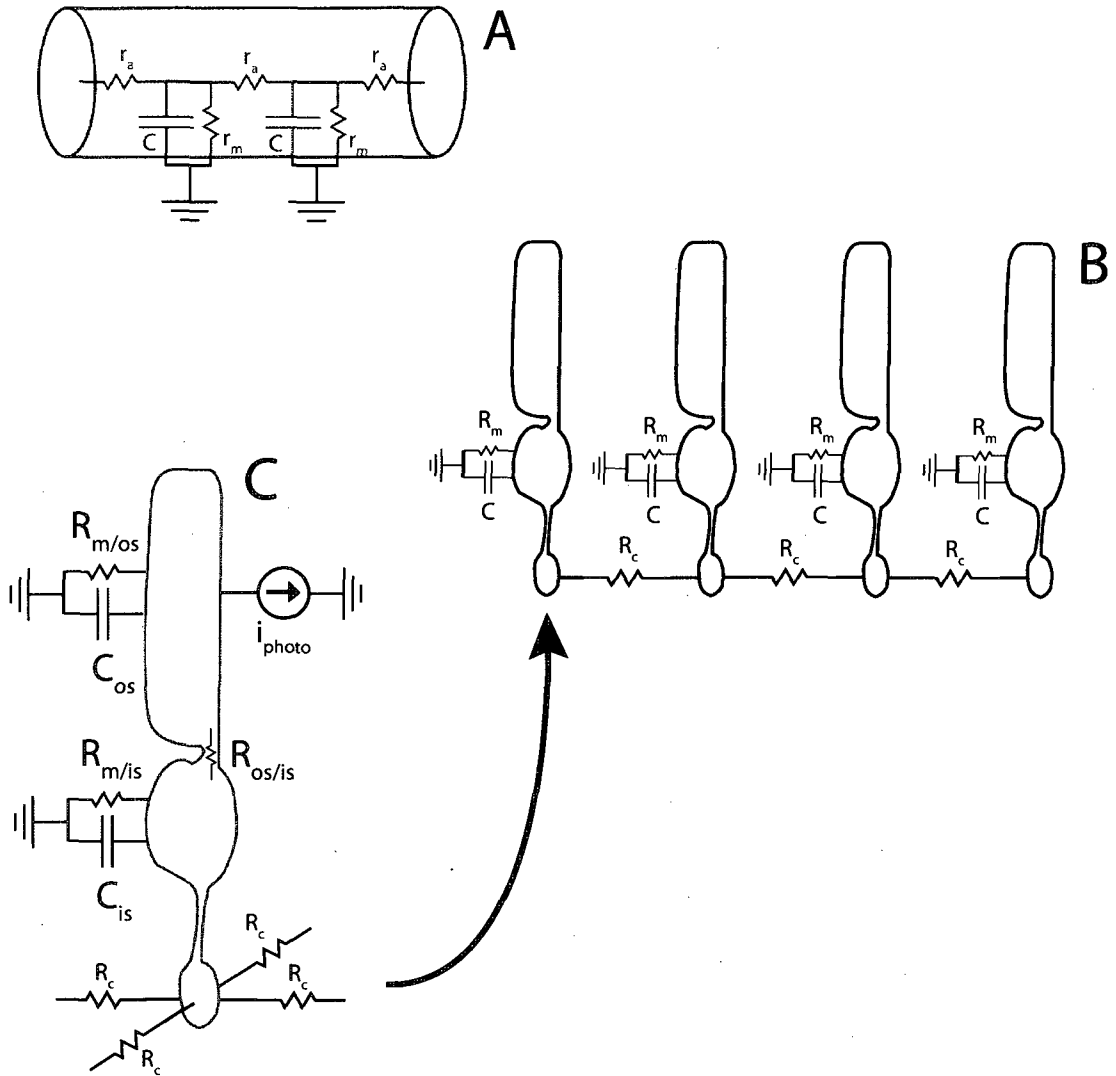


Figure 5.6: (A) One-dimensional neuronal cable. (B) One dimensional slice through the rod network is analogous to a one-dimensional cable. (C) Because the resistance  $R_{os/is}$  between the outer segment of the photoreceptor, which contains the photocurrent, and the inner segment, which has the gap junctions that couple neighboring cells, is small, the rod can be modeled as a single compartment.

and space-varying solution can be integrated over time for a step of current delivered at a point in space ( $i(x, t) = u(t)\delta(x)$ ) at  $t=\infty$  to yield the steady state solution for a point source:

$$G^*(x)_\infty = v(x) = R_{in1D}i_0 \exp\left(-\frac{D|x|}{\lambda}\right) \quad (5.4)$$

Where space constant  $\lambda$ , the dimensionless quantity of cell lengths, is given by the following:

$$\gamma = 2\left(\cosh \frac{D}{\lambda} - 1\right) \quad (5.5)$$

$$\gamma = R_c/R_m$$

When  $\lambda \gg D$  [69]:

$$\frac{\lambda}{D} = \sqrt{\gamma^{-1}} = \sqrt{R_m/R_c} \quad (5.6)$$

These general solutions  $G^*(x, t)$  and  $G^*(x)_\infty$  are known in Mathematics as Green's functions‡ for the cable equation, but they are equivalent to the engineering concept of an impulse response. The steady-state solution  $G^*(x)_\infty$  can be convolved (superimposed) with any other distribution of current  $i(x)$  to yield the steady-state solution for that distribution. Likewise, the time-dependent solution  $G^*(x, t)$  can also be convolved through space and

---

‡Green's functions are named after George Green, the who was a miller who taught himself mathematics mathematician. He studied the idea of fundamental solutions to particular partial differential equations (PDEs) in the early 19th century [72]. His work was (not surprisingly) very influential for Lord Kelvin

time with the current input to yield the solution to a space and time-dependent input. These Green's functions are identical to the concept of an impulse response from engineering.

#### 5.4.2 Cable equation in two dimensions

While the one-dimensional cable equation is useful for computing the response of the rod network to a bar stimulus, where current flow is restricted to the dimension perpendicular to the bar (see figure 5.1), to understand how coupling in the rod network reduces noise in photoreceptors, the entire network must be considered.

The cable equation has been studied extensively for one-dimensional problems relating to the voltage distribution in a neuron, but a two-dimensional electrical cable is a much less common topology. One example of a two-dimensional cable is the array of rod photoreceptors connected to one another in a grid, as shown in figures 4.3 and 5.8.

The steady-state response for a current  $i$  injected into a continuous two-dimensional cable is:

$$V(r) = i \frac{R_c}{2\pi} K_0 \left( \frac{r}{\lambda} \right) \quad (5.7)$$

$$\frac{\lambda}{D} = \sqrt{\frac{R_m}{R_c}} \quad (5.8)$$

Where  $K$  is a modified Bessel function of the second kind with  $\alpha = 0$  [69]. The solution is radially symmetric, so  $r = \sqrt{x^2 + y^2}$ .

### 5.4.3 Discrete cable

The previously presented equations describe the potential distribution in a continuous cable. However, unlike an axon, the rod network does not have continuously distributed capacitance and resistance, but consists of discrete photoreceptors interconnected via gap junctions. Each photoreceptor can be considered isopotential, with an associated membrane capacitance and resistance. The continuous cable equations give a reasonable estimate of the voltage distribution in networks of discretely coupled cells when the length constant  $\lambda$  is large compared to the distance between cells ( $\lambda > D$ ).

The analytic form of the impulse response function (Green's function) for a discrete two-dimensional cable is given by:

$$V_{m,n}(t) = \frac{1}{C} I_m \left( \frac{2t}{\gamma\tau} \right) I_m \left( \frac{2t}{\gamma\tau} \right) \exp \left( \frac{-(\gamma + 4)t}{\gamma\tau} \right) \quad (5.9)$$

$$\tau = R_m C$$

$$\gamma = R_c / R_m$$

where  $I_m$  and  $I_n$  are modified Bessel functions of the first kind. Photoreceptors are on a grid centered at  $(m=0, n=0)$ . This solution, derived by Alan Hodgkin, is given in Lamb and Simon, 1976 [69].

### 5.4.4 Numerical Methods

Although equation 5.9 can be convolved over space and time to give the response of the two-dimensional network, this is very inconvenient, and an analytic solution may not be

possible to solve for. In integrating equation 5.9 numerically as done by Lamb and Simon [69], there is error in the calculation of the Bessel functions by the computer. As a result, it is much more convenient and straightforward to solve the entire network numerically in the first place, rather than from an analytic solution.

Normally numerical solutions are used as discrete approximation to a continuous problem. They are useful in many cases where analytical solutions cannot be derived, because of either complex problem geometry or in the case of nonlinear problems. Where they exist, analytical solutions can act as a check on the accuracy of the numerical solution. To increase the accuracy of a numerical solution for a continuous problem, the discretization is made finer in space and time, requiring more computational power. However, coupled photoreceptors are discrete elements which can be considered isopotential, so a spatial finite-difference scheme is able to capture the discrete topology of the rod network exactly. Therefore a numerical finite difference integration scheme that is easy to implement with a computer is an ideal way to solve for the voltage in the rod network.

The one dimensional heat equation can be discretized as follows:

$$\frac{v_n - v_{n+1}}{R_c} + \frac{v_n - v_{n-1}}{R_c} + \frac{v_n}{R_m} + C \frac{dv_n}{dt} = i_n \quad (5.10)$$

$$\frac{2v_n - v_{n+1} - v_{n-1}}{R_c} + \frac{v_n}{R_m} + C \frac{dv_n}{dt} = i_n \quad (5.11)$$

where  $v_n$  represents the voltage at photoreceptor  $n$ , and  $i_n$  represents the current injected into photoreceptor  $n$ . This scheme can be directly realized from the circuit diagram for the rod, shown in figure 5.6. This scheme can be written in vector / matrix form, with tridiagonal

matrix  $\mathbf{A}$ . Discretizing this form in time as well yields:

$$\hat{v}_{t+1} = \hat{v}_t + \frac{1}{C} \left( \hat{i} - \frac{1}{R_c} \mathbf{A} \hat{v} - \frac{1}{R_m} \mathbf{I} \hat{v} \right) dt \quad (5.12)$$

where  $\mathbf{I}$  is the identity matrix. This integration scheme is called "forward euler", and is stable as long as  $2dt < \tau$ . It is an explicit scheme that relies on the slope of the voltage at the current time point  $t$  to predict the future voltage at  $t + 1$ . A scheme which gives better stability is:

$$\hat{v}_t = \left[ \mathbf{I} - dt \left( \frac{1}{R_c C} \mathbf{A} - \frac{1}{R_m C} \mathbf{I} \right) \right]^{-1} \left( \frac{\hat{i}}{C} dt + \hat{v}_{t-1} \right) \quad (5.13)$$

This scheme is called "backwards euler," and an "implicit" scheme in that a system of equations must be solved to find the voltage at time  $t$  from time  $t - 1$ .

This scheme can be expanded to model a two-dimensional network by changing  $\mathbf{A}$  from the tridiagonal second difference form to the difference matrix for the two dimensional laplacian operator  $\nabla^2$ . This matrix can be computed by taking the sum of the Kronecker tensor products of the identity matrix and one-dimensional second difference matrix plus the tensor product of the one-dimensional second difference matrix with the identity matrix [81].

Finally, the steady-state distribution can be solved by eliminating the capacitance from this model, where  $\mathbf{A}$  can represent the 1d or 2d difference matrix:

$$\left( \frac{1}{R_m} \mathbf{I} + \frac{1}{R_c} \mathbf{A} \right) \hat{v}_{ss} = \hat{i} \quad (5.14)$$

### 5.4.5 Network input impedance

#### 2D input impedance

The input impedance measured from a point in the two-dimensional network  $R_{in2D}$  is given by the steady-state voltage response of a cell divided by the value of the current step injected into it. Solving the discretized equation 5.14 numerically for the voltage response of a unit point source of current injected into that cell gives the input resistance  $v_{0,0} = R_{in2D}$ .

The analytical form is [69]:

$$R_{in2D} = v_{0,0} = R_m \frac{2}{\pi} \left( \frac{\gamma}{\gamma + 4} \right) D \left( \left[ \frac{4}{\gamma + 4} \right]^2 \right) \quad (5.15)$$

where D is the elliptic integral of the first kind [69]. For this work, the numerical solution for  $v_{ss}$  was used to calculate the input impedance.

#### 1D input impedance

The one-dimensional input impedance is given by:

$$R_{in1D} = v_0 = \frac{DR_m}{2\lambda_{1D}} \S \quad (5.16)$$

It is important to note that the one-dimensional input impedance  $R_{in1D}$  is different from the two-dimensional input impedance  $R_{in2D}$ . The one-dimensional impedance is not as useful for a two-dimensional network because it would be very hard to measure experimentally. It would be the input impedance to a current injection into a column of photoreceptors

---

§We derive this relationship in appendix A.5

in the network. This could be assessed with the bar light stimulus by dividing the voltage response by the equivalent photocurrent generated, but would require making several assumptions.

A plot of the network impedance vs  $\gamma = R_c/R_m$  for a 1D and 2D network is shown in figure 5.7 B. As the  $R_c/R_m$  grows, the network becomes essentially uncoupled, and the input impedance approaches  $R_m$ . The impedance in the one-dimensional network is greater because there are fewer paths for the current to take.

Figure 5.7 A shows the normalized length constant  $D/\lambda$  as a function of  $R_c/R_m$ . The length constant decreases as  $R_c/R_m$  increases because it becomes increasingly difficult for current to flow laterally. For the 1D steady-state solution, the length constant describes an exponential decay as in equation 5.4. Although the 2D steady-state solution (equation 5.7 involves a Bessel function, the discrete solution is well approximated by an exponential decay with length constant  $\lambda_{2D}$ , shown in figure 5.5. Figure 5.4 C shows the relationship between length constant and cell input impedance. This is a useful relationship because the length constant can be measured experimentally, whereas  $\gamma$  cannot.

#### 5.4.6 Network impulse response and frequency response

Figure 5.8 B shows the impulse response (Green's function) for a 2D network with  $R_m = 0.7 \text{ G}\Omega$ ,  $R_c = 0.9 \text{ G}\Omega$ , and  $C = 50 \cdot 10^{-3} \text{ nF}$ . The corresponding frequency responses of the indicated cells are shown in figure 5.8 C. The cutoff frequency in the originating rod (0,0) is around 1 Hz. The cutoff frequency in more distant rods decreases further from the



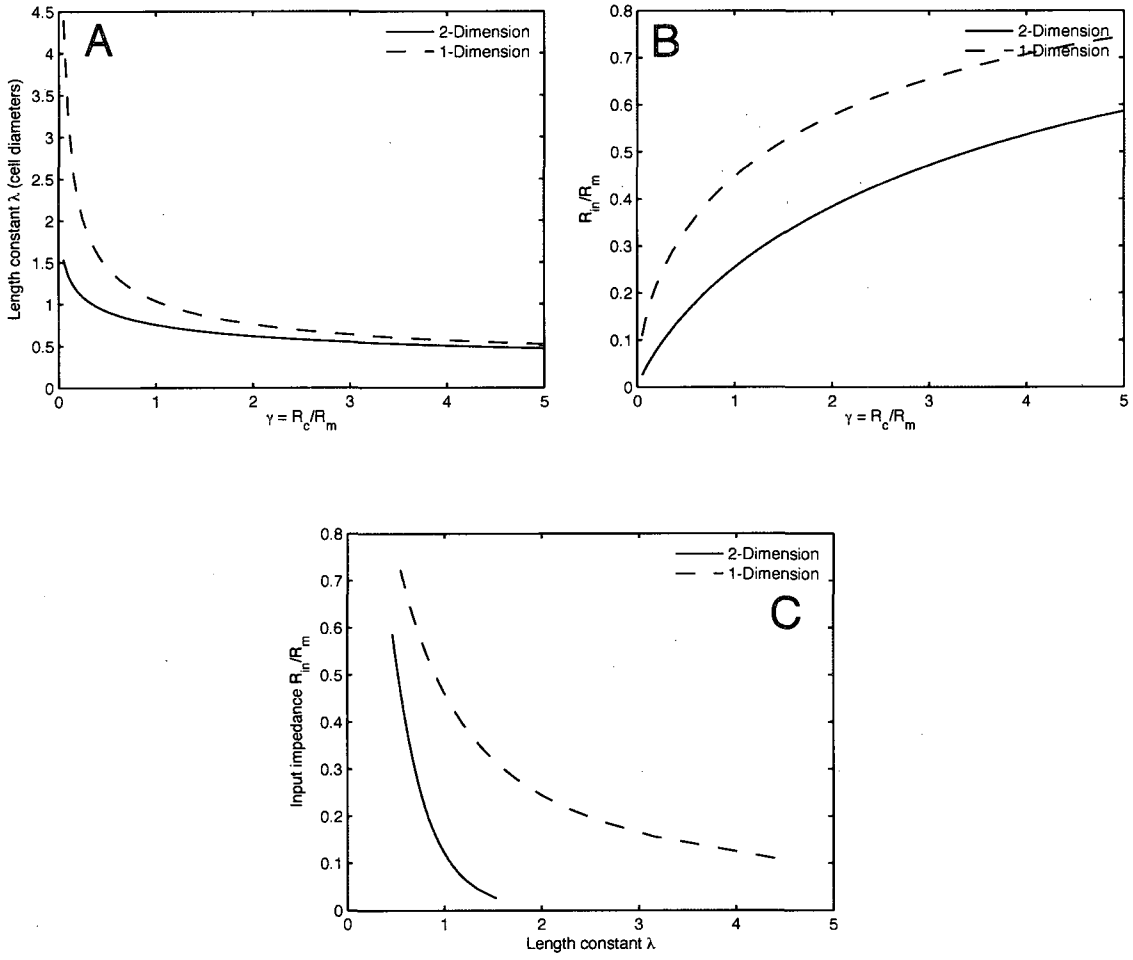


Figure 5.7 : These plots show the key parameters for describing the steady-state voltage distribution in a 1D and 2D cable. The results are for a point source, as  $\gamma = R_c/R_m$  is varied. (A) Normalized length constant  $D/\lambda$  plotted vs  $\gamma = R_c/R_m$ . (B) Input impedance  $R_{in}$  relative to membrane resistance  $R_m$  as a function of  $\gamma = R_c/R_m$ . (C) Input impedance  $R_{in}/R_m$  vs normalized length constant  $D/\lambda$  for the 1D and 2D case.

originating rod. The frequency response plot (figure 5.8) shows that signals changing slower than  $\approx 1$  Hz can be considered to be unaffected by the capacitive filtering.

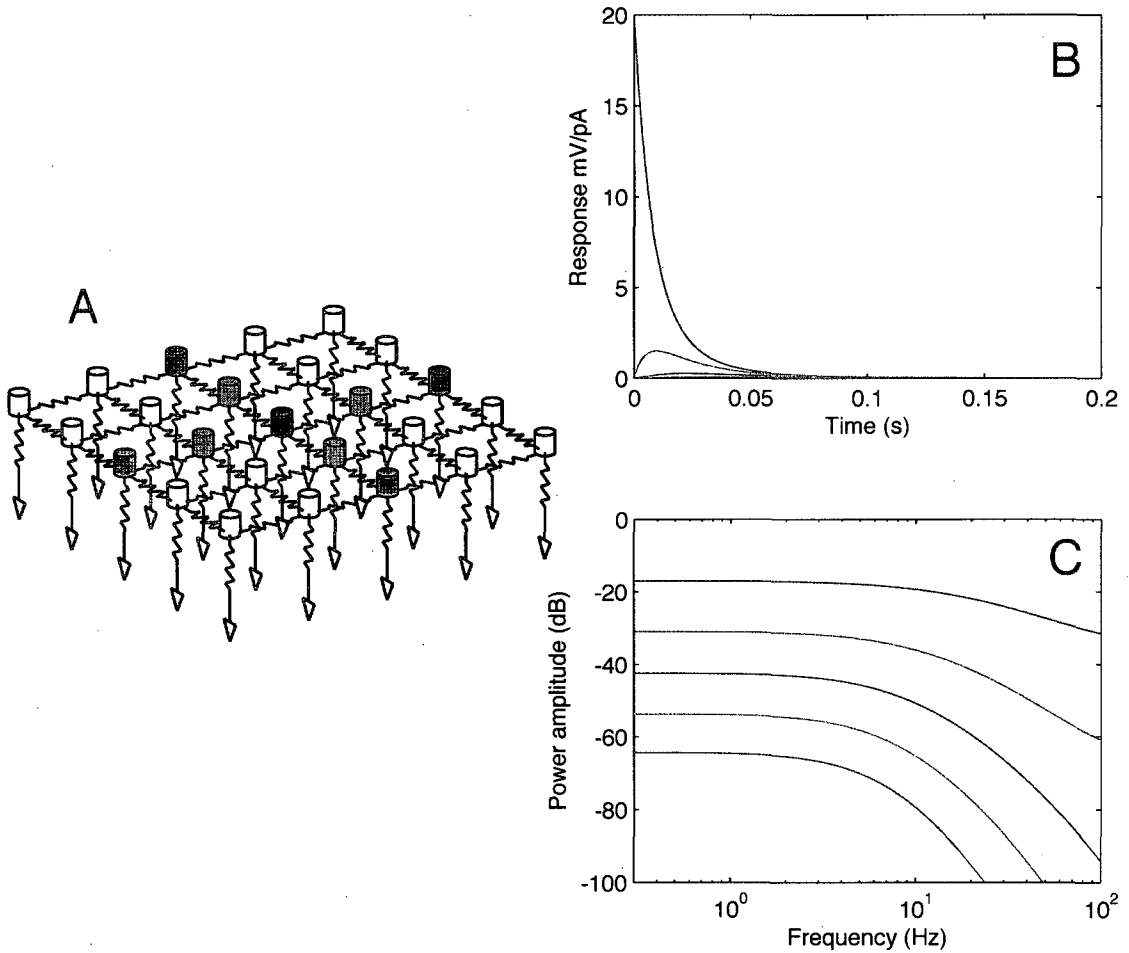


Figure 5.8 : (A) Diagram of the network with colored cells and their corresponding traces in A and B. (B) Impulse response and Bode plot of corresponding (C) frequency response of colored cells in response to a signal in the center (blue) cell in power  $\text{dB} = 10 \log (\text{mV/pA})^2$ .

## 5.5 Estimation of adjacent coupling resistance

The measurements made using voltage clamp in section 5.3 measure the apparent resistance  $R_a$  between two cells through the entire network, not the resistance  $R_c$  that connects the two adjacent cells. When the length constant is short, these values are comparable. The network resistance between two cells is an interesting parameter because it can be measured directly from the retina, and estimates the degree of coupling between cells. It also serves as a lower bound on the possible value for  $R_c$ . However, by itself,  $R_a$  is useless to create a model because many combinations of  $\gamma = R_c/R_m$  could produce a recorded network conductance. Here, we show that for a given input impedance and length constant, there is one network resistance for adjacent cells.

Input impedances may vary from cell to cell, so to obtain an estimate of  $R_c$  from  $R_a$ , the input impedance of the particular cell being recorded is important. While the input impedance of each cell was not recorded during the voltage clamp experiments, it can be estimated by making two assumptions. If we assume (1) that the input impedances of the pair of cells being recorded are equivalent, and (2) that the holding potential of the follower cell (-40 mV) is near the resting potential for rods, then we can solve for the input impedance of each cell  $R_{in2D}$ .

The voltage distribution can be described by a system of two equations from the superposition of two point sources of current in the network, as shown by figure 5.5. These equations are as follows, where  $K$  is the voltage decay from the source to the neighboring cell.  $v_0$  is the voltage (and  $i_0$  the current) in the driver cell, and  $v_1$  is the voltage (and  $i_0$  the

current) in the follower cell.

$$\begin{cases} v_0 = R_{in2D}i_0 + R_{in2D}i_1K \\ v_1 = R_{in2D}i_0K + R_{in2D}i_1 \end{cases} \quad (5.17)$$

From the second relationship, if  $v_1$  is assumed to be 0 because the follower cell is held at the rod resting potential then:

$$\begin{aligned} R_{in2D}i_1 &= -R_{in2D}i_0K \\ K &= -\frac{i_1}{i_0} \end{aligned}$$

Divide the first relationship in system 5.17 by  $i_1$  and substitute in K

$$\frac{v_0}{i_1} = R_{in2D}\frac{i_0}{i_1} - R_{in2D}\frac{i_1}{i_0} \quad (5.18)$$

from our definition of network resistance between adjacent cells (R apparent)  $R_a = v_0/i_1$

$$R_{in2D} = \frac{\frac{v_0}{i_1}}{\left(\frac{i_0}{i_1} - \frac{i_1}{i_0}\right)} = \frac{R_a}{\left(\frac{i_0}{i_1} - \frac{i_1}{i_0}\right)} \quad (5.19)$$

The input impedance for all pairs estimated from equation 5.19 is shown in figure 5.7. The mean  $R_{in2D}$  was 137 M $\Omega$ , which is in line with our experience from recording from rod photoreceptors. Figure 5.9 A shows the estimates of  $R_{in2D}$  for each pair of cells, and figure 5.9 B shows a box plot with the means, 25th and 75th percentiles of the same data.

From the previous set of equations we can also solve for how  $R_a$  varies with  $R_{in2D}$  and  $\lambda_{2D}$ . Substituting K back into equation 5.18 yields

$$\frac{v_0}{i_1} = R_a = -R_{in}/K + R_{in}K$$

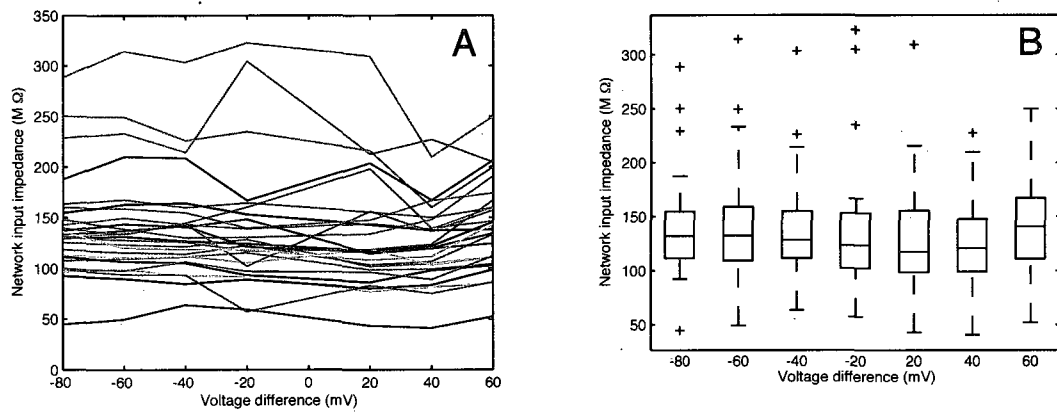


Figure 5.9 : (A) Estimates of input impedance  $R_{in2D}$  from dual patch voltage clamp data. (B) Boxplot of data showing mean (red line), 25 and 75th percentiles (blue), and outliers (red crosses). Estimates of  $R_{in2D}$  come from the analysis detailed in section 5.5.

Although the steady-state voltage distribution for a continuous network is given by a Bessel function (equation 5.7), the voltage falloff is well approximated by an exponential decay, as shown in figure 5.5 D. Therefore,  $K$ , the voltage difference between neighboring cells due to a point source of current can be given by a unit of single exponential decay.

$$K = -\frac{i_1}{i_0} = -\exp\left(-\frac{D}{\lambda}\right)$$

$$\frac{v_0}{i_1} = R_a = R_{in} \exp\left(-\frac{D}{\lambda}\right) - R_{in} \exp\left(\frac{D}{\lambda}\right)$$

$$\frac{v_0}{i_1} = R_a = R_{in} \left[ \exp\left(-\frac{D}{\lambda}\right) - \exp\left(\frac{D}{\lambda}\right) \right]$$

From the definition for hyperbolic sine:

$$\frac{v_0}{i_1} = R_a = -2R_{in} \sinh\left(\frac{D}{\lambda}\right) \quad (5.20)$$

## 5.6 Coupling and noise in the rod network

Estimates of  $R_m$  and  $R_c$  are particularly interesting because they describe how rod-rod coupling affects visual signals in the retina. With these estimates from derivations and experiments described in the previous sections, we show that compared to an uncoupled rod network, rod-rod coupling increases the signal-to-noise ratio of visual information when image features cover multiple photoreceptors, but reduces it when the input signal contrast varies from rod to rod.

We analyzed this phenomenon quantitatively using Fourier analysis. Although the steady-state impulse response contains all of the information about how signals may spread in the

rod network, its message is not easy to interpret. Spectral analysis via the Fourier transform of these steady-state responses, on the other hand, reveals rod-rod coupling's effect on image frequency components. Because the frequency components of images may change over the area covered by a single rod, the width of each rod and spacing between rods is also taken into account. Rods are assumed to be spaced 16 microns apart with a diameter of 10 microns.

Figure 5.10 A shows the contributions of a single rod to the response of the entire network with a 1 pA step test current. The response peaks at 0.141 mV ( $R_{in2D} = 141 \text{ M}\Omega$ ) at the center rod, and coupling between rods allows signal spread to adjacent rods. Figure 5.10 B shows the response when the same rods are uncoupled. The response is 0.3 mV ( $R_m = 300 \text{ M}\Omega$ ). Because any arbitrary image can be decomposed into its frequency components, examining the frequency response of both the coupled and uncoupled network can demonstrate their behavior. Figure 5.10 C and D show example 2D and 1D sinusoidal gratings with frequencies of 50 microns per cycle.

Figure 5.11 shows the voltage response of a rod to varying frequencies in the x and y dimension from the 2D Fourier transform of the patterns in figure 5.10. The amplitude of the sinusoidal stimulus on the retina is a single rod's response to a given frequency when the peak over the rod's center. Figure 5.11 A shows the response in the coupled network, from 5.10 A, and 5.11 B shows the response in an uncoupled network. The diagonal represents stimuli of increasing frequency with x and y frequencies equal, as shown in figure 5.10 C. The uncoupled network has a frequency response (figure 5.11 B) with radial symmetry

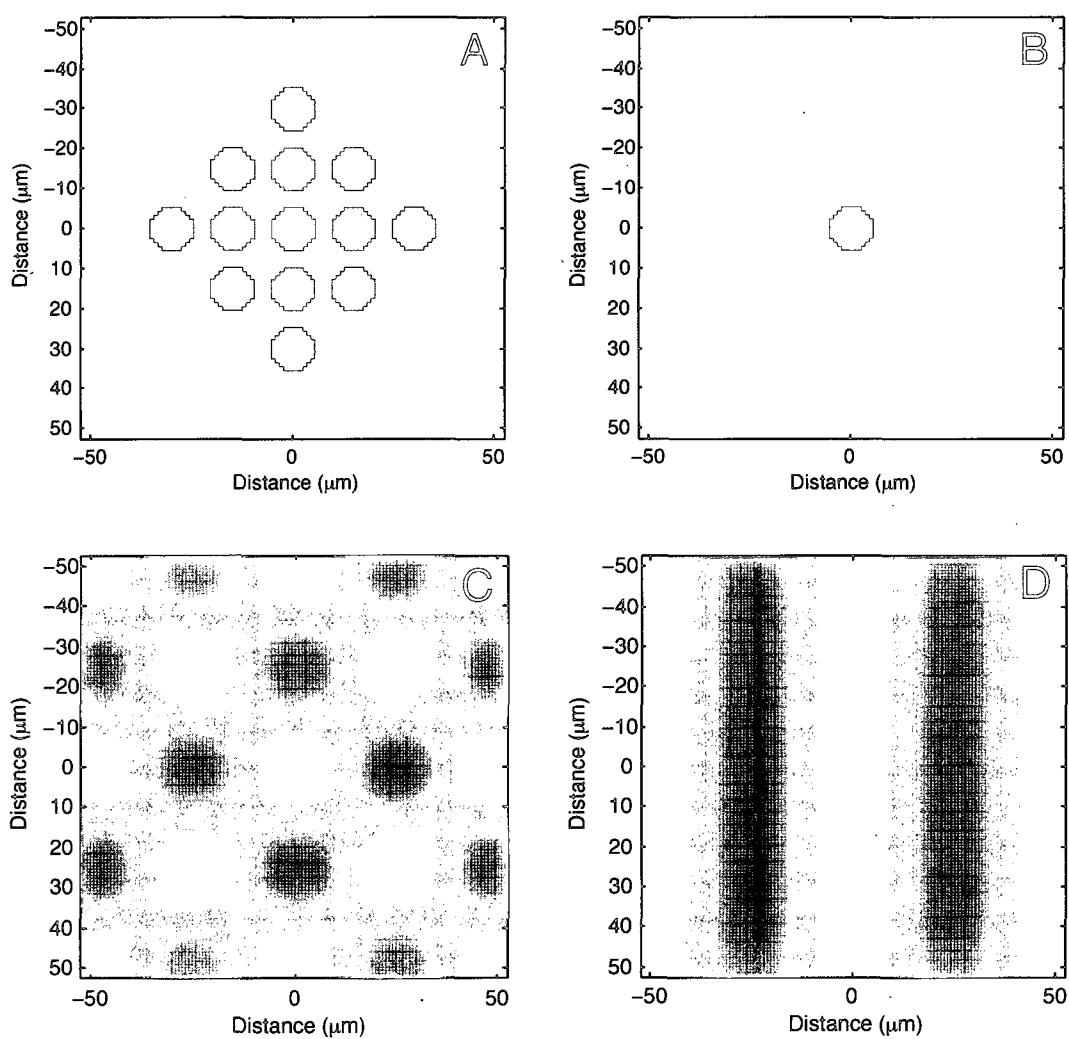


Figure 5.10 : (A, B) Rod network with rod diameter  $a = 10 \mu\text{m}$  and rod spacing  $D = 16 \mu\text{m}$ . (A) Rod network with coupling. Colors represent relative response amplitudes from exponential decay. (B) Uncoupled rod network. (C) Example of a two-dimensional sinusoidal grating. (D) Example of a one-dimensional grating.



because it reflects the geometry of the photoreceptor, which is circular. Irregularities in the frequency response come from the imperfect roundness of the digital representation of each receptor (figure 5.10 A, B). As expected, both the uncoupled and coupled networks show an identical response to whole field stimuli ( $f_x = f_y = 0$ ), because whole field stimuli "uncouple" the network. The coupled network does not show radial symmetry. This is due to the fact that the length constant for signal spread is different for one dimensional  $\lambda_{1D}$  and two dimensional stimuli  $\lambda_{2D}$ . Therefore the frequency response to a 1D grating ( $f_x$  or  $f_y = 0$ ), shown in figure 5.10 D, is different from a two dimensional grating of the same frequency ( $f_x = f_y$ ).

Figure 5.11 shows that the coupled network has a faster falloff in its response to spatial frequencies than the uncoupled network. However, only a small part of the plots in figure 5.11 is actually relevant. Because photoreceptor spacing is 16 microns, according to the Nyquist sampling rule, any spatial wavelengths shorter than 32 microns will not be able to be represented by the retina. This corresponds to a frequency of 0.03 cycles per micron (or a wavelength of 32 microns), or 0.5 cycles per rod. Any frequencies higher than 0.03 cycles per micron will be aliased by the photoreceptors—perceived as frequencies lower than the stimulus. Figure 5.12 A shows an example of aliasing occurs in the coupled and uncoupled network. Note that both networks in 5.12 A have adjacent photoreceptors that are not shown.

Noise due to sources internal to the rod is another sort of stimulus the network must contend with. In the case of the uncoupled network, internal noise currents lead directly

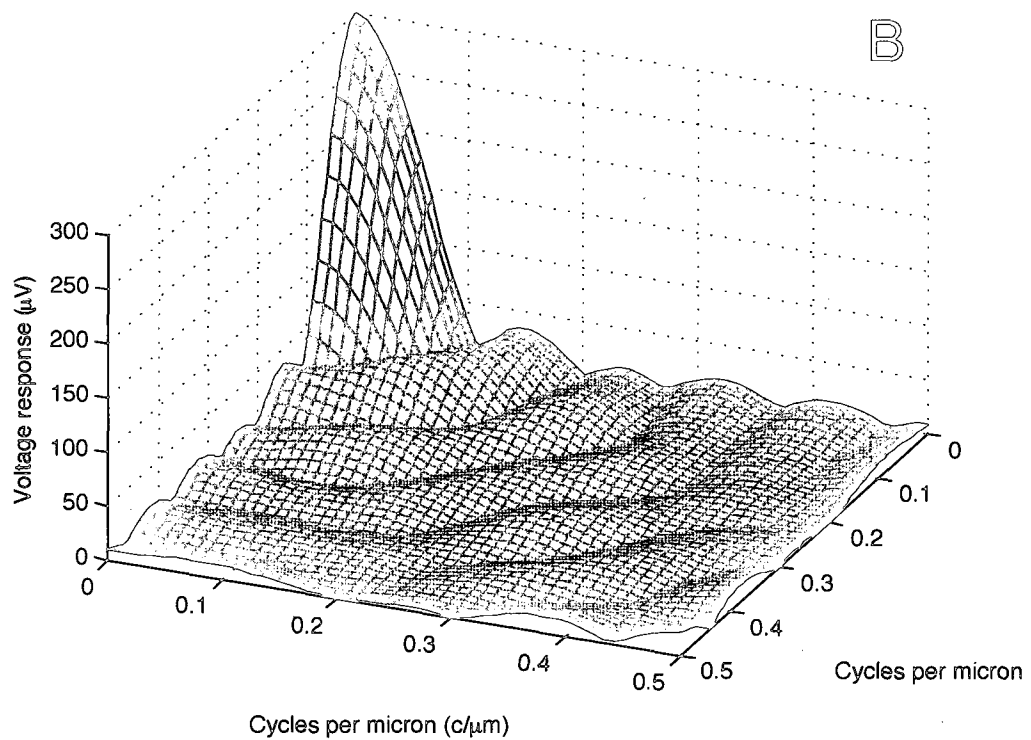
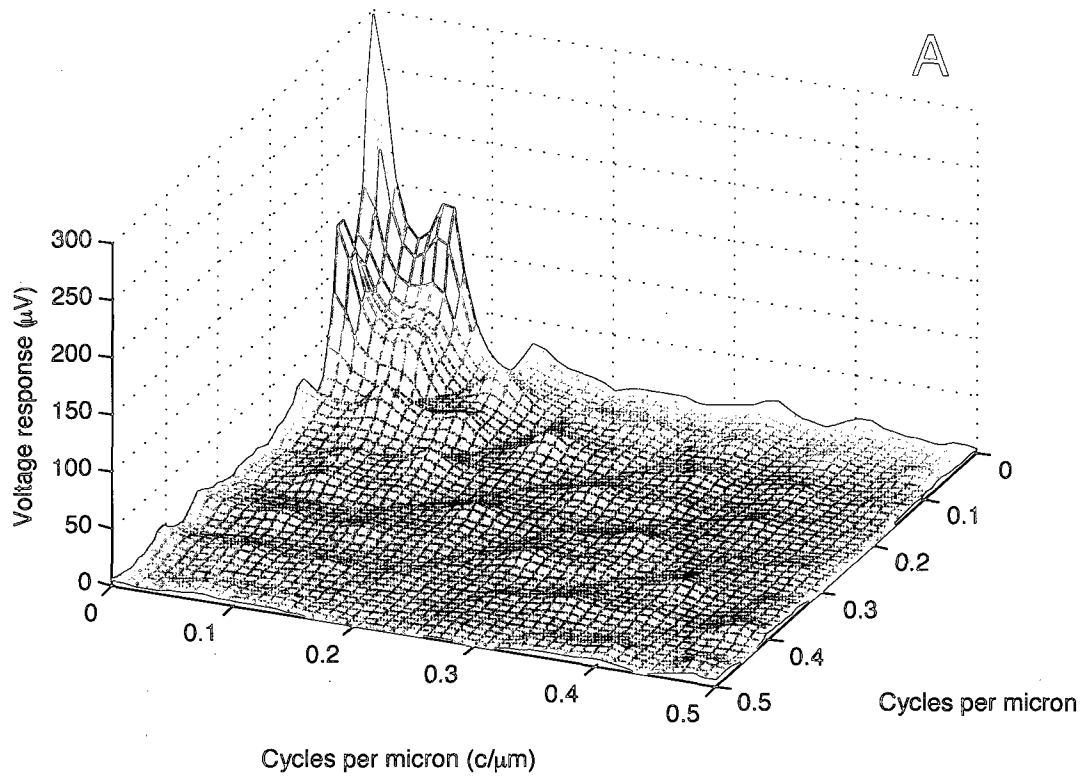


Figure 5.11 : Response of the rod network to spatial frequencies in two directions. Rod diameter  $a = 10 \mu\text{m}$  and cell spacing  $D = 16 \mu\text{m}$ . Diagonal represents equal  $x$  and  $y$  frequencies. (A) Spatial frequency response in the coupled salamander retina. (B) Spatial frequency response in uncoupled rod photoreceptors.

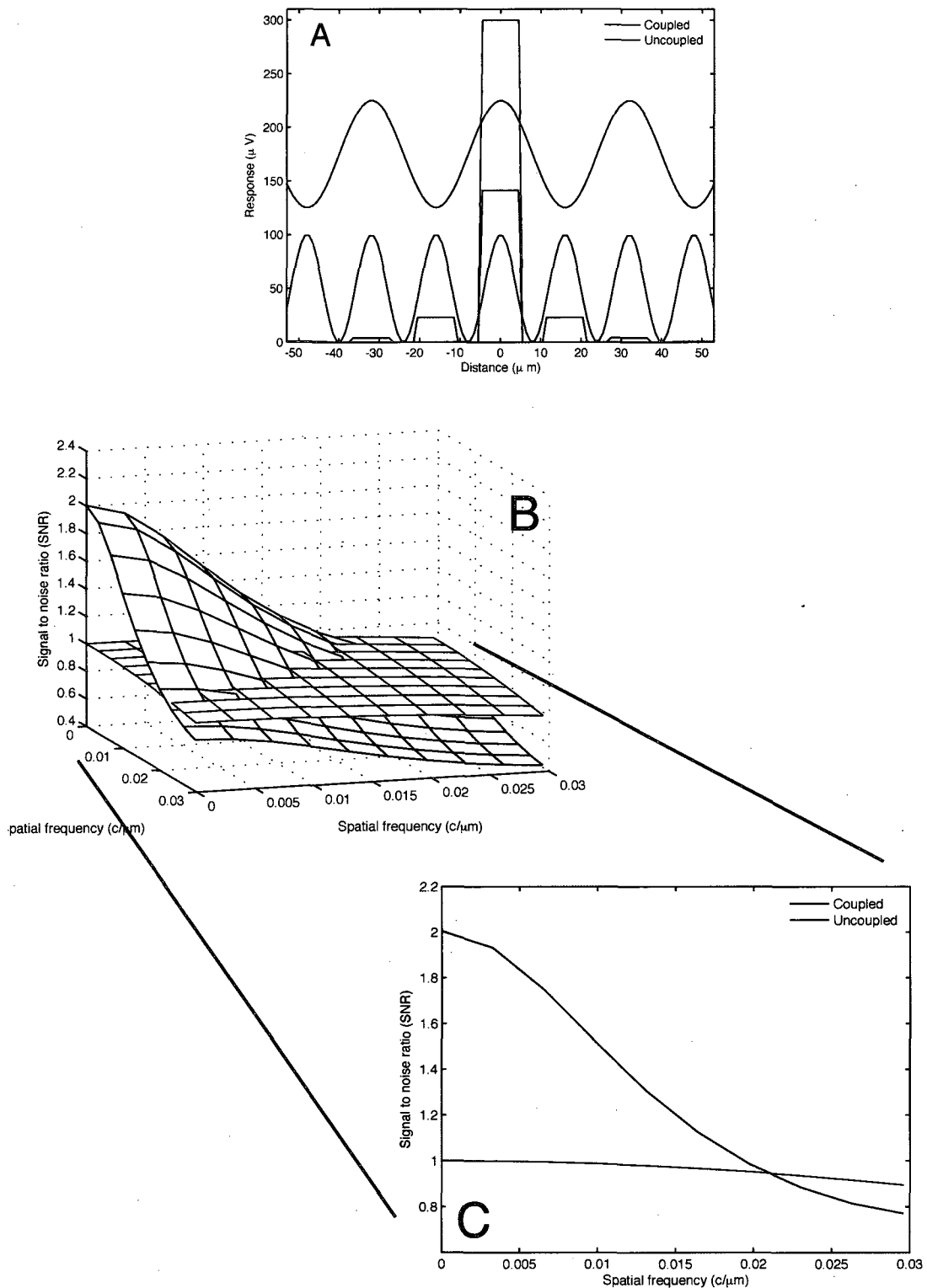


Figure 5.12 : (A) Example of aliasing in the rod network. The first sinusoid is at the critical frequency ( $0.5 \text{ c/rod}$   $0.03 \text{ c/micron}$ ). The second sinusoid is aliased by the rods, causing the second peak in the rod responses shown in figure 5.11. (B) Signal-to-noise ratio with unit sinusoidal input and unit noise variance in each rod vs two-dimensional frequency components. (C) A projection along the x axis of the plot in B.

to voltage noise in the photoreceptor through the membrane resistance. The output voltage variance is given by:

$$v_{uc}^2 = R_m^2 i_0^2 \quad (5.21)$$

In the coupled rod network, current fluctuations in a rod are distributed through the network according to the impulse response.

$$v_c^2 = \sum_{m=-\infty}^{\infty} \sum_{n=-\infty}^{\infty} v_{m,n}^2 \quad (5.22)$$

where  $v_{m,n}$  is the steady-state impulse response function of the rod network (as in figure 5.5).

For a hypothetical current noise of unit variance, the output variances and standard deviations for the uncoupled and coupled cases are:

$$v_{uc}^2 = R_m^2 = 0.09$$

$$v_{uc} = R_m = 0.3$$

$$v_c^2 = 0.02$$

$$v_c = 0.15$$

Because of the signal averaging due to coupling, the baseline noise of the coupled network is half the noise of the hypothetical uncoupled network. The signal-to-noise ratio is the output amplitude divided by the noise standard deviation, so with whole field stimuli, the

SNR in the coupled network is double that of the uncoupled network. Figure 5.12 B shows the SNR for an intrinsic noise source of unit variance in each rod over all practical combinations of spatial frequencies. Frequencies higher than the Nyquist sampling frequency for individual rods are omitted. Figure 5.12 C shows a 2D projection of B, demonstrating that for most frequencies able to be realized in the network, the coupled network shows an increase in SNR.

## 5.7 Discussion

While it is known that rods are coupled in the salamander retina, the nature of the coupling has been unclear due to conflicting reports of the coupling resistance. In this work we have used two techniques, light stimuli, and electrical stimuli, to estimate the coupling resistance between rods in the salamander retina.

### 5.7.1 Measurement of coupling with light

Other studies of electrical coupling between cones in the turtle retina used a similar technique, with a manually driven bar [69]. As mentioned by Detwiler and Hodgkin [32], a problem with using a light stimulus to probe coupling is that the light stimulus is scattered both by retinal tissue and the optics of the experimental setup. This scattering could lead to an overestimate of the length constant  $\lambda_{1D}$ , as it makes the stimulus appear wider to the photoreceptors than it actually is. To circumvent this confounding factor, we measured the profile of the scattered light in the retinal preparation using a cone photoreceptor as a detec-

tor. Because cones are not coupled to one another, the recorded response comes only from that cone. We compensated for the nonlinear response of the cone by using its nonlinear sensitivity relationship (figure 5.2 B) to find the intensity of the scattered light from the bar as a function of position. We then transformed the profile of the scattered light to predict the hypothetical uncoupled rod response, and deconvolved the actual measured response from the rod network with this hypothetical uncoupled response. The resulting predicted network response gave estimates of  $\lambda_{1D} = 17.4$  and  $9.8 \mu\text{m}$ . The latter estimate gave a far better fit to the expected exponential decay.

One drawback of this measurement technique is that while cones are not coupled to cones, they are weakly coupled to adjacent rods. However, our experiments used a light stimulus with a background intensity that nearly saturated the rod response while probing the cone response. The very minimal rod responses would be further attenuated by the strong resistance (weak coupling) between rods and cones [7]. Another potential drawback of this method is that negative feedback from horizontal cells to cones could lead to an underestimate of the light response profile. However, our experience from other experiments is that thin bar stimuli such as the one we used to not stimulate enough of the horizontal cell receptive field to elicit any feedback.

### 5.7.2 Measurement of coupling via dual-patch

Our dual-patch recordings are the first known set of paired patch-pipette recordings from adjacent rods in the whole salamander retina. Other studies have used patch pipettes in

the slice preparation (Zhang and Wu) [115], and sharp electrodes in the slice preparation (Attwell and Wilson) [5]. Compared with Zhang and Wu, our whole-mount estimate of  $R_a$  is less than half the  $R_a$  measured in the slice preparation (0.89 G $\Omega$  vs 2 G $\Omega$ ). In making the slice preparation, one half of the surrounding network is sheared away. Because our results show that only a small part of the current flow between the two rods is through indirect pathways, we would not expect to see a very large difference. However, the 2 G $\Omega$  estimate is still larger than our estimate of  $R_c$ , which suggests that in making the slice preparation, some of the gap junctional connections between the adjacent cells could have been sheared away.

In comparison to Attwell and Wilson's estimate of 0.3 G $\Omega$  [5], our estimate is notably larger. They report a lower network input impedance  $R_{in}$  of 90 M $\Omega$  compared to our 137 M $\Omega$  estimate, which could be due to cell damage from the sharp electrodes they used. This underestimate of  $R_{in}$  could have led them in turn to underestimate the coupling resistance  $R_c$ , because it is a determinant of the input impedance (equation 5.15).

While our experiments represent the most rigorous estimates to date of the apparent coupling resistance  $R_a$  in the salamander retina, they are also not without drawbacks. In order to accurately estimate  $R_c$  from  $R_a$ , we had to calculate the input impedance of each cell using recordings we made of the pair. Due to inhomogeneities in the network, the impedances of the driver and follower cell could be different. However, this difference would be expected to be averaged out over the many pairs we recorded. Second, the estimate of the length constant  $\lambda_{2D}$  from the data relies on the assumption that the follower cell was patched

at the resting potential for unstimulated rods. This potential could change from cell to cell, and the -40 mV we assumed is likely up to 5 mV more negative than the average rod resting potential in darkness. This could cause a small error, but the estimates of  $\gamma = R_c/R_m$  with the dual patch recordings agree well with our estimates using the light stimulus.

### 5.7.3 Significance of rod-rod coupling

It is well known that rods are coupled to one another in several species, but the consequences of the coupling have not been thoroughly examined quantitatively. We use the coupling data collected in the first sections to create a first-order 2D model of the rod network (figure 5.6). We analyze the model response using spectral analysis to show how the spatial frequency components of visual scenes will be represented in the salamander retina (figure 5.11). This analysis shows that coupling reduces high frequency components. Features with a wavelength of  $\approx 50$  microns would be attenuated to half the amplitude of a whole-field stimulus. This coupling would reduce the response to sharp contrasts in a visual scene, which are composed of high frequency changes.

While rod-rod coupling has the disadvantage that it causes attenuation of rapid changes in contrast in an image, its primary advantage of reducing noise in photoreceptors is a worthwhile tradeoff. One of the sources of intrinsic noise in photoreceptors is the photocurrent, which drives the photoreceptor response to light. The photocurrent noise has two components: continuous noise, which comes from variations in phosphodiesterase (PDE) activity, and discrete noise, which comes from spontaneous thermal activation of rhodopsin



molecules [90]. Both of these phenomenon have temporal spectra that are largely confined to frequencies below 1 Hz [105, 62], so according to the model frequency response (figure 5.8), the retina's affect on these noise sources will be described by the steady-state response.

Our analysis shows that the standard deviation of the noise in the coupled salamander retina is halved compared to a hypothetical isolated rod. This means that the signal-to-noise ratio for whole-field stimuli is double what it would be in a rod network without coupling. The decay in the coupled retina's response to increasing spatial frequencies means that at a feature wavelength of 50 microns, the SNR is equal to that of the uncoupled retina. However, the minimum perceptible wavelength before image aliasing occurs is twice the receptor spacing, or 32 microns (figure 5.12 A). So for most perceptible spatial frequencies, coupling between rods leads to an increase in the signal-to-noise over the uncoupled network (figure 5.12 B, C), and for higher frequencies, the SNR is at least 80% of the uncoupled network.

Rod bipolar cells are thought to have synaptic inputs from several rods, as their dendritic field diameter is  $\approx 60$  microns [109]. While their receptive fields are larger [113], this is thought to be due to coupling between bipolar cells, as this is too far to have occurred from rod-rod coupling. This means that, uncoupled, each bipolar cell may average the responses of 12-13 rods. The averaging of rod responses by bipolar cells would reduce both the quantal noise from the synapse and intrinsic noise from photoreceptors. This would seem to make the averaging of rod signals via rod-rod coupling redundant— if the synapse was linear. However, current evidence shows that the rod bipolar cell synapse is not linear¶ [111]. The

---

¶It has been shown that the rod-DBC synapse can be approximated as linear for a given light intensity [110]

saturation gain function at the synapse means that the bipolar cell output would be much noisier for small signals due to the increased gain for these signals. Therefore, by filtering signals in the rod network before they go through the synapse, the noise in the signals could be reduced before they are amplified by the synapse.

Natural scenes tend to exhibit  $1/f$  spectra or  $1/f^2$  power spectra [105, 11], which means that the majority of the signal in natural images is contained low spatial frequency components. These low spatial frequencies would be reproduced with better fidelity in a retina with coupling than one without it. Although it can be argued, at least for higher animals such as primates, that most of the information in visual scenes comes from higher frequency image components, such as fine high contrast features like text and other symbols, the rod pathways are adapted to a different purpose. Instead, the rod pathway has evolved to operate in dimly-lit low contrast environments, characteristic of natural environments in twilight and in starlight.

Interestingly, Balboa and Grzywacz show that the power spectra of underwater images exhibit anisotropy— they are different when measured in the horizontal vs vertical direction. Salamanders spend the larval stage of their life in an aquatic environment, so it is possible that their rod networks could have evolved to have their anisotropic coupling in order to adapt to the spatial frequencies in their environment. Our results demonstrate significant (Fisher F-test) variability in coupling conductances between different rod pairs, which could have resulted from differing coupling conductances in the horizontal vs vertical direction. Future work may evaluate whether such a difference does exist. If so, it would support our

claim that coupling in the salamander rod network is optimized to maximize the fidelity of visual scenes from its environment.

## Chapter 6

### Conclusion and Future Directions

#### 6.1 Conclusion

In the 40 year history of electrophysiological investigations into the retina, much has been learned about photoreceptor physiology. For example, it is likely that we have a more detailed understanding of the complex molecular pathway underlying the photocurrent than any other molecular transduction pathway. The tools available to study retinal electrophysiology today are fundamentally the same as the tools that were available since the invention of the patch clamp technique 30 years ago. The biggest change from then to today has been in our accumulation of knowledge about how the retina works, and the addition of faster, and cheaper computers for easier data analysis. In particular, having enough digital storage capacity to make all of the data points an experimenter has collected online available for online analysis is very convenient. As a result, the studies of photoreceptor electrophysiology in this thesis use the currently available tools to build on what is already known about photoreceptor function.

While studies of  $I_h$  had already been done in rod and cone photoreceptors, our work analyzed their properties in a controlled way to show that these currents are similar in salamander rods and cones. Combining these patch clamp results with western blot and im-

munohistochemical analysis, we demonstrated for the first time that the HCN1 isoform is likely the ion channel that underlies  $I_h$  in both rods and cones. We also performed the technically challenging experiment of estimating the small single channel conductance of HCN1 channels in photoreceptors (section 3.2.3), and show that it is similar to the conductance of HCN1 channels in other systems— around 660 fS. These studies, along with molecular and genetic evidence from amphibians (section 3.2.2) suggest that HCN channels are, like the voltage-gated sodium channel, a highly conserved building block in physiology. Our studies on the function of HCN channels in photoreceptors (section 3.3) show how they act to speed up the light response of rod and cone photoreceptors at the expense of decreased gain at low temporal frequencies. They demonstrate that HCN channels are more important for rod function at dimmer light intensities, and more important in cones at brighter light intensities.

Next, we combined the information learned about HCN channels with parameters from other photoreceptor ion channels to form functional physiology-based models of rod and cone photoreceptors. Based on the results of the rod model, we demonstrate that the time dependent changes in  $h$  and  $K_x$  conductance largely cancel one another (section 4.1.2). As a result, change in rod membrane impedance during a light response is minimized, while simultaneously preserving the high-pass filter characteristic important for the rod temporal response. We propose that the stable membrane impedance may be beneficial for signal averaging through rod-rod coupling by minimizing distortion in lateral signal propagation from rod-rod coupling.

With the cone model, we investigate a potential component of horizontal cell to cone feedback that is common to both the pH and hemichannel theories of feedback. We conclude that this mechanism, which involves activation of voltage gated calcium channels and gating of a calcium activated chloride current, is feasible (section 4.2.1). This analysis also suggests that modulation of the calcium current alone is not enough to cause the observed depolarization during a horizontal cell surround response, highlighting the potential role for the calcium activated chloride current in the feedback response.

Finally, in chapter 5, we perform a detailed analysis of rod-rod coupling using light and electrical stimuli, and use the resulting parameters in a linear model of the rod network. With the model, we demonstrate quantitatively how rod-rod coupling leads to an attenuation of high spatial frequencies in visual scenes, but also a large reduction in photoreceptor noise. By analyzing the tradeoff between these two features, we show that coupling provides a benefit in signal-to-noise ratio for most perceptible stimuli. This benefit is especially helpful in the representation of natural scenes, a task for which the rod system has presumably evolved to handle.

I hope that these studies will provide a base for further studies of the retina by others in the field of retinal physiology. In particular, the analysis in chapter 5 is not necessarily specific to rods, and could be generalized to other coupled neurons in the retina.

## 6.2 Future Directions

After talking with and reading about many scientists, I realize that every paper published is never really finished— there are always more experiments to be done, more in depth analyses to be undertaken, and more to be discovered. If I were to say that I am truly done with the work in my thesis, I think it would mean I would be ready to retire, not graduate. That being said, the work in this thesis is able to stand on its own, and should be a useful and interesting contribution to visual neuroscience. However, even as I write this I have ideas about how to extend the work I presented in chapter 5.

While the steady-state analysis of photocurrent generated noise in section 5.6 is valid for the photocurrent, whose frequency components are below the filter cutoff several photoreceptors distant from the source, it is not true of other noise sources in the rod. For instance, HCN channels, which have a time constant around 60 ms, would fluctuate with a cutoff frequency of 2.6 Hz, above the cutoff frequency for any rod in the network (figure 5.8). Other ion channels such as voltage gated potassium channels, with even faster kinetics may also contribute to receptor noise. Accurately characterizing the rod network's response to these noise sources would require using the transient impulse response function. Higher temporal frequency noise sources would contribute less and less to noise in more distant photoreceptors. On the other hand, in studies of photoreceptor noise in the turtle cones, it appears that the photocurrent noise is the largest determinant of the receptor voltage noise [70]. If this also applies to salamander rods, this would imply that our analysis of rod-rod coupling's effect on photoreceptor noise is a valid approximation.

Other than a more detailed analysis of the photoreceptors themselves, there are two possible directions in which studies of noise in the retina can be extended: to upstream noise in the stimulus source, and to downstream noise elements such as the synapse, bipolar cells, and ganglion cells.

While photoreceptors generate their own intrinsic noise from fluctuations in the photocurrent and ion channel activity, it has been shown that the major determinant to rod noise in response to dim visual scenes is the variability in the light stimulus itself [105]. The quantal nature of light means that in dimly lit conditions, fluctuations in the number of photons arriving in a given time interval may make up a significant fraction of the mean arrival rate. Photon emission, and thus arrivals, are probabilistic events, described by a Poisson distribution, which means that a variable numbers of photons will be absorbed in a given time interval. This variability is seen by the photoreceptor when the response to a single photon makes up a significant fraction of the total response in a given time interval. While it could be argued that variability in the incident light stimulus is an intrinsic part of the signal rather than a noise phenomenon, it nevertheless represents an uncertainty that the animal must deal with in order to perceive its surroundings.

In other systems where this type of variability is present it is often called shot noise. In low light or high speed photography, it is called photon noise, and can be seen in the noisy appearance of dim areas of images. In semiconductor devices, the particle nature of electron charge carriers manifests itself as small fluctuations in current flowing across a charge barrier which is called shot noise. Rice's analysis on the effect of shot noise in linear devices such as



vacuum tubes shows that the output noise in the device is proportional to the integral of the square of the impulse response of the device. The mean system output is the integral of the impulse response times the event rate (equation 6.1). This is known as Campbell's theorem [89]:

$$\bar{y} = \nu \int_0^{\infty} h(t) dt \quad (6.1)$$

$$\sigma_y^2 = \nu \int_0^{\infty} h^2(t) dt \quad (6.2)$$

Where  $\nu$  is the mean and variance for a Poisson distributed process, and  $h(t)$  is the impulse response for the linear system.

The integral of the impulse response is the step response of the system, and the integral of the square of the impulse response gives the output variance due to a single impulsive input. Therefore, the mean output is the mean input rate times the system step response, and the output variance is the arrival rate of each impulse times the variance of a single impulse.

Independently, Vu et al. and Jones [105, 62] found that the output variance of the photocurrent first increased, and then decreased, with increasing light intensity (photon arrival rate). This increase and decrease is due to the decreasing amplitude of the impulse response for a single photon arrival in the presence of brighter background light. Thus the noise produced by the photocurrent would not be constant, and instead vary with the light intensity that is incident on each photoreceptor.

This phenomenon occurs over a change in four orders of magnitude in the input light

intensity. Because natural scenes rarely show more than 50% contrast [105], there is little more than a 0.3 log unit difference in light intensity from the darkest to brightest part of a scene. There are likely some exceptions to this finding, but it means that the photon noise driving the photocurrent in rod photoreceptors would be nearly uniform over the retina for a given mean light intensity of a visual scene. As a result, the simple analysis performed in section 5.6, is also applicable to extrinsic photon noise as well as intrinsic noise.

In the future, it would like to extend the analysis of noise in the rod network presented here to demonstrate how the signal-to-noise ratio varies as a function of not only spatial frequencies, but also light intensity. It may also be useful to consider the exceptional cases where large contrast differences in a single image cause differences in background noise over different parts of the retina.

Another logical next logical step would be to extend the analysis of filtering in the rod network to investigate how the noise in rods is transformed and added to by higher order neurons in the retina. Specifically, it would be interesting to investigate the tradeoff of spatial averaging in the rod network vs. spatial averaging in the rod bipolar cells. Ideally if the rod-bipolar cell synapse were linear, there would be no difference between the two. However, given that the synapse has been shown to be nonlinear, there would be a difference in the averaging done before and after the synapse. Tessier-Lavigne and Attwell analyze this paradox using an ideal coupled network [101]. Their explanation is that at the initial rise of the sigmoidal response curve characteristic of the rod-bipolar cell synapse, the gain for small signals is lower than that for incrementally larger signals. This means that signals rid-

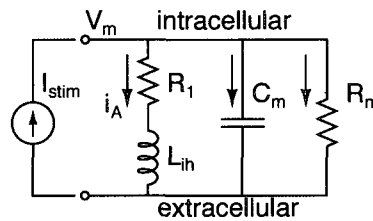
ing on top of depolarizing noise fluctuations would be amplified more compared to signals riding on hyperpolarizing noise fluctuations. This asymmetry would cause an increase in the overall noise, as random fluctuations above and below the mean would not average each other out. A more complete way to analyze this phenomenon would use the model of the rod network we have developed, and a more detailed model of the noise, which could include a harmonic analysis of intermodulation distortion to examine how synaptic nonlinearities would cause noise and signal to modulate one another.

By outlining these ideas for future work, I hope that I have outlined a path for myself and others to follow to continue what I have accomplished.

## Appendix A

### Appendix

#### A.1 Derivation of second order model parameters



The following describes how to calculate the analytical solution for the RLRC circuit model for HCN currents in the photoreceptor [57]

$$\begin{cases} v_m - L \frac{di_A}{dt} - R_1 i_A = 0 \\ i_s - i_A - v_m/R_m - C \frac{dv_m}{dt} = 0 \quad i_s = 0 \end{cases}$$

$$\begin{cases} v_m - L \frac{di_A}{dt} - R_1 i_A = 0 \\ i_A = v_m/R_m + C \frac{dv_m}{dt} \end{cases}$$

$$0 = v_m - L \left[ -\frac{dv_m}{dt} \frac{1}{R_m} - C \frac{d^2 v_m}{dt^2} \right] - R_1 \left( -\frac{v_m}{R_m} - C \frac{dv_m}{dt} \right)$$

$$0 = LC \frac{d^2 v_m}{dt^2} + \left( \frac{L}{R_m} + R_1 C \right) \frac{dv_m}{dt} + \left( 1 + \frac{R_1}{R_m} \right) v_m$$

Now putting the equation in the form  $\frac{d^2 x(t)}{dt^2} + 2\alpha \frac{dx(t)}{dt} + \omega_0^2 x(t) = 0$

$$\frac{d^2 v_m}{dt^2} + \left( \frac{1}{CR_m} + \frac{R_1}{L} \right) \frac{dv_m}{dt} + \left( \frac{1}{LC} + \frac{R_1}{LCR_m} \right) v_m = 0$$

Solve the characteristic equation  $s^2 + 2\alpha s + \omega_0^2$

$$\omega_0 = \sqrt{\frac{1}{LC} + \frac{R_1}{LCR_m}}$$

$$\alpha = \frac{1}{2CR_m} + \frac{R_1}{2L}$$

$$s = \frac{-2\alpha \pm \sqrt{4\alpha^2 - 4\omega_0^2}}{2}$$

$$s = -\frac{1}{2CR_m} - \frac{R_1}{2L} \pm \sqrt{\left(-\frac{1}{2CR_m} - \frac{R_1}{2L}\right)^2 - \left(\frac{1}{LC} + \frac{R_1}{LCR_m}\right)^2}$$

Now  $s_1$  and  $s_2$  are defined, along with  $\omega_0$  the resonant frequency (in radians/sec) and  $\alpha$  the damping factor

We look for a solution of the form  $v(t) = K_1 e^{s_1 t} + K_2 e^{s_2 t} + K_3$

We need to solve for  $K_1$ ,  $K_2$  and  $K_3$  from the final and initial conditions

$$\begin{cases} K_1 e^{-\infty} + K_2 e^{-\infty} + K_3 = i_s (R_1 || R_m) \\ \frac{d}{dt} [K_1 e^{s_1 t} + K_2 e^{s_2 t} + K_3] = \frac{dv_m}{dt} \Big|_{t=0} = i_s / C_m \\ K_1 e^0 + K_2 e^0 + K_3 = v(0) = 0 \end{cases}$$

$$\begin{cases} K_3 = i_s (R_1 || R_m) = i_s \frac{(R_1 R_m)}{R_1 + R_m} \\ s_1 K_1 + s_2 K_2 = \frac{dv_m}{dt} \Big|_{t=0} = i_s / C_m \\ K_1 + K_2 = -K_3 \end{cases}$$

Now the system is fully defined

## A.2 Frequency domain calculations

The following calculations were used to estimate the frequency response of a cell after fitting the step response. Calculations are performed in the Laplace domain.

$$\begin{aligned}
 Z(s) &= (R_1 + sL) \parallel R_m \parallel \frac{1}{sC} \\
 &= \left( \frac{sLR_m + R_1R_m}{R_m + R_1 + sL} \right) \parallel \frac{1}{sC} \\
 &= \left[ \frac{R_m + R_1 + sL}{sLR_m + R_1R_m} + \frac{sC(sLR_m + R_1R_m)}{sLR_m + R_1R_m} \right]^{-1} \\
 &= \left[ \frac{s^2LR_mC + sCR_1R_m + sL + R_1 + R_m}{sLR_m + R_1R_m} \right]^{-1}
 \end{aligned}$$

$$Z(s) = \frac{sLR_m + R_1R_m}{s^2LR_mC + s(CR_1R_m + L) + R_1 + R_m}$$

### A.3 Rod model parameters

Note: All numerical values are given as they were entered in the simulation. Units are provided for reference.

#### Cell Voltage and Currents

---

$$\begin{aligned} \dot{v} &= -1/C_m(i_{couple} + i_{kx} + i_h + i_{kv} + i_{leak} + i_{ca} + i_{photo}) \\ i_{couple} &= g_c \mathbf{A} v \\ i_{kx} &= g_{kx} m_{kx} (v - E_{kx}) \\ i_h &= g_h n_h (v - E_h) \\ i_{kv} &= g_{kv} n_{kv} (v - E_{kv}) \\ i_{leak} &= g_{leak} (v - E_{leak}) \\ i_{ca} &= g_{ca} n_{ca} (v - E_{ca}) \\ i_{photo} &= I_{dark} \vec{F} \end{aligned}$$

where (for n=3 rods in a linear network)...

$$\begin{aligned} \vec{v} &= \begin{pmatrix} v_1 & v_2 & v_3 \end{pmatrix}' \\ \vec{i} &= \begin{pmatrix} i_1 & i_2 & i_3 \end{pmatrix}' \\ \vec{F} &= \begin{pmatrix} F_1 & F_2 & F_3 \end{pmatrix}' \\ \mathbf{A} &= \begin{pmatrix} 1 & -1 & 0 \\ -1 & 2 & -1 \\ 0 & -1 & 1 \end{pmatrix} \end{aligned}$$

### Variables and Constants

$v$	Membrane voltage (mV)
$i$	Currents given in pA
$C_m = 35 \cdot 10^{-3}$ nF	
$g_c = 0.5$ nS	
$g_{kx} = 1.5$ nS	$E_{kx} = -74$ mV
$g_h = 2$ nS	$E_h = -30$ mV
$g_{kv} = 0.5$ nS	$E_{kv} = -74$ mV
$g_{leak} = 0.2$ nS	$E_{leak} = -55$ mV
$g_{ca} = 2$ nS	$E_{ca} = 40$ mV
$I_{dark} = -50$ pA	

### Photocurrent (from Hamer, 2000)

---

$F = (cG/cG_{dark})^{n_{cG}}$	Normalized dark current fraction
$\dot{R} = \phi - (1/\tau_R)R$	Rhodopsin activation rate
$\dot{E} = v_{rp}(R - (1/\tau_E)E)$	Phosphodiesterase activation rate
$c\dot{G} = A_{max}/(1 + (c/(K_{ca})^{n_{ca}}) - cG(\beta_{dark} + E\beta_E))$	cGMP activation rate

### Outer Segment Calcium Concentration and Buffer Activity

$\dot{c} = bJ_dF - \gamma_c(c - c_{min}) - \dot{c}_b$	Change in calcium concentration
$\dot{c}_b = k_1(e_t - c_b)c - k_2c_b$	Change in buffered calcium



*Variables and Constants*

$\phi$	Number of photoisomerizations
$R$	Number of activated rhodopsin molecules
$E$	Number of activated PDE molecules
$cG$	cGMP concentration in outer seg. ( $\mu\text{M}$ )
$c$	Calcium concentration in outer seg. ( $\mu\text{M}$ )
$c_b$	Buffered calcium concentration in outer seg. ( $\mu\text{M}$ )
$cG_{dark} = 2 \mu\text{M}$	Dark cGMP level
$n_{cG} = 2.201$	CNG channel activation Hill coeff.
$\tau_R = 0.416 \text{ s}$	Rhodopsin deactivation time const.
$v_{rp} = 1734.72 \text{ s}^{-1}$	Photopigment activation rate
$\tau_E = 1.195 \text{ s}$	PDE inactivation time const.
$A_{max} = 4.461 \mu\text{M/s}$	Maximum cGMP synthesis rate
$K_{ca} = 0.219 \mu\text{M}$	Half-activation level of guanylate cyclase by Ca
$n_{ca} = 2.855$	Ca activated guanylate cyclase Hill coeff.
$\beta_{dark} = 0.136 \text{ s}^{-1}$	cGMP hydrolysis rate in darkness
$\beta_E = 1.68 \times 10^{-5} \text{ s}^{-1}$	PDE dependent cGMP hydrolysis rate
$b = 0.780 \mu\text{Ms}^{-1}\text{pA}^{-1}$	Photocurrent to Ca flux
$J_d = 72.296 \text{ pA}$	Photocurrent model dark current
$\gamma_c = 99.67 \text{ s}^{-1}$	Ca exchanger extrusion rate
$c_{min} = 0.005 \mu\text{M}$	Minimum outer segment Ca level
$k_1 = 0.166 \mu\text{M}^{-1}\text{s}^{-1}$	Ca buffer binding rate
$e_t = 394.58 \mu\text{M}$	Total Ca buffer concentration
$k_2 = 2.350 \text{ s}^{-1}$	Ca buffer unbinding rate

---

h-current kinetics

---

$$n_h = 1 - ((1 - m_h)^4 + 4m_h(1 - m_h)^3) \quad \text{Probability of } \geq 2 \text{ of 4 particles being open}$$

$$\dot{m}_h = \alpha_h(1 - m_h) - \beta_h m_h \quad \text{Probability of one particle being open}$$

$$\alpha_h = 18/(1 + \exp((v + 88)/12))$$

$$\beta_h = 18/(1 + \exp(-(v + 18)/19))$$

---

kx-current kinetics

---

$$\dot{m}_{kx} = \alpha_{kx}(1 - m_{kx}) - \beta_{kx} m_{kx} \quad \text{Two-state noninactivating kinetics}$$

$$\alpha_{kx} = 0.66 \exp((v + 50)/(2 \cdot 5.7))$$

$$\beta_{kx} = 0.66 \exp(-(v + 50)/(2 \cdot 5.7))$$

---

kv-current kinetics

---

$$n_{kv} = m_{kv}^3 h_{kv} \quad \text{Gating with 3 activation and 1 inactivation particles}$$

$$\dot{m}_{kv} = \alpha_{mkv}(1 - m_{mkv}) - \beta_{mkv} m_{mkv} \quad \text{Activation particle}$$

$$\alpha_{mkv} = 5(100 - v) / \exp((100 - v)/42) - 1$$

$$\beta_{mkv} = 9 \exp(-(v - 20)/40)$$

$$\dot{h}_{kv} = \alpha_{hkv}(1 - h_{kv}) - \beta_{hkv} h_{kv} \quad \text{Inactivation particle}$$

$$\alpha_{hkv} = 0.15 \exp(-v/22)$$

$$\beta_{hkv} = 0.4125 / \exp(-(v - 10)/7 + 1)$$

---

Ca-current kinetics

---

$$n_{ca} = m_{ca}h_{ca}$$

Gating with 1 activation and 1 inactivation particle

$$\dot{m}_{ca} = \alpha_{mca}(1 - m_{ca}) - \beta_{mca}m_{ca}$$

Activation particle

$$\alpha_{mca} = 100 \exp((v + 10)/(2 \cdot 6))$$

$$\beta_{mca} = 100 \exp(-(v + 10)/(2 \cdot 6))$$

$$\dot{h}_{ca} = \alpha_{hca}(1 - h_{ca}) - \beta_{hca}h_{ca}$$

Inactivation particle

$$\alpha_{hca} = 0.5 \exp((v - 11)/(2 \cdot 9))$$

$$\beta_{hca} = 0.5 \exp(-(v - 11)/(2 \cdot 9))$$

---

Inner segment Ca buffer system

---

$$\dot{c}_{is} = R_{in} - R_{out}$$

$$R_{in} = \begin{cases} -i_{ca}/(F_c V f_v k_c z) & \text{if } i_{ca} < 0 \\ 0 & \text{otherwise} \end{cases}$$

$$R_{out} = (c_{is} - c_{min})/\tau_{Cai}$$

## Variables Constants

 $c_{is}$ Inner seg calcium conc. in  $\mu\text{M}$ 

$$F_c = 96500 \text{ C/mol}$$

Faraday constant

$$V = 2000 \mu\text{m}^3$$

Volume of the inner segment

$$f_v = 1 \times 10^{-15} \text{ L}/\mu\text{m}^3$$

Convert  $\mu\text{m}^3$  to L

$$k_c = 1 \times 10^6 \text{ pC}/\mu\text{C}$$

Conversion from pC to  $\mu\text{C}$ 

$$z = 2$$

Ca valence

$$c_{min} = 0.05 \mu\text{M}$$

Minimum inner seg. Ca concentration

$$\tau_{Cai} = 20 \times 10^{-3} \text{ s}$$

Calcium extrusion time const.

## A.4 Derivation of the solution for a one-dimensional infinite cable

Starting with the differential equation

$$\frac{v}{r_m} + C \frac{\partial v}{\partial t} - \frac{1}{r_a} \frac{\partial^2 v}{\partial x^2} = i$$

to find the impulse response (Green's function) use an impulsive input  $i$  in space and time

$$\frac{v}{r_m} + C \frac{\partial v}{\partial t} - \frac{1}{r_a} \frac{\partial^2 v}{\partial x^2} = \delta(t)\delta(x)$$

Take the Fourier transform with respect to space

$$\mathcal{F}_x \left\{ \frac{v}{r_m} + C \frac{\partial v}{\partial t} - \frac{1}{r_a} \frac{\partial^2 v}{\partial x^2} \right\} = \mathcal{F}_x \{ \delta(t)\delta(x) \}$$

$$\frac{v}{r_m} + C \frac{\partial v}{\partial t} - \frac{1}{r_a} - (j\omega)^2 v \frac{1}{r_a} = \delta(t) \frac{1}{\sqrt{2\pi}}$$

$$C \frac{\partial v}{\partial t} + \left( \frac{1}{r_m} + \frac{\omega^2}{r_a} \right) v = \delta(t) \frac{1}{\sqrt{2\pi}}$$

Solve first order ODE with respect to time by finding integrating factor  $\mu$ , multiplying both sides by  $\mu$  and integrating

$$\mu = \exp \left( \frac{1}{C} \left( \frac{1}{r_m} + \frac{\omega^2}{r_a} \right) t \right)$$

$$v = \frac{\int \exp \left( \frac{1}{C} \left( \frac{1}{r_m} + \frac{\omega^2}{r_a} \right) t \right) \frac{\delta(t)}{\sqrt{2\pi}} dt}{\exp \left( \frac{1}{C} \left( \frac{1}{r_m} + \frac{\omega^2}{r_a} \right) t \right)}$$

$$v = \frac{1}{C\sqrt{2\pi}} u(t) \exp \left( -\frac{1}{Cr_m} t \right) \exp \left( \frac{\omega^2}{Cr_a} t \right)$$

Take the inverse Fourier transform

$$\mathcal{F}^{-1} \left\{ \exp \left( \frac{\omega^2}{Cr_a} t \right) \right\} = \sqrt{\frac{r_a C}{2t}} \exp \left( \frac{Cr_a}{4t} x^2 \right)$$

according to Wolfram Mathematica, so...

$$v = \sqrt{\frac{r_a}{4\pi C t}} u(t) \exp \left( -\frac{1}{Cr_m} t \right) \exp \left( -\frac{Cr_a}{4t} x^2 \right)$$

### A.5 Derivation of the input impedance of a one-dimensional cable

Using the relationship for the steady-state voltage distribution for a one-dimensional cable:

$$v(x) = v_0 \exp\left(-\frac{|x|}{\lambda_{1D}}\right) \quad (\text{A.1})$$

The current into the point source (the originating cell) must be equal to the sum of all of the currents that flow through the membranes of all cells in the network, and the current through the membranes is the the cell voltage divided by the membrane resistance so:

$$i_0 = \int_{-\infty}^{\infty} v(x)/R_m dx \quad (\text{A.2})$$

Substituting A.1 into A.2 yields:

$$\begin{aligned} i_0 &= \int_{-\infty}^{\infty} \frac{v_0}{R_m} \exp\left(-\frac{|x|}{\lambda_{1D}}\right) dx \\ i_0 &= \frac{v_0}{R_m} \left( \int_{-\infty}^0 \exp\left(\frac{x}{\lambda_{1D}}\right) + \int_0^{\infty} \exp\left(-\frac{x}{\lambda_{1D}}\right) \right) \\ i_0 &= \frac{v_0}{R_m} \left( \lambda_{1D} \exp\left(\frac{x}{\lambda_{1D}}\right) \Big|_{-\infty}^0 - \lambda_{1D} \exp\left(-\frac{x}{\lambda_{1D}}\right) \Big|_0^{\infty} \right) \\ i_0 &= \frac{2v_0\lambda_{1D}}{R_m} \end{aligned}$$

Rearranging terms, keeping in mind that  $R_{in1D} = v_0/i_0$

$$R_{in1D} = \frac{R_m}{2\lambda} \quad (\text{A.3})$$

## Bibliography

- [1] A Akopian and P Witkovsky. D2 dopamine receptor-mediated inhibition of a hyperpolarization-activated current in rod photoreceptors. *J Neurophysiol*, 76(3):1828–35, Sep 1996.
- [2] C Altomare, A Bucchi, E Camatini, M Baruscotti, C Viscomi, A Moroni, and Dario DiFrancesco. Integrated allosteric model of voltage gating of HCN channels. *J Gen Physiol*, 117(6):519–32, Jun 2001.
- [3] Claudia Altomare, Benedetta Terragni, Chiara Brioschi, Raffaella Milanesi, Cinzia Pagliuca, Carlo Viscomi, Anna Moroni, Mirko Baruscotti, and Dario DiFrancesco. Heteromeric HCN1-HCN4 channels: a comparison with native pacemaker channels from the rabbit sinoatrial node. *J Physiol (Lond)*, 549(Pt 2):347–59, Jun 2003.
- [4] Osvaldo Alvarez, Carlos Gonzalez, and Ramon Latorre. Counting channels: a tutorial guide on ion channel fluctuation analysis. *Advances in physiology education*, 26(1-4):327–41, Dec 2002.
- [5] D Attwell and M Wilson. Behaviour of the rod network in the tiger salamander retina mediated by membrane properties of individual rods. *J Physiol (Lond)*, 309:287–315, Dec 1980.
- [6] D Attwell and M Wilson. The spatial frequency sensitivity of bipolar cells. *Biological Cybernetics*, 47(2):131–40, Jan 1983.
- [7] D Attwell, M Wilson, and Samuel M Wu. A quantitative analysis of interactions between photoreceptors in the salamander (ambystoma) retina. *J Physiol (Lond)*, 352:703–37, Jul 1984.
- [8] D Attwell, M Wilson, and Samuel M Wu. The effect of light on the spread of signals through the rod network of the salamander retina. *Brain Res*, 343(1):79–88, Sep 1985.

- [9] C R Bader and D Bertrand. Effect of changes in intra- and extracellular sodium on the inward (anomalous) rectification in salamander photoreceptors. *J Physiol (Lond)*, 347:611–31, Feb 1984.
- [10] C R Bader, D Bertrand, and E A Schwartz. Voltage-activated and calcium-activated currents studied in solitary rod inner segments from the salamander retina. *J Physiol (Lond)*, 331:253–84, Oct 1982.
- [11] Rosario M Balboa and Norberto M Grzywacz. Power spectra and distribution of contrasts of natural images from different habitats. *Vision Res*, 43(24):2527–37, Nov 2003.
- [12] S Barnes and Q Bui. Modulation of calcium-activated chloride current via Ph-induced changes of calcium channel properties in cone photoreceptors. *J Neurosci*, 11(12):4015–23, Dec 1991.
- [13] S Barnes and B Hille. Ionic channels of the inner segment of tiger salamander cone photoreceptors. *J Gen Physiol*, 94(4):719–43, Oct 1989.
- [14] Andrew J Barrow and Samuel M Wu. Low-conductance HCN1 ion channels augment the frequency response of rod and cone photoreceptors. *J Neurosci*, 29(18):5841–53, May 2009.
- [15] Mirko Baruscotti, Annalisa Bucchi, and Dario DiFrancesco. Physiology and pharmacology of the cardiac pacemaker (“funny”) current. *Pharmacol Ther*, 107(1):59–79, Jul 2005.
- [16] D A Baylor, M G Fuortes, and P M O’Byrne. Receptive fields of cones in the retina of the turtle. *J Physiol (Lond)*, 214(2):265–94, Apr 1971.
- [17] D A Baylor, G Matthews, and B J Nunn. Location and function of voltage-sensitive conductances in retinal rods of the salamander, *ambystoma tigrinum*. *J Physiol (Lond)*, 354:203–23, Sep 1984.
- [18] D A Baylor and B J Nunn. Electrical properties of the light-sensitive conductance of rods of the salamander *ambystoma tigrinum*. *J Physiol (Lond)*, 371:115–45, Feb 1986.
- [19] D J Beech and S Barnes. Characterization of a voltage-gated K<sup>+</sup> channel that accelerates the rod response to dim light. *Neuron*, 3(5):573–81, Nov 1989.

- [20] Jeff B Bowes, Kevin A Snyder, Erik Segerdell, Ross Gibb, Chris Jarabek, Etienne Noumen, Nicolas Pollet, and Peter D Vize. Xenbase: a xenopus biology and genomics resource. *Nucleic Acids Res*, 36(Database issue):D761–7, 2008.
- [21] Encyclopedia Britannica. William Thompson, Baron Kelvin.
- [22] H Brown, D DiFrancesco, and S Noble. Cardiac pacemaker oscillation and its modulation by autonomic transmitters. *J Exp Biol*, 81:175–204, Aug 1979.
- [23] H F Brown, Dario DiFrancesco, and S J Noble. How does adrenaline accelerate the heart? *Nature*, 280(5719):235–6, Jul 1979.
- [24] A Bucchi, A Tognati, R Milanese, M Baruscotti, and Dario DiFrancesco. Properties of ivabradine-induced block of HCN1 and HCN4 pacemaker channels. *J Physiol (Lond)*, 572(Pt 2):335–46, Apr 2006.
- [25] A L Byzov and T M Shura-Bura. Electrical feedback mechanism in the processing of signals in the outer plexiform layer of the retina. *Vision Res*, 26(1):33–44, Jan 1986.
- [26] Lorenzo Cangiano, Claudia Gargini, Luca Della Santina, Gian Carlo Demontis, and Luigi Cervetto. High-pass filtering of input signals by the  $I_h$  current in a non-spiking neuron, the retinal rod bipolar cell. *PLoS ONE*, 2(12):e1327, Jan 2007.
- [27] Gábor Czirják, Zsuzsanna E Tóth, and Péter Enyedi. Characterization of the heteromeric potassium channel formed by Kv2.1 and the retinal subunit Kv8.2 in xenopus oocytes. *J Neurophysiol*, 98(3):1213–22, Sep 2007.
- [28] Christopher M Davenport, Peter B Detwiler, and Dennis M Dacey. Effects of Ph buffering on horizontal and ganglion cell light responses in primate retina: evidence for the proton hypothesis of surround formation. *J Neurosci*, 28(2):456–64, Jan 2008.
- [29] Michael R Deans, Bela Volgyi, Daniel A Goodenough, Stewart A Bloomfield, and David L Paul. Connexin36 is essential for transmission of rod-mediated visual signals in the mammalian retina. *Neuron*, 36(4):703–12, Nov 2002.
- [30] Gian Carlo Demontis, B Longoni, U Barcaro, and L Cervetto. Properties and functional roles of hyperpolarization-gated currents in guinea-pig retinal rods. *J Physiol (Lond)*, 515 ( Pt 3):813–28, Mar 1999.



- [31] Gian Carlo Demontis, Anna Moroni, Biagio Gravante, Claudia Altomare, Bianca-maria Longoni, Luigi Cervetto, and Dario DiFrancesco. Functional characterisation and subcellular localisation of HCN1 channels in rabbit retinal rod photoreceptors. *J Physiol (Lond)*, 542(Pt 1):89–97, Jul 2002.
- [32] P B Detwiler and A L Hodgkin. Electrical coupling between cones in turtle retina. *J Physiol (Lond)*, 291:75–100, Jun 1979.
- [33] Peter B Detwiler, A L Hodgkin, and P A McNaughton. A surprising property of electrical spread in the network of rods in the turtle's retina. *Nature*, 274(5671):562–5, Aug 1978.
- [34] Peter B Detwiler, A L Hodgkin, and P A McNaughton. Temporal and spatial characteristics of the voltage response of rods in the retina of the snapping turtle. *J Physiol (Lond)*, 300:213–50, Mar 1980.
- [35] Steven H DeVries, Xiaofeng Qi, Robert Smith, Walter Makous, and Peter Sterling. Electrical coupling between mammalian cones. *Curr Biol*, 12(22):1900–7, Nov 2002.
- [36] D DiFrancesco and C Tromba. Inhibition of the hyperpolarization-activated current ( $I_f$ ) induced by acetylcholine in rabbit sino-atrial node myocytes. *J Physiol (Lond)*, 405:477–91, Nov 1988.
- [37] D DiFrancesco and C Tromba. Muscarinic control of the hyperpolarization-activated current ( $I_f$ ) in rabbit sino-atrial node myocytes. *J Physiol (Lond)*, 405:493–510, Nov 1988.
- [38] Dario DiFrancesco. Characterization of the pace-maker current kinetics in calf purkinje fibres. *J Physiol (Lond)*, 348:341–67, Mar 1984.
- [39] Dario DiFrancesco. Serious workings of the funny current. *Prog Biophys Mol Biol*, 90(1-3):13–25, Jan 2006.
- [40] Andrey V Dmitriev and Stuart C Mangel. Electrical feedback in the cone pedicle: a computational analysis. *J Neurophysiol*, 95(3):1419–27, Mar 2006.
- [41] Iris Fahrenfort, Marvin Steijaert, Trijntje Sjoerdsma, Evan Vickers, Harris Ripps, Jorrit van Asselt, Duco Endeman, Jan Klooster, Robert Numan, Huub ten Eikelder,

- Henrique von Gersdorff, and Maarten Kamermans. Hemichannel-mediated and Ph-based feedback from horizontal cells to cones in the vertebrate retina. *PLoS ONE*, 4(6):e6090, Jan 2009.
- [42] G L Fain, H M Gerschenfeld, and F N Quandt. Calcium spikes in toad rods. *J Physiol (Lond)*, 303:495–513, Jun 1980.
- [43] G L Fain and F N Quandt. The effects of tetraethylammonium and cobalt ions on responses to extrinsic current in toad rods. *J Physiol (Lond)*, 303:515–33, Jun 1980.
- [44] E E Fesenko, S S Kolesnikov, and A L Lyubarsky. Induction by cyclic gmp of cationic conductance in plasma membrane of retinal rod outer segment. *Nature*, 313(6000):310–3, Jan 1985.
- [45] K Fox, I Ford, P Steg, M Tendera, R Ferrari, and on behalf of the BEAUTIFUL investigators. Ivabradine for patients with stable coronary artery disease and left-ventricular systolic dysfunction (BEAUTIFUL): a randomised, double-blind, placebo-controlled trial. *Lancet*, 372(9641):807–816, Sep 2008.
- [46] K Fox, I Ford, P Steg, M Tendera, M Robertson, R Ferrari, and on behalf of the BEAUTIFUL investigators. Heart rate as a prognostic risk factor in patients with coronary artery disease and left-ventricular systolic dysfunction (BEAUTIFUL): a subgroup analysis of a randomised controlled trial. *Lancet*, 372(9641):817–821, Sep 2008.
- [47] S Frings, N Brüll, C Dzeja, A Angele, V Hagen, U B Kaupp, and A Baumann. Characterization of ether-à-go-go channels present in photoreceptors reveals similarity to  $I_{Kx}$ , a  $K^+$  current in rod inner segments. *J Gen Physiol*, 111(4):583–99, Apr 1998.
- [48] C Gargini, Gian Carlo Demontis, S Bisti, and L Cervetto. Effects of blocking the hyperpolarization-activated current ( $I_h$ ) on the cat electroretinogram. *Vision Res*, 39(10):1767–74, May 1999.
- [49] C Gargini, Gian Carlo Demontis, S Bisti, and L Cervetto. Temporal fidelity in the visual system. *Archives italiennes de biologie*, 137(4):299–309, Aug 1999.
- [50] C Gargini, Gian Carlo Demontis, L Cervetto, and S Bisti. Analysis of pharmacologically isolated components of the ERG. *Vision Res*, 39(10):1759–66, May 1999.

- [51] R D Hamer. Computational analysis of vertebrate phototransduction: combined quantitative and qualitative modeling of dark- and light-adapted responses in amphibian rods. *Vis Neurosci*, 17(5):679–99, Jan 2000.
- [52] O P Hamill, A Marty, E Neher, Bert Sakmann, and F J Sigworth. Improved patch-clamp techniques for high-resolution current recording from cells and cell-free membrane patches. *Pflugers Arch*, 391(2):85–100, 1981.
- [53] Espen Hartveit and Margaret Lin Veruki. Studying properties of neurotransmitter receptors by non-stationary noise analysis of spontaneous postsynaptic currents and agonist-evoked responses in outside-out patches. *Nature protocols*, 2(2):434–48, Jan 2007.
- [54] S Hestrin. The properties and function of inward rectification in rod photoreceptors of the tiger salamander. *J Physiol (Lond)*, 390:319–33, Sep 1987.
- [55] Hajime Hirasawa and Akimichi Kaneko. Ph changes in the invaginating synaptic cleft mediate feedback from horizontal cells to cone photoreceptors by modulating  $Ca^{2+}$  channels. *J Gen Physiol*, 122(6):657–71, Dec 2003.
- [56] Eric P Hornstein, Jan Verweij, and Julie L Schnapf. Electrical coupling between red and green cones in primate retina. *Nat Neurosci*, 7(7):745–50, Jul 2004.
- [57] J. David Irwin. *Basic engineering circuit analysis*. Macmillan Pub. Co., New York, 2nd ed edition, 1987.
- [58] Elena Ivanova and Frank Müller. Retinal bipolar cell types differ in their inventory of ion channels. *Vis Neurosci*, 23(2):143–54, Jan 2006.
- [59] Heather A Jackson, Christian R Marshall, and Eric A Accili. Evolution and structural diversification of hyperpolarization-activated cyclic nucleotide-gated channel genes. *Physiol Genomics*, 29(3):231–45, May 2007.
- [60] Jaakko L P Jarvinen and T D Lamb. Inverted photocurrent responses from amphibian rod photoreceptors: role of membrane voltage in response recovery. *J Physiol (Lond)*, 566(Pt 2):455–66, Jul 2005.
- [61] Daniel Johnston and Samuel Miao-sin Wu. *Foundations of cellular neurophysiology*. MIT Press, Cambridge, Mass., 1995.

- [62] G J Jones. Membrane current noise in dark-adapted and light-adapted isolated retinal rods of the larval tiger salamander. *J Physiol (Lond)*, 511 ( Pt 3):903–13, Sep 1998.
- [63] Maarten Kamermans and Iris Fahrenfort. Ephaptic interactions within a chemical synapse: hemichannel-mediated ephaptic inhibition in the retina. *Curr Opin Neurobiol*, 14(5):531–41, Oct 2004.
- [64] Y Kamiyama, T Ogura, and Shiro Usui. Ionic current model of the vertebrate rod photoreceptor. *Vision Res*, 36(24):4059–68, Dec 1996.
- [65] Fusao Kawai, Masayuki Horiguchi, Hiroshi Ichinose, Mahito Ohkuma, Ryoko Isobe, and Ei ichi Miyachi. Suppression by an  $I_h$  current of spontaneous  $\text{Na}^+$  action potentials in human cone and rod photoreceptors. *Invest Ophthalmol Vis Sci*, 46(1):390–7, Jan 2005.
- [66] Maarten H P Kole, Stefan Hallermann, and Greg J Stuart. Single  $I_h$  channels in pyramidal neuron dendrites: properties, distribution, and impact on action potential output. *J Neurosci*, 26(6):1677–87, Feb 2006.
- [67] D E Kurenniy and S Barnes. Regulation of M-like  $\text{K}^+$  current,  $I_{Kx}$ , by  $\text{Ca}^{2+}$ -dependent phosphorylation in rod photoreceptors. *Am J Physiol*, 272(6 Pt 1):C1844–53, Jun 1997.
- [68] Mélanie R Lalonde, Melanie E Kelly, and Steven Barnes. Calcium-activated chloride channels in the retina. *Channels (Austin, Tex)*, 2(4):252–60, Jan 2008.
- [69] T D Lamb and E J Simon. The relation between intercellular coupling and electrical noise in turtle photoreceptors. *J Physiol (Lond)*, 263(2):257–86, Dec 1976.
- [70] T D Lamb and E J Simon. Analysis of electrical noise in turtle cones. *J Physiol (Lond)*, 272(2):435–68, Nov 1977.
- [71] A Lasansky. Organization of the outer synaptic layer in the retina of the larval tiger salamander. *Philos Trans R Soc Lond, B, Biol Sci*, 265(872):471–89, Jan 1973.
- [72] John Lienhard. *Engines of Our Ingenuity*. University of Houston / NPR, episode 1924.
- [73] Xiao-Dong Liu and Dmitri E Kourennyi. Effects of tetraethylammonium on  $\text{K}_x$  channels and simulated light response in rod photoreceptors. *Annals of biomedical engineering*, 32(10):1428–42, Oct 2004.

- [74] J C Magee. Dendritic hyperpolarization-activated currents modify the integrative properties of hippocampal CA1 pyramidal neurons. *J Neurosci*, 18(19):7613–24, Oct 1998.
- [75] Andrew Todd Malcolm, Dmitri E Kourennyi, and Steven Barnes. Protons and calcium alter gating of the hyperpolarization-activated cation current ( $I_h$ ) in rod photoreceptors. *Biochim Biophys Acta*, 1609(2):183–92, Jan 2003.
- [76] Roope Männikkö, Fredrik Elinder, and H Peter Larsson. Voltage-sensing mechanism is conserved among ion channels gated by opposite voltages. *Nature*, 419(6909):837–41, Oct 2002.
- [77] Roope Männikkö, Shilpi Pandey, H Peter Larsson, and Fredrik Elinder. Hysteresis in the voltage dependence of hcn channels: conversion between two modes affects pacemaker properties. *J Gen Physiol*, 125(3):305–26, Mar 2005.
- [78] A V Maricq and J I Korenbrot. Inward rectification in the inner segment of single retinal cone photoreceptors. *J Neurophysiol*, 64(6):1917–28, Dec 1990.
- [79] P Z Marmarelis and K I Naka. Nonlinear analysis and synthesis of receptive-field responses in the catfish retina. 3. two-input white-noise analysis. *J Neurophysiol*, 36(4):634–48, Jul 1973.
- [80] Panos Z Marmarelis and Vasilis Z. Marmarelis. *Analysis of physiological systems: the white-noise approach*. Computers in biology and medicine. Plenum Press, New York, 1978.
- [81] The Mathworks. *MATLAB help documentation*, version 2008b edition.
- [82] S Moosmang, J Stieber, X Zong, M Biel, F Hofmann, and A Ludwig. Cellular expression and functional characterization of four hyperpolarization-activated pacemaker channels in cardiac and neuronal tissues. *Eur J Biochem*, 268(6):1646–52, Mar 2001.
- [83] Frank Müller, Alexander Scholten, Elena Ivanova, Silke Haverkamp, Elisabeth Kremmer, and U Benjamin Kaupp. HCN channels are expressed differentially in retinal bipolar cells and concentrated at synaptic terminals. *Eur J Neurosci*, 17(10):2084–96, May 2003.

- [84] Rishikesh Narayanan and Daniel Johnston. Long-term potentiation in rat hippocampal neurons is accompanied by spatially widespread changes in intrinsic oscillatory dynamics and excitability. *Neuron*, 56(6):1061–75, Dec 2007.
- [85] S Nikonov, N Engheta, and E N Pugh. Kinetics of recovery of the dark-adapted salamander rod photoresponse. *J Gen Physiol*, 111(1):7–37, Jan 1998.
- [86] Toshihiko Ogura, Tomo Oki Satoh, Shiro Usui, and Masahiro Yamada. A simulation analysis on mechanisms of damped oscillation in retinal rod photoreceptor cells. *Vision Res*, 43(19):2019–28, Sep 2003.
- [87] W G Owen and V Torre. High-pass filtering of small signals by retinal rods. Ionic studies. *Biophys J*, 41(3):325–39, Mar 1983.
- [88] R Publio, R Oliveira, and A Roque. A realistic model of rod photoreceptor for use in a retina network model. *Neurocomputing*, Jan 2006.
- [89] S.O. Rice. Mathematical analysis of random noise. In N. Wax, editor, *Noise and Stochastic Processes*, pages pp. 133–294. Dover, New York, 1954.
- [90] F Rieke and D A Baylor. Origin and functional impact of dark noise in retinal cones. *Neuron*, 26(1):181–6, Apr 2000.
- [91] Bert Sakmann and Erwin Neher. *Single-channel recording*. Plenum Press, New York, 2nd ed edition, 1995.
- [92] B Santoro, S G Grant, D Bartsch, and E R Kandel. Interactive cloning with the SH3 domain of n-src identifies a new brain specific ion channel protein, with homology to EAG and cyclic nucleotide-gated channels. *Proc Natl Acad Sci USA*, 94(26):14815–20, Dec 1997.
- [93] B Santoro, D T Liu, H Yao, D Bartsch, E R Kandel, S A Siegelbaum, and G R Tibbs. Identification of a gene encoding a hyperpolarization-activated pacemaker channel of brain. *Cell*, 93(5):717–29, May 1998.
- [94] T O Satoh and Masahiro Yamada. A bradycardiac agent ZD7288 blocks the hyperpolarization-activated current ( $I_h$ ) in retinal rod photoreceptors. *Neuropharmacology*, 39(7):1284–91, Apr 2000.
- [95] F J Sigworth. The variance of sodium current fluctuations at the node of Ranvier. *J Physiol (Lond)*, 307:97–129, Oct 1980.

- [96] C-W Siu, D K Lieu, and R A Li. Hcn-encoded pacemaker channels: from physiology and biophysics to bioengineering. *J Membr Biol*, 214(3):115–22, Jan 2006.
- [97] Frederick S Soo, Peter B Detwiler, and Fred Rieke. Light adaptation in salamander l-cone photoreceptors. *J Neurosci*, 28(6):1331–42, Feb 2008.
- [98] Juliane Stieber, Georg Stöckl, Stefan Herrmann, Benjamin Hassfurth, and Franz Hofmann. Functional expression of the human HCN3 channel. *J Biol Chem*, 280(41):34635–43, Oct 2005.
- [99] Juliane Stieber, Karen Wieland, Georg Stöckl, Andreas Ludwig, and Franz Hofmann. Bradycardic and proarrhythmic properties of sinus node inhibitors. *Mol Pharmacol*, 69(4):1328–37, Apr 2006.
- [100] T Tatsukawa, H Hirasawa, A Kaneko, and M Kaneda. Gaba-mediated component in the feedback response of turtle retinal cones. *Vis Neurosci*, 22(3):317–24, Jan 2005.
- [101] M Tessier-Lavigne and D Attwell. The effect of photoreceptor coupling and synapse nonlinearity on signal: noise ratio in early .... *Proceedings of the Royal Society of London. Series B*, Jan 1988.
- [102] Wallace B Thoreson and Eric J Bryson. Chloride equilibrium potential in salamander cones. *BMC neuroscience*, 5(1):53, Dec 2004.
- [103] V Torre and W G Owen. High-pass filtering of small signals by the rod network in the retina of the toad, *bufo marinus*. *Biophys J*, 41(3):305–24, Mar 1983.
- [104] John P Vessey, Anna K Stratis, Bryan A Daniels, Noel Da Silva, Michael G Jonz, Melanie R Lalonde, William H Baldrige, and Steven Barnes. Proton-mediated feedback inhibition of presynaptic calcium channels at the cone photoreceptor synapse. *J Neurosci*, 25(16):4108–17, Apr 2005.
- [105] T Q Vu, S T McCarthy, and W G Owen. Linear transduction of natural stimuli by dark-adapted and light-adapted rods of the salamander, *ambystoma tigrinum*. *J Physiol (Lond)*, 505 ( Pt 1):193–204, Nov 1997.
- [106] Min Wang, Brian P Ramos, Constantinos D Paspalas, Yousheng Shu, Arthur Simen, Alvaro Duque, Susheel Vijayraghavan, Avis Brennan, Anne Dudley, Eric Nou, James A Mazer, David A McCormick, and Amy F T Arnsten. Alpha2a-adrenoceptors

strengthen working memory networks by inhibiting cAMP-HCN channel signaling in prefrontal cortex. *Cell*, 129(2):397–410, Apr 2007.

- [107] L P Wollmuth. Mechanism of Ba<sup>2+</sup> block of M-like K channels of rod photoreceptors of tiger salamanders. *J Gen Physiol*, 103(1):45–66, Jan 1994.
- [108] L P Wollmuth and B Hille. Ionic selectivity of  $I_h$  channels of rod photoreceptors in tiger salamanders. *J Gen Physiol*, 100(5):749–65, Nov 1992.
- [109] S M Wu, F Gao, and B R Maple. Integration and segregation of visual signals by bipolar cells in the tiger salamander retina. *Prog Brain Res*, 131:125–43, Jan 2001.
- [110] Samuel M Wu. Synaptic transmission from rods to bipolar cells in the tiger salamander retina. *Proc Natl Acad Sci USA*, 82(11):3944–7, Jun 1985.
- [111] Samuel M Wu and X L Yang. Modulation of synaptic gain by light. *Proc Natl Acad Sci USA*, 89(24):11755–8, Dec 1992.
- [112] K W Yau. Phototransduction mechanism in retinal rods and cones. the friedenwald lecture. *Invest Ophthalmol Vis Sci*, 35(1):9–32, Jan 1994.
- [113] Ai-Jun Zhang and Samuel M Wu. Receptive fields of retinal bipolar cells are mediated by heterogeneous synaptic circuitry. *J Neurosci*, 29(3):789–97, Jan 2009.
- [114] J Zhang and S Wu. Immunocytochemical analysis of photoreceptors in the tiger salamander retina. *Vision Res*, Oct 2008.
- [115] Jian Zhang and Samuel M Wu. Physiological properties of rod photoreceptor electrical coupling in the tiger salamander retina. *J Physiol (Lond)*, 564(Pt 3):849–62, May 2005.